UNIVERSITEIT GENT

Ghent University
Faculty of Sciences

Sol-gel processes for protection and synthesis of luminescent materials

Thesis submitted in fulfilment of the requirements for the award of the degree of doctor of philosophy in sciences: physics by

Nursen Avci

Promoters:

Prof. Dr. Dirk Poelman (Department of Solid State Sciences)
Prof. Dr. Philippe Smet (Department of Solid State Sciences)

Academic year 2011-2012

Members of the Exam committee

Chairman

Prof. Dr. Freddy Callens (Ghent University, Department of Solid State Sciences)

Reading committee

Prof. Dr. Philippe Smet (Ghent University, Department of Solid State Sciences)
Prof. Dr. Klaartje De Buysser (Ghent University, Department of Inorganic and Physical Chemistry)
Prof. Dr. Benoît Heinrichs (Université de Liège, Laboratoire de Génie chimique-Génie catalytique)

The other members of the examination committee

Prof. Dr. Dirk Poelman (Ghent University, Department of Solid State Sciences)
Prof. Dr. Christophe Detavernier (Ghent University, Department of Solid State Sciences)
Dr. Davy Wauters (European Patent Attorney and owner at DenK iP bvba)

This research has been conducted at the LumiLab research group at the Department of Solid State Sciences (Ghent University)

Special thanks

The research presented in this PhD thesis has been performed at the department of Solid State Sciences of Ghent University. I would like to acknowledge that this would not have been possible without the top-level expertise, outstanding guidance and the encouragement of my promoter, colleagues, friends and family. Therefore, I would like to express my sincere gratitude to all the people who helped me through the process of finalizing my thesis.

First and foremost, I would like to express my great gratitude to Dirk Poelman who has been a excellent promoter during this study. I am also indebted to Philippe Smet who I aspire to be like one day. Their perpetual energy and enthusiasm in research has been a great source of motivation for all their advisees, including me. In addition, they were always accessible and prepared to help their students with their research. As a result, my research life proved to be smooth and rewarding for me. I am deeply obliged to these two great scientists. I simply cannot thank them enough.

When I began my doctoral study, I shared the office with Philippe and Jo. Jo, thank you for all your explanations, endless patience and for giving me those beautiful particles that I could use for a long time.

I would like to single out the LumiLab guys as well. Dearest Katleen, we spent more than 2 years in the same office. It was very nice to have someone with whom I could talk about everything. Koen, thank you for your never-ending kindness, and for your help with latex. Thank you Anthony for letting me use the oven first even when you had registered it for yourself. Thanks to you, I am now living in a house with a big garden. Jonas; your positive energy made my days in the office more pleasant. Although we never managed to arrange a day on which only Dutch was spoken, I could pass my exams thanks to your guidance. And Iolanda, thank you for all your clarifications of chemical reactions and friendship. Hard working and lovely Lisanne, it was very nice to work with you. I would like also to thank Hilde

Poelman for the XPS analysis of TiO_2 and the engaging conversations.

Many thanks to the staff at the Department of Solid State Sciences whose friendship and support have made it much more than a temporary place of study for the students. I would especially like to thank Elly De Vos for her help with the administrative things, Henk Vrielinck and Johan Lauwaert for the FT-IR measurements, Nico De Roo and Olivier Janssens for their technical assistance in computer, XPS, XRD and SEM measurements and analyses.

I would like to acknowledge Klaartje De Buysser, Nigel Vandevelde and Jonas Feys from the SCRiPTS group who assisted me during my visits to S3 for viscosity, pH and TGA/DTA measurements and on understanding the sol-gel mechanism. I am indebted to Björn Vandecasteele from the CMST group for the degradation measurements.

I would also like to express my deepest gratitude to the interuniversity attraction poles programme IAP/VI- 17 (INANOMAT) financed by the Belgian State, Federal science policy office for financial assistance.

Zelal ve Doğan, soğuk bir ülkenin sunduğu inanılmaz derecede sıcak iki insan, dostluğunuz hiçbir şey ile ölçülemez. Sevgili Setenay dostluğun ve yardımların için teşekkürler. Trabzondaki ailem, anneciğim ve babacığım, eğer siz yardımıma koşmasaydınız, bu tezi zamanında teslim edemezdim, tüm desteğiniz ve yardımlarınız için kalpten teşekkürler. Bu tezin referanslar kısmındaki birçok makeleyi bana gönderen insan, abim, sabrın, ilgin ve yardımların için teşekkürler. Yengeciğim ve amcacığım, kendimden şüphe duyduğum zamanlarda bile sizin bana olan desteğiniz hiç bitmedi, umarım sizi hep mutlu etmişimdir, teşekkürler bana kattığınız herşey için. Anneciğim, babacığım, ve minik fasulyem; bana hep inandığınız ve aramızdaki onca kilometreye rağmen yanımda olduğunuzu hep hissettirdiğiniz için teşekkürler.

And finally, to my dear
Teşekkürler hep yanımda olduğun ve hayatıma aşk kattığın için.

Contents

Contents **iii**

1 Introduction **1**

2 Luminescent Materials **5**
2.1 How does luminescence work? 7
2.1.1 Configurational coordinate model 7
2.1.2 Electron-lattice interaction 10
2.1.3 Spectral shape 11
2.1.4 Energy transfer between luminescent ions 14
2.1.4.1 Energy transfer between two different luminescent ions 14
2.1.4.2 Energy transfer between two identical luminescent ions 14
2.1.5 Photoionization 15
2.1.6 The decay of luminescence 16
2.1.6.1 Fluorescence 16
2.1.6.2 Persistent luminescence 17
2.1.7 Host material 17
2.1.8 Europium as luminescent ion 19
2.1.8.1 Eu^{3+} 19
2.1.8.2 Eu^{2+} 20

3 Material Preparation **23**
3.1 Preparation of CaS:Eu 23
3.2 Non-Aqueous Sol-Gel 24
3.2.1 Effect of precursor 26
3.2.2 Effect of water/alkoxide ratio 28
3.2.3 Effect of alcohol 29
3.2.4 Effect of catalyst 30
3.2.5 Effect of reaction temperature 31

3.2.6 Aqueous versus non-aqueous . . . 31
3.3 TiO_2 thin films powders and protection layers . . . 32
3.4 Al_2O_3 thin films . . . 34
3.5 $CaAl_2O_4$:Eu,Nd . . . 36
3.6 Preparation Instruments . . . 37
3.6.1 Classic tube furnace annealing . . . 37
3.6.2 Electron beam annealing . . . 38
3.6.3 Spin coating . . . 38
3.7 Atomic layer deposition (ALD) . . . 39

4 Characterization Techniques and Instruments 41
4.1 X-ray diffraction . . . 41
4.1.1 in situ XRD . . . 41
4.1.2 ex situ XRD . . . 41
4.1.2.1 Orientation of the planes . . . 42
4.1.2.2 Bragg's law . . . 42
4.1.2.3 Intensity of the diffraction peaks . . . 43
4.1.2.4 Details of diffraction patterns . . . 44
4.2 Scanning electron microscopy . . . 44
4.2.1 Energy dispersive analysis of X-rays (EDX) . . . 46
4.3 X-ray photoelectron spectroscopy (XPS) . . . 47
4.4 Steady state fluorescence spectrometer . . . 48
4.4.1 In situ steady state fluorescence spectrometer . . . 50
4.4.1.1 Optical transmission measurements . . . 50
4.5 Spectroscopic ellipsometry . . . 51
4.6 Thermal analysis . . . 52
4.7 Fourier transform infrared spectroscopy . . . 53

5 Literature data 55
5.1 White-light emitting diodes (LEDs) . . . 55
5.2 $CaS:Eu^{2+}$ . . . 57
5.2.1 Luminescence of CaS . . . 57
5.2.2 Luminescence of $CaS:Eu^{2+}$ . . . 57
5.2.3 Degradation of CaS . . . 58
5.2.4 Luminescence of $CaSO_4$:Eu . . . 59
5.2.5 Stability improvement of $CaS:Eu^{2+}$ . . . 60
5.3 Optical and structural properties of TiO_2 . . . 62
5.4 Optical and structural properties of Al_2O_3 . . . 63
5.5 $CaAl_2O_4$ . . . 64
5.6 Luminescence of doped $CaAl_2O_4$ . . . 66

6 Luminescence and degradation of CaS:Eu^{2+} 69
6.1 Motivation . . . 69
6.2 Crystallographic and luminescent characterization of CaS :Eu^{2+} 70
6.3 Degradation study of CaS:Eu^{2+} . . . 72
6.3.1 Low temperature degradation . . . 73
6.3.2 High temperature degradation . . . 75
6.4 Conclusions and perspectives . . . 78

7 TiO_2 powders and thin films 81
7.1 Motivation . . . 81
7.2 Thermal analysis (TGA/DTA) . . . 82
7.3 Crystallization and phase transformations of powders . . . 83
7.4 Morphology, thickness and optical properties of thin films . . . 86
7.5 TiO_2 as a protection layer . . . 91
7.6 Conclusions and perspectives . . . 96

8 Al_2O_3 thin films 99
8.1 Motivation . . . 99
8.2 Optical and structural properties of Al_2O_3 thin films . . . 100
8.3 Al_2O_3 as a protection layer . . . 106
8.3.1 Al_2O_3 prepared with sol-gel . . . 106
8.3.2 Al_2O_3 prepared with ALD . . . 111
8.4 Conclusions and perspectives . . . 116

9 $CaAl_2O_4$:Eu^{2+},Nd^{3+} powders 119
9.1 Motivation . . . 119
9.2 $CaAl_2O_4$:Eu . . . 120
9.2.1 Optimum annealing temperature . . . 120
9.2.2 Influence of the Eu concentration . . . 124
9.2.3 Reduction of Eu^{3+} to Eu^{2+} . . . 125
9.3 $CaAl_2O_4$:Eu^{2+},Nd^{3+} . . . 129
9.4 Conclusions and perspectives . . . 130

10 Closing remarks 133

11 List of publications 137
11.1 Publications directly related to this research . . . 137
11.2 Other publications . . . 138
11.3 International conference contributions . . . 138
11.4 Other contributions . . . 140

12 Nederlandstalige samenvatting 141

Bibliography 145

Chapter 1

Introduction

Throughout history, the fascination of glass and porcelain has always encouraged people to improve their quality. In the 19^{th} century silica gel was used as a glazing solution as binder for ceramic powders to make porcelain. This gel was prepared using a technique which is remarkably similar to those of today's sol-gel chemistry. Meanwhile the first silicon alkoxide was synthesized using silicon tetrachloride and alcohol by Ebelmen [1]. Although sol-gel chemistry allows to synthesize a wide range of inorganic and organic composite materials, till the 1930s the technique had little scientific impact. The technique has been awarded deserved interest thanks to W. A. Patric who understood very well the reproducibility of silica gel and introduced the use of silica as desiccants, catalysts and absorbent materials [2]. Plenty of patents, a lot of materials and useful information about the mechanism of sol-gel processes have followed this progress.

Sol-gel chemistry has a very broad application area such as thin films and coatings, monoliths, powders, grains and spheres, fibers, composites, porous gels and membranes. From thin film to powder, different kinds of materials with excellent control of stoichiometry, density and microstructure can be synthesized using simple equipment without the need for vacuum and at relatively low temperatures. Using sol-gel, it is also possible to obtain the same material with different properties by changing only one parameter during the preparation. The broad application range and specific advantages of the technique make it very attractive.

Sol-gel techniques can be divided into two groups depending on the solvent: aqueous and non-aqueous sol-gel techniques. The aqueous sol-gel method is the more popular one but in some cases there are a few drawbacks in this method. When precursors with strong reactivity towards water (like titanium

alkoxides) are used, the hydrolysis reaction can result in precipitation [3]. In addition to this, for the preparation of rare-earth doped layers, water encourages hydrolysis of the rare-earth ion and accordingly the dispensability of the ion decreases [4, 5]. Also using water during the preparation of layers to protect sulfide particles can damage their luminescent feature [6, 7].

In the LumiLab research group, different kinds of luminescent materials such as oxides, nitrides and particularly sulfides are synthesized. Sulfides have a special place in luminescent materials because of their relatively low synthesis temperature and broad emission spectra upon doping with europium and cerium [7]. In addition to their use as wavelength converters in LEDs, alkaline earth sulfide phosphors are employed in different areas such as display applications [8], electroluminescent devices [9] and optical information storage [10]. Nevertheless, the lack of stability with respect to water and other atmospheric components hinders usage of the alkaline earth sulfides as phosphor hosts [6,8,11–15]. Degradation of the alkaline earth sulfides is accelerated by temperature and decomposition products such as sulfur dioxide and hydrogen sulfide gases evolve from the surface [11], finally forming sulfates and carbonates [7]. Therefore the decomposition causes not only a decrease in the light intensity, but also shifting of the emission wavelength. A number of encapsulation techniques have been utilized to improve the stability of sulfide phosphors on a large scale [6, 14–18]. Upon encapsulation with an inert film, the film should be thermally and chemically stable. In addition, it should be transparent to the excitation and emission light of the incorporated luminescent particles. The film should also homogeneously coat the particle surfaces. Furthermore, the preparation of the inert film and the coating are as important as the properties of the film. If there is an excess amount of water and/or strong acid in these processes, it may cause the degradation of moisture-sensitive material during the preparation. In this study, we started with CaS:Eu luminescent particles prepared by solvothermal synthesis and used two different techniques to encapsulate these particles: namely, overall coating with TiO_2 and Al_2O_3 via non-aqueous sol-gel technique and microencapsulation with Al_2O_3 via Atomic Layer Deposition (ALD). The optical and structural properties of the coating layers were thoroughly investigated.

Persistent luminescent materials are distinguished from ordinary luminescent materials by their long decay time. They are for instance used in emergency signs, toys and luminous paint. The LumiLab group is also working on the synthesis and the nature of persistent luminescent materials. The alkaline earth aluminates doped with Eu^{2+} and R^{3+} (R: rare earth) MAl_2O_4: Eu^{2+}, R^{3+} (M: Ca, Sr, Ba) are among the best known persistent luminescent ma-

terials [19]. In most of the preparation techniques very high temperature, vacuum or additional chemicals are required to synthesize MAl_2O_4: Eu^{2+}, R^{3+}. Sol-gel is used as a promising alternative to these techniques due to relatively low preparation temperature, control of the stoichiometry with simple equipment and high homogeneity. In the last year of this study, we synthesized Eu and Nd doped $CaAl_2O_4$ via the non-aqueous sol-gel technique.

Structure of the thesis

In the next three chapters, a general introduction on luminescence (Chapter 2) and details about experimental (Chapter 3) and characterization (Chapter 4) aspects of this work are given. The following chapter focuses on the literature review of the materials studied during this research. In Chapter 6, crystallographic and luminescent characterization and also the degradation of CaS :Eu^{2+} particles are dealt with. The optical and structural properties of TiO_2 thin films and powders and Al_2O_3 thin films and their performance as protection layer are evaluated in Chapters 7 and 8, respectively. Chapter 9 is devoted to the study of the persistent luminescent material $CaAl_2O_4$: Eu^{2+}, Nd^{3+}. The last chapter summarizes the original contributions of this work and states the main conclusions.

Chapter 2

Luminescent Materials

Luminescence is a term used to describe the conversion of a certain type of energy into light which is different than thermal radiation. Luminescence can be classified depending on how the light is generated:

- **Chemiluminescence and bioluminescence:** The emission of light by the release of energy from a chemical reaction is called *chemiluminescence*. The reaction of Luminol ($C_8H_7N_3O_2$) with an appropriate oxidant results in a striking blue glow. *Bioluminescence* is also known as "living light" and the most amazing examples of this phenomena can be found in the deep seas. In the darkness of the oceans where sun light can not reach, several living organisms produce light as the result of chemical reactions.

- **Triboluminescence:** In this accidentally discovered type of luminescence, light is generated by mechanical energy. Pulling apart, ripping, scratching, crushing, or rubbing can result in the breaking of chemical bonds in the material which triggers light emission like in sugar or silicon crystals.

- **Thermoluminescence:** The heating up of certain materials causes the release of previously absorbed energy by emission of light. This is called *thermoluminescence*.

- **Cathodoluminescence (CL):** The light emission is a result of electron beam excitation. Both in the case of cathode ray tube (CRT) televisions or computer screens and a scanning electron microscope (SEM), an electron gun is used for this purpose.

- **Electroluminescence (EL):**Light is generated in response to an applied electric field on a certain material. The most used electroluminescent devices in daily life are certainly light emitting diodes (LEDs).

- **Photoluminescence (PL):** Emission of the light is the result of the excitation by light with in general higher energy than the emitted light. Photoluminescence has a very broad application area from whitening substances in washing powder to plasma screens for large scale displays. Some photoluminescent powders which are synthesized in our laboratory are indicated in Fig. 2.1. The powders are excited at 320 nm and emit at different wavelengths. There is a special type of luminescence which has a very slow decay with the emission continuing for minutes or hours. This type of luminescence is called long lasting or persistent luminescence and it is commonly used in safety and exit marking.

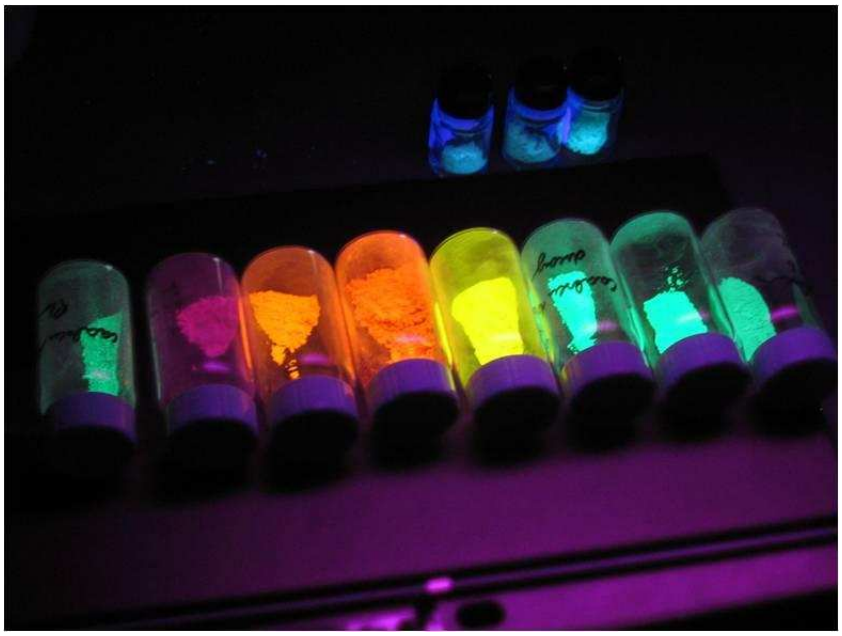

Figure 2.1: Examples of photoluminescent powders under UV excitation.

An inorganic luminescent material is also called a *phosphor*. The phosphor name originates from the Greek words *phos* expressing light and *phoros* expressing bearer. The meaning of phosphor has remained the same over the centuries. The reported first phosphor was prepared by Japanese from seashells in the 10^{th} century. However, the "phosphor" word has only been used after Vincentinus Casciarolo of Bologna, Italy in the early 17^{th} century.

Casciarolo found a stone which is probably barite ($BaSO_4$) and fired it with the intention to convert it into a noble metal. Although he did not obtain any metal, he discovered a material which glows (red light) in the dark after exposure to sunlight. In 1866 Théodore Sidot prepared zinc sulfide (ZnS) which was the prototype of phosphor used in the present day cathode ray tubes. In Germany, between late 19^{th} and early 20^{th} centuries Philip E.A. Lenard and colleagues worked on phosphors. They used different rare earth ions in addition to heavy metal ions as luminescent ions in different host materials [20].

2.1 How does luminescence work?

Most of the luminescent materials consist of a transparent host crystal and a luminescent ion called an *activator*. The activator consists of a very small amount of impurity atoms which are deliberately added into the host crystal. Most of the time emission and excitation features of the luminescent material are determined by the activator. Luminescent properties of activators such as Eu^{3+} and Eu^{2+} are explained by the configurational coordinate model.

2.1.1 Configurational coordinate model

Although the activator is responsible for the luminescence properties of the phosphor, the surrounding atoms' vibrations also have an effect on optical properties. The configurational coordinate model [20] is used to explain this fact by selecting a luminescent ion and its nearest neighbour sites like an isolated molecule which is called the *luminescent center*. In this way, displacement of the other atoms and their particular coordinates are generalized by one coordinate. Thus, all other atoms' positions are shown at once and this generalized coordinate is called "configurational coordinate" Q. In this model, potential energy curves are used to explain optical properties of the localized center (Fig. 2.2). The total energy (electron energy + ion energy) of the molecule in the ground state (g) and excited state (e) is indicated by the curves as a function of the configurational coordinate. For simplicity, the vibrational frequencies of the ground and the excited states are often assumed the same.

Usually only the totally symmetric vibrational mode or the "breathing mode" is taken into account, nevertheless this model introduces very useful information such as:

- Stokes' shift; the energy difference between absorption and emission.

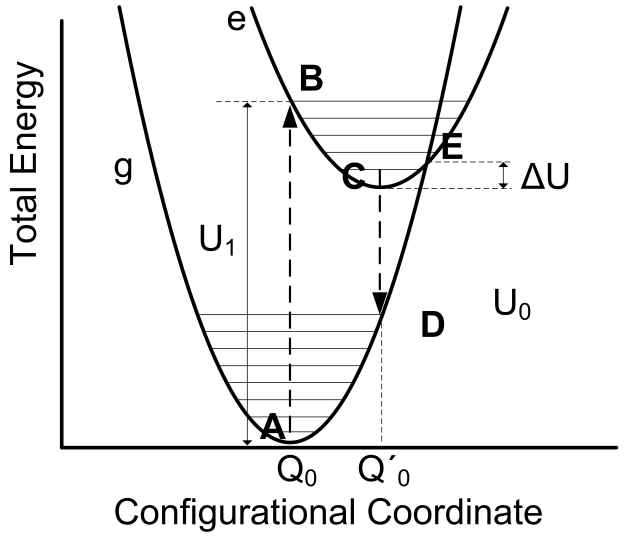

Figure 2.2: A schematic illustration of a configurational coordinate model [20]. Transitions between ground (g) and excited (e) state are shown with broken arrows A $\rightarrow$ B (the absorption of light) and C $\rightarrow$ D (the emission of light). The parabola offset is ΔQ= | Q_0-Q'_0 | .

- The temperature dependence and the widths of absorption and emission bands.

- Thermal quenching of luminescence. This model gives only a qualitative explanation of thermal quenching. It is necessary to use a multidimensional model for quantitative explanation [20].

The parabolic shape of curves is inherited from the vibration motion of the bonds between the luminescent ion and a nearest-neighbor ion which is assumed to be harmonic and it is expressed by Hooke's law [21];

$$F_g = -K_g\,(Q - Q_0) \tag{2.1}$$

$$F_e = -K_e\,(Q - Q'_0) \tag{2.2}$$

Where F_g and F_e are the restoring forces in ground state and excited state, respectively. K_g and K_e are the force constants of the chemical bonds, Q_0 is the equilibrium position of the ground state and Q'_0 is the interatomic equilibrium position of the excited state. This force corresponds to an energy with parabolic dependency on Q. The total energy of the ground state U_g and of the excited state U_e are given by the following equations [20].

$$U_g = K_g \frac{(Q - Q_0)^2}{2} \tag{2.3}$$

$$U_e = K_e \frac{(Q - Q_0')^2}{2} + U_0 \tag{2.4}$$

Here U_0 is the total energy of the excited state at Q=Q_0'.

The chemical bonds between the luminescent ion and the lattice (electron-phonon coupling) in the excited state are different from those in the ground state (usually weaker). Accordingly, a difference on the force constants (mostly $K_g > K_e$) and the equilibrium distances is observed. The shift of the parabolas are also seen in Fig. 2.2. The larger value of Q_0' induces a larger Stokes' shift and broader absorption and emission bands.

The optical absorption and emission processes are indicated in Fig. 2.2. It is assumed that these processes occur at 0 K and the nucleus of the luminescent ion does not change its position during the absorption (the Franck Condon principle). The absorption from the lowest vibrational level of the ground state is shown by the arrow A $\rightarrow$ B. The wave functions of the levels are known and in the lowest vibrational level, the highest probability of finding the system is near the equilibrium position. Nevertheless, for higher vibrational levels the highest probability position is at the edges of the parabolas [21,22]. The transition from state B to the equilibrium position C is relaxation since in the same state the probability of losing energy by light emission is about 10^5 times lower than by the generation of lattice vibrations. Spontaneously, emission occurs (C $\rightarrow$ D) and the cycle is completed by the second relaxation from a high vibrational level in the ground state D to the equilibrium position A. In other words, after absorption (A $\rightarrow$ B), the luminescent center expands to a new equilibrium position Q_0' at higher energy (B $\rightarrow$ C). Then a large part of the energy is lost by emission (C $\rightarrow$ D). By the relaxation process (D $\rightarrow$ A) to the equilibrium position of the ground state, the luminescent center contracts again.

As shown in Fig. 2.2 when two parabolas intersect, an electron in the excited state can nonradiatively turn back to the ground state through the intersection E over a thermal barrier. The non-radiative transition probability,W_{NR}, exponentially depends on the activation energy ΔU which is required to excite the electron from the equilibrium position of the excited state to the

intersection E of the parabolas.

$$W_{NR} = s.exp\left(\frac{-\Delta U}{kT}\right) \tag{2.5}$$

Where k is the Boltzmann constant and s is the frequency factor. ΔU is a thermal energy. At higher temperatures the non-radiative transition probability is higher due to the exponential dependence on T. The case, which is explained above, is not the only possible way for the non-radiative transition. The non-radiative decay process may be observed when the equilibrium position of the excited state is placed outside the configurational coordinate curve of the ground state. In this case, the excited state intersects the ground state in relaxing from B to C. Although W_{NR} is usually governed by thermal relaxation processes, it can be increased by the resonant energy transfer between two luminescent ions. In this case, luminescent ions are very close each other, accordingly their electronic wave functions overlap each other. This will be dealt with again in section 2.1.4.

2.1.2 Electron-lattice interaction

The electron-lattice interaction (electron-phonon coupling) in the excited state is different than in the ground state and this difference affects the spectral shape.

If the excited and ground state have equal force constants (K_g=K_e=K) or in other words if the parabolas have the same shape, the energy loss in the relaxation process is equal to S$\hbar\nu$ per parabola, where $\hbar\nu$ is the energy difference between two vibrational levels. S is the number of emitted phonon accompanying the optical transition and it is a integer which is called the Huang-Rhys coupling constant and given as follows [22]:

$$\begin{aligned} S\hbar\nu &= U_e\left(Q_0\right) - U_e\left(Q_0'\right) \\ &= K\frac{\left(Q_0 - Q_0'\right)^2}{2} + U_0 - U_0 \\ S\hbar\nu &= K\frac{\left(Q_0 - Q_0'\right)^2}{2} \end{aligned} \tag{2.6}$$

The Stokes shift is defined by [21]

$$\begin{aligned}\Delta S &= U_e\left(Q_0\right) - \left[U_e\left(Q_0'\right) - U_g\left(Q_0'\right)\right] \\ &= K\left(Q_0 - Q_0'\right)^2 \\ \Delta S &= 2S\hbar\nu \end{aligned} \tag{2.7}$$

This equation shows the dependency of the Stokes shift on the S value. A larger S value leads to a larger Stokes shift. Equation 2.6 indicates the relation between S and the offset (ΔQ= | Q_0-Q_0' |) of the parabola in the configurational coordinate model (Fig. 2.2), S is proportional to $(\Delta Q)^2$ and measures the strength of the electron-phonon coupling [21]. One distinguishes weak coupling for S<1, intermediate coupling for 1<S<5 and strong coupling for S>5.

2.1.3 Spectral shape

The effect of S can also be seen on the spectral shape of the absorption and emission. At T=0 K, only the lowest vibrational level (n=0) of the ground state is occupied. In case of weak electron-phonon coupling (S<1), the zero-phonon (zero-vibrational) transition is dominant and the spectrum consists of only narrow peaks as seen in Fig. 2.3a. The excited state is located exactly above the ground state, ΔQ=0 and theoretically the band width of the transition vanishes and ends up with a narrow line. The energy of this line is equal to the energy difference between the minimum vibrational level of (m=0) the ground state and (n=0) the excited state which is shown in Fig. 2.2 as U_0.

In the intermediate coupling regime (1<S<5), in addition to the zero-phonon line extra peaks are observed and the zero-phonon line is not the strongest peak anymore in the absorption or emission spectrum. Figure 2.3b indicates a specific example of the intermediate coupling transition which is the emission spectrum of the uranyl ion (UO_2^{2+}). An example of the strong coupling case (S>5) is the broad emission band (M) in Fig. 2.3c. In this figure neither zero-phonon line nor vibrational structure can be observed. Additionally, when excitation and emission spectra are compared in the same chart, a large Stokes shift stands out.

The shape of the bands changes as a function of the Huang-Rhys parameter, S. Larger values of S lead to more symmetrical bands than smaller values of S. In the latter case, the absorption transition ends on the excited state parabola where curvature is changing rapidly and this causes an asymmetry

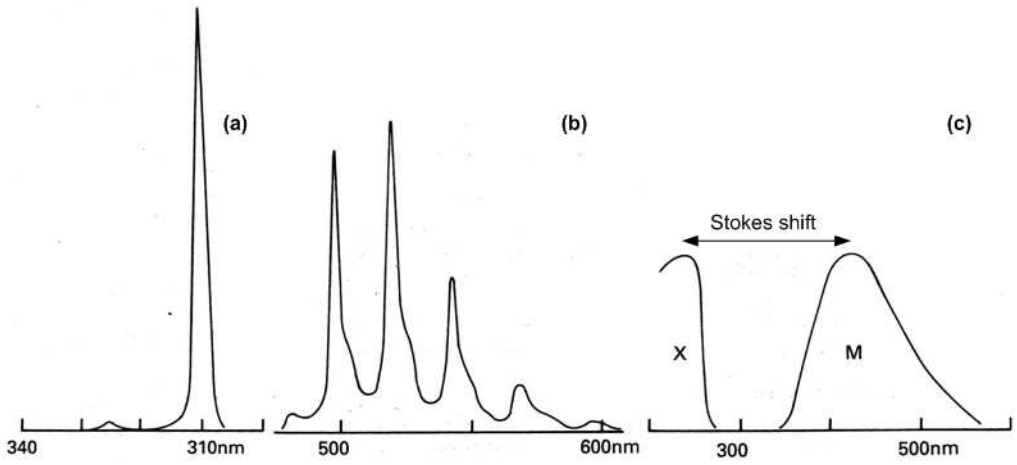

Figure 2.3: **(a)** The emission spectrum of LaB_3O_6:Gd^{3+} as an example of the weak coupling case. **(b)** The emission spectrum of UO_2^{2+} as an example of intermediate coupling. **(c)** The emission (M) and excitation (X) spectra of $CaWO_4$. The emission spectrum is an example of the strong coupling case. [22]

in the absorption band. The same phenomenon is also valid for the emission spectrum.

The spectra in Fig.2.3c consist of many overlapping lines which are related to transitions to every vibrational level of the ground state (m). If the ground and excited states have the same angular frequency, at n=0, then the transition probability is expressed by

$$W_{m0} = S^m \frac{e^{-S}}{m!} \tag{2.8}$$

This equation is useful to show the effect of electron-phonon interaction on the optical spectrum [20].

In addition to the S value, the temperature of the system has also a big influence on the band width. At a finite temperature, the transitions from the higher vibrational levels occur in addition to transition from the minimum energy level. The transition probability is proportional to the population density of levels which obeys a Boltzmann distribution. The spectral band width expressed as the full width at half maximum (FWHM) at a specific temperature (Γ(T)) is given by [23]

$$\Gamma(T) = \Gamma(0)\sqrt{coth\frac{\hbar\omega}{2kT}} \tag{2.9}$$

Where T is the absolute temperature, k is the Boltzmann constant and $\Gamma(0)$ is the band width at T=0 K and given by

$$\Gamma(0) = 2.36\hbar\omega\sqrt{S} \tag{2.10}$$

Although the transition band width increases as a function of temperature, the total intensity of the band is not changed, because the side bands' intensities increase while the intensity in the zero phonon line decreases with temperature [23].

The energy fluctuation of the initial and final states of the optical transition resulting from the uncertainty principle is the main reason of non-thermal line broadening. This fact can not be explained using the configurational coordinate model [20, 23]. A spectrum can be considered as an envelope surrounding the spectrum of sharp sidebands. The life times of the initial and final states are represented by τ and the line width of this spectrum is given by $\hbar/\tau$ [20]. The perturbation of energy states has two kinds of contributions on the band width of a photoluminescent spectrum: the first one is absorption and emission of photons (natural width) and the second one is absorption and emission of phonons. As an example, the shortest fluorescent life time of a rare-earth ion is around 10^{-7}s and this life time is correlated with 10^{-5} cm^{-1} of spectral width. However, the actual width is around 10 cm^{-1}. It means that there is an extra source in addition to "natural width". The Raman scattering of phonons has a significant contribution to the width; however, it does not affect the life time. The spectral width due to the Raman scattering of phonons, ΔE, presents a strong dependency of temperature ($\Delta E \propto T^7$). This kind of broadening is called *homogeneous broadening* [20].

In addition to temperature and energy fluctuations of the states, there are different sources which can cause line broadening. In particular, strains and defects such as impurities, vacancies or dislocations in host material around the luminescent ion cause a distribution of crystal field strength. Because of this distribution, the ions have a distributed energy and it results in an *inhomogeneous broadening* in the spectral band. Precisely, the magnitude of the inhomogeneous broadening is higher in disordered solids like glass than in crystalline solids. Additionally, this kind of broadening is more readily observed in line spectra than for broad spectra [20, 22].

2.1.4 Energy transfer between luminescent ions

After the excitation of a luminescent ion, it is possible to transfer this excitation energy to another center instead of returning to the ground state by emission. This energy transfer can occur between two chemically different luminescent ions as well as between two identical centers.

2.1.4.1 Energy transfer between two different luminescent ions

Consider two luminescent ions which are S (sensitiser or donor) and A (activator or acceptor) and the distance between them is R. If R is small enough, an interaction between the two centers can occur. If A is in the ground state and S in the exited state, the energy of S may be transfered to A. Immediately after this energy transfer, A may emit light. There are two requirements for energy transfer [21].

1. The energy difference between ground and excited states of A and S has to be equal (resonance condition). In other words, the emission spectrum of S has to overlap with the absorption of A.

2. A suitable interaction between the two systems has to be present such as an exchange interaction (wave function overlap) or an electric or magnetic multipolar interaction.

When the emission band of S and the absorption band of A overlap, the excited S can radiatively decay and the emission can then be absorbed by A. Under this condition, the emission band of S disappears at the wavelengths where A absorbs strongly. Band broadness determines the energy transfer possibility. The energy transfer from a broad-band emitter to a line absorber can only occur between nearest neighbours while transfer from a line emitter to a band absorber can be observed over long distances [21].

The energy transfer rate strongly depends on the distance between A and S and this dependency is often of the form R^{-n} with n= 6 for electric-dipole electric-dipole interaction and n= 8 for electric-dipole electric-quadrupole interaction [21].

2.1.4.2 Energy transfer between two identical luminescent ions

In this case energy transfer occurs between two identical ions. This causes energy migration which means that the emission can take place far from

where the the absorption occurs. The probability of the energy migration increases with the luminescent ion concentration. Contrary to expectations, the emission intensity of the phosphor does not increase linearly by increasing the concentration of luminescent ion, whereas one often observes a linear increase in the absorption. After a certain value, the emission intensity begins to decrease, this phenomena is called *concentration quenching*. The energy migration between the luminescent ions is one of the main reasons of this effect. By this way energy can reach remote killers or the crystal surface acting as quenching centers [21]. The other reason can be the coagulation of ions. The luminescent ions may gather as a pair or a cluster and form a quenching center [20].

The other kind of energy transfer between two identical centres is sharing the initial excitation energy by a pair of ions and it is called *cross relaxation* [21]. In this case, the energy from the relaxation of an excited ion to an intermediate excitation state is used to excite a neighbour ion from its ground state to the excited state. Therefore emission from two centers can be obtained [20].

As an example of energy transfer between the same luminescent ions, Ca_2SiS_4 doped with Eu^{2+} (at low doping concentrations) can be given. Two emission bands, yellow (at 564nm) and red (at 660 nm) are observed originating from the presence of two different sites in the orthorhombic Ca_2SiS_4 lattice [24]. In this material, the emission band of the 'yellow' center overlaps with the excitation spectrum of the 'red' center. Increasing the dopant concentration leads to a relatively stronger contribution of the 'red' center. Furthermore, the intensity of the yellow band decreases with increasing Eu concentration and this fact allows us to tune the emission color.

2.1.5 Photoionization

In addition to energy transfer between two different or identical luminescent ions, photoionization can cause a drastic change or even complete quenching of the emission. If the ground state of the luminescent ion is located in the forbidden zone between valence and conduction band and additionally its excited state is in the conduction band, an electron in the excited state can readily be ionized from the center to the conduction band. As a next step there are two possibilities:

1. The electron may recombine with a hole somewhere else, and it causes quenching in luminescence.

2. The electron in the conduction band and a hole on the ionized center may attract each other and form an exciton. This exciton bonds to the luminescent ion, therefore radiative recombination of this exciton can be observed but non-radiative recombination is also possible [21].

Photoionization which is quenching of luminescence by electron transfer is frequently observed in a combination of a center which can be easily oxidized with a center which tends to become reduced [21]. It will be considered again in § 2.1.8.2.

2.1.6 The decay of luminescence

Photoluminescence phenomena can be investigated in two groups as a function of the duration of emission in inorganic materials. *Fluorescence* as a term is commonly used to identify light emission during excitation or with a short decay time, while *Phosphorescence* implies an emission longer than 0.1 s after excitation is ended. However, the meaning of fluorescence and phosphorescence is different for organic luminescence. Emission from a singlet excited state is called fluorescence which is usually observed while emission from a triplet excited state is called phosphorescence which is rarely observed. In order to prevent any confusion I will use *persistent luminescence* for inorganic materials instead of phosphorescence [20].

2.1.6.1 Fluorescence

The fluorescence emission decay is depending on the life time of the emitting state of the center and it is generally shorter than 10 ms. The emission intensity (I(t)) at time t is described by [20]:

$$I\left(t\right) = I_0 \times exp\left(\frac{-t}{\tau}\right) \tag{2.11}$$

Here I_0 is the emission intensity at t=0, i.e. immediately after excitation and τ is the radiative decay time or decay constant.

Equation 2.11 is the simplest form of the decay profile of the luminescent intensity. Most of the time a decay profile consists of more than one component and after decay measurement, this profile can be fitted using an extension of equation 2.11 with multiple decay constants [24].

2.1.6.2 Persistent luminescence

When a persistent luminescent material is excited with high energy photons (usually UV light), it emits visible light from seconds to several hours after the excitation has ended (longer decay time). The decay rate is determined by the release of trapped charge carriers by thermal energy. Therefore the depth of the charge carrier traps, which are states in the forbidden band gap with long life time, and temperature strongly affect the afterglow property. Depth of the trap means the required minimum energy to free a captured charge carrier from the trap. Shallow (with a trap depth lower than 0.4 eV) or deep (with a trap depth higher than 1 eV) traps hinder the use of persistent luminescent materials at room temperature, therefore the trap depth should be between these two extremes (around 0.65 eV). The most common way to determine the trap depth is thermoluminescence. In this technique, light output caused by the liberation of trapped charges is measured as a function of temperature [19].

Although the exact origin of the afterglow phenomena has not been found out yet, it is thought to be governed by a quasistable state of a center or a trap and there are some suggested persistent luminescent mechanisms [19].

2.1.7 Host material

Although luminescence emission is often produced by dopant ions, the influence of the host lattice cannot be underrated. It is possible to change the optical properties of the luminescent ion by changing the host lattice. The main factors responsible for different optical properties of a luminescent ion in different host matrices are listed below [21].

- **Covalency.** When the covalency between ligands and luminescent ion increases, the interaction between the electrons of the luminescent ion reduces and electrons spread out over wider orbitals. As a result, electronic transition energy between energy levels shift to lower values and this effect is called the *nephelauxetic effect.* [20, 21]. Additionally, at higher covalency the interaction between luminescent ion and ligands increases, consequently the charge-transfer transition occurs at lower energy. This will be explained again in § 2.1.8.2 for a specific example.
- **Crystal field.** While covalency causes a global shift of the energy levels, the crystal field, which is the electric field of the surroundings on the ion under consideration, leads to a splitting of the energy levels. More details will be given in § 2.1.8.2.

Depending on the application area the required features of the host matrix change. However, several basic requirements can be outlined.

- The band gap of the host materials should be wider than the emission energy. In other words the host materials should be transparent at the emission wavelengths of the luminescent ion.
- To facilitate the substitution of dopant ions and host cations, their sizes should match. Furthermore, the oxidation state of the substituted cation should preferentially be the same as that of the dopant ion.
- Since the disordered structure of the host materials can cause a decrease in the luminescent intensity, crystalline materials are preferred [8].

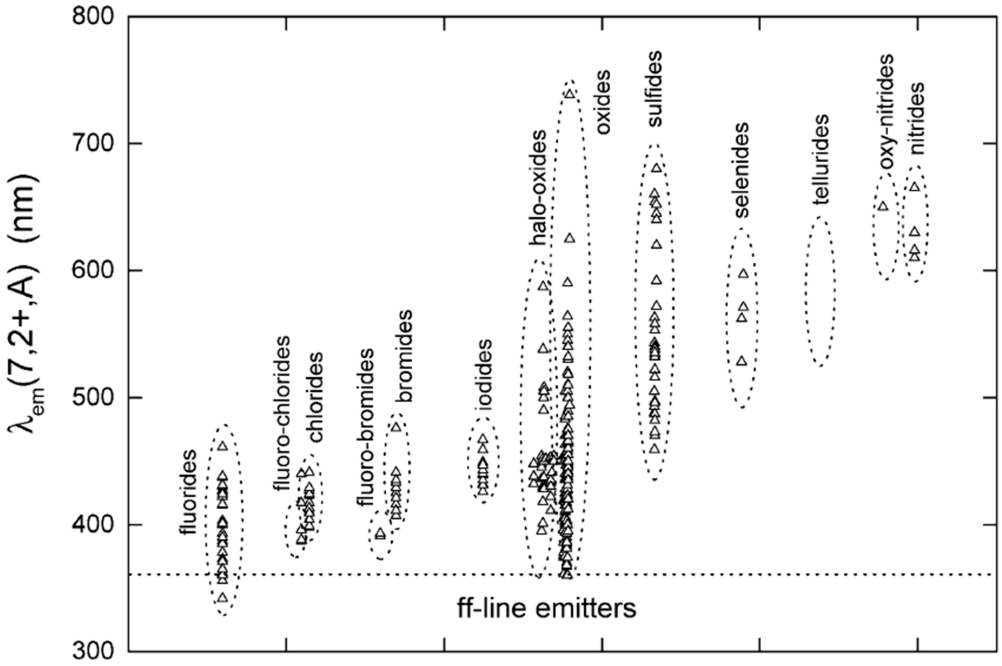

Figure 2.4: Eu^{2+} emission peak positions as a function of the compound [25].

Figure 2.4 shows the emission peak positions of Eu^{2+} in different compounds [25]. Different groups of host compounds are indicated with an ellipse. This figure summarizes very well the effect of the host material on the emission characteristics of a specific ion. As seen in the figure, in oxides and sulfides emission almost covers the whole visible region. The crystallization temperature of oxides is quite high when compared with that of sulfides [8]. Tunability of emission color and low crystallization temperature (around 500°C) make sulfides very attractive as host material.

2.1.8 Europium as luminescent ion

Europium is a member of the rare-earth metals (lanthanides) family. It was discovered in 1901 by French chemist Eugène-Anatole Demarçay. Demarçay named this element after the continent of Europe. Europium has two main application areas: it is used in thin film superconductor alloys and in luminescent materials [26]. Well-known europium doped materials are Y_2O_2S:Eu as red phosphor in television tubes [27], $SrAl_2O_4$:Eu,Dy as persistent phosphor [28] and $Sr_2Si_5N_8$:Eu as LED conversion phosphor [29].

Europium can have two oxidation states depending on the material in which it is doped. It can be trivalent (Eu^{3+}), divalent (Eu^{2+}) [25], or both of them together [30] in a solid.

2.1.8.1 Eu^{3+}

The electronic configuration of (Eu^{3+}) is given by [Xe]$4f^6$ and that of (Eu^{2+}) is [Xe]$4f^7$. Since the incompletely filled 4f orbitals are well shielded from the effects of the surrounding ions by the $5s^2$ and $5p^6$ orbitals, only a small influence of the host lattice is observed. On the contrary, the host lattice has a big influence on the 5d orbital, because it is not shielded by filled orbitals.

The energy levels of Eu^{3+} arise from a $4f^6$ configuration. These energy levels for Y_2O_2S:Eu^{3+} are indicated in the configurational coordinate model (Fig. 2.5). In the model, they are shown as parallel parabolas because of the well shielded 4f orbitals. Excitation of Eu^{3+} starts from the bottom of the minimum energy level of the ground state, $^7F_0$, and the vertical transition ends on the edge of the charge-transfer state (CTS) parabola or direct transition to $^5D_{J'}$ parabolas. After the relaxation in CTS, excitation is transfered to $^5D_{J'}$. Another relaxation occurs to the minimum energy level of excited state, $^5D_0$. Immediately after that, radiative transition takes place from $^5D_0$ to ^7F_J. The radiative transition from $^5D_{J'}$ to ^7F_J (J'=1,2) is possible with low probability. However, for this phosphor it is not possible from $^5D_3$ to ^7F_J, because $^5D_3$ lies far from the minimum of CTS curve [20, 21].

The emission spectrum of Y_2O_2S:Eu^{3+} is shown in Fig. 2.6. The sharp peaks (FWHM is around 5 nm) of the spectrum underline the intraconfigurational $4f^n$ transitions, ΔQ=0 [21]. Although the 4f-4f transitions are forbidden because of the parity selection rule, a relaxation in this rule arises due to the local symmetry of the host lattice. In Y_2O_2S, Eu^{3+} ions occupy two sites with different symmetry. Magnetic-dipole transitions ($^5D_0$ - $^7F_1$) are

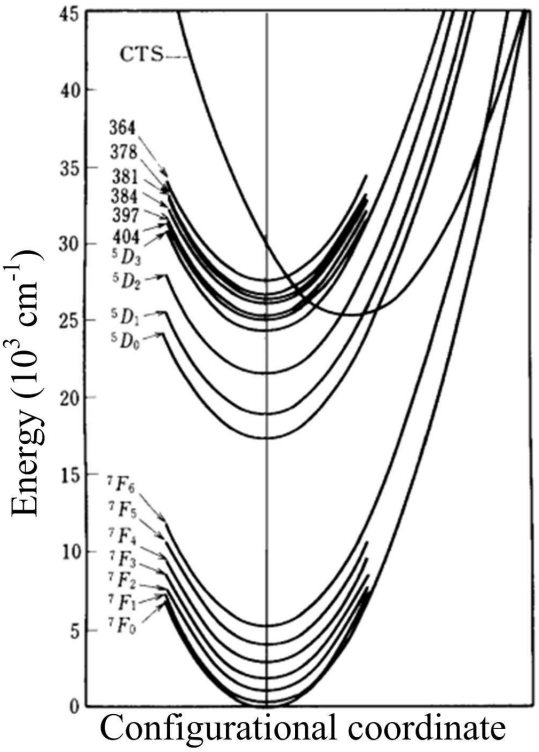

Figure 2.5: Configurational coordinate model of Y_2O_2S:Eu^{3+} [20].

mainly observed from the site without inversion symmetry, forced electric-dipole transitions ($^5D_0$ - $^7F_{2,4}$) are predominantly observed from the site with inversion symmetry [21, 27]. Because of the forbidden character of the 4f-4f transition, the life time of the luminescence is in the range of milliseconds.

2.1.8.2 Eu^{2+}

In most crystals, the lowest excited state of the $4f^6$5d configuration of Eu^{2+} is located at lower energy than that of $4f^7$, which leads to a broad-band emission. The emission color depends on the host material and can be changed from UV to red. Eu^{2+} has a relatively long life time (10^{-5}-10^{-6} s) for an allowed transition. The excited state $4f^6$5d contains (spin) octets (8) and sextets (6) while the ground state $4f^7$ (^{8}S) contains only octets. Since only states with the same total spin quantum number are "spin-allowed", the sextet part of the exited state contributes to the "spin-forbidden" transition and it leads to a relatively long life time.

The 5d electron level of Eu^{2+} is responsible for broad-band emission. Since it

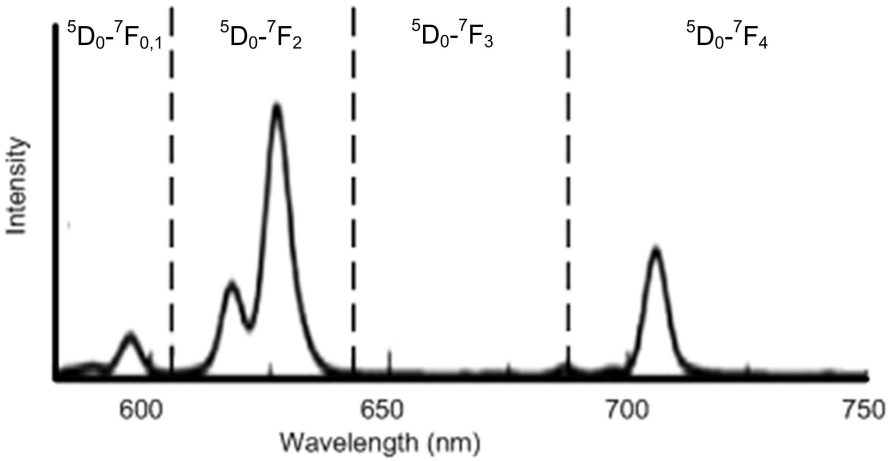

Figure 2.6: Emission spectrum of Y_2O_2S:Eu^{3+}. $^5D_0 \rightarrow {}^7F_J$ transitions are indicated at top of the figure [27].

is not shielded from the surroundings in contrast to the 4f levels, the optical transition energy from $4f^6 5d$ to $4f^7$ and thus the emission color can easily be tuned by changing the host material.

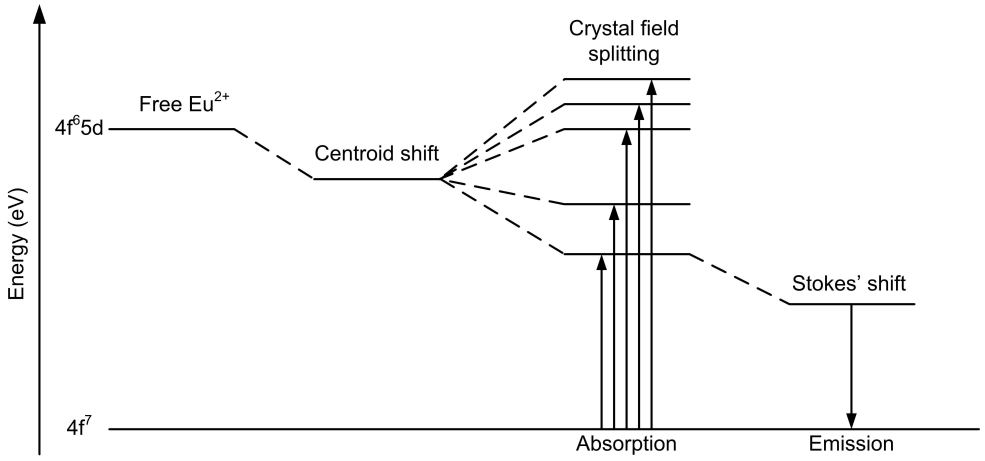

Figure 2.7: Schematic representation of the influence of the host lattice on the free Eu^{2+} energy states [20].

Several effects influence the Eu^{2+} ion in a crystal and due to this effect Stokes shift, centroid shift and crystal field splitting on the $4f^6 5d$ can be observed [31]. Figure 2.7 illustrates how the $4f^6 5d$ state of the Eu^{2+} ion is affected by the host lattice. The energy difference between the d- and f-electrons is changed by the covalency between the Eu^{2+} ion and the lig-

and bond, and the crystal field strength. When the covalency increases, the interaction between the electrons of the Eu^{2+} ion reduces and the energy difference of the 4f-5d levels decreases (nephelauxetic effect). This decrease in the energy difference of the 4f-5d levels is called *centroid shift* [27]. The average energy of the 5d state is shifting to lower values due to the centroid shift and crystal field splitting. The total decrease because of these two effects is called the *red shift* (D). Red shift of Eu^{2+} shows a strong dependency on the host material. The lowest $4f^6 5d$ level, which is already lowered due to the red shift, is further lowered by the Stokes' shift due to the lattice relaxation [31].

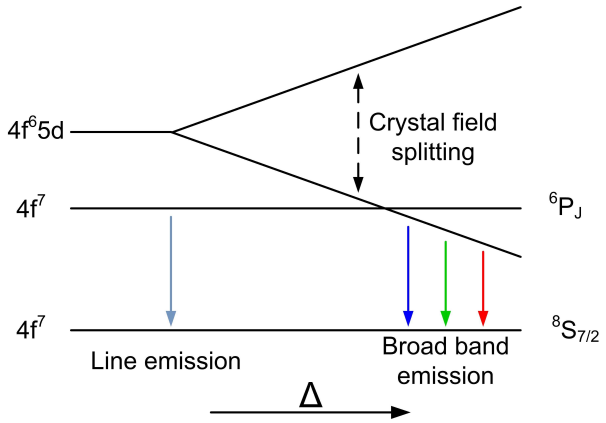

Figure 2.8: Energy separation of the centroid shifted $4f^6 5d$ level in Eu^{2+} as a function of the crystal field strength (Δ) [20].

There are three types of Eu^{2+} emissions, namely 5d-4f broad band emission, 4f-4f line emission, and anomalous Eu^{2+} emission [25]. In most of the crystals Eu^{2+} has broad band emission due to 5d-4f transition. Splitting in the d level of Eu^{2+} as a function of the crystal field strength is indicated in Fig. 2.8. As seen in this figure the energy levels of the $4f^7$ state, ^6P_J, are located lower than that of the $4f^6 5d$ level. Sometimes, the 5d-4f broad band emission can be observed together with 4f-4f line emission for low crystal field strength, such as for $BaAlF_5$ and $SrAlF_5$ [25].

When an electron from the 5d level is photo-ionized to the conduction band, it leaves a hole. The recombination of the electron with the hole can result in an emission which is called *anomalous emission*. It is characterized by a very large Stokes' shift [20, 25].The emission at 878 nm from BaS:Eu^{2+} is an example for anomalous emission, normally a blue shift is expected in the emission of the BaS:Eu^{2+} when compared to SrS:Eu^{2+} (620 nm) and CaS:Eu^{2+} (652 nm) due to the smaller crystal splitting [32].

Chapter 3

Material Preparation

This chapter discusses the sample preparation techniques we utilized in this research. The chapter starts with the synthesis of CaS:Eu luminescent particles via a solvothermal method. We use two techniques to encapsulate CaS:Eu particles, the first one being a sol-gel method. After the introduction on the sol-gel method, the preparation procedures of TiO_2 and Al_2O_3 via the sol-gel technique are explained in detail. The second technique is atomic layer deposition, which is briefly introduced. Then the experimental setup to deposit Al_2O_3 on CaS:Eu is described. Finally, this chapter ends with the description of the preparation of $CaAl_2O_4$:Eu,Nd luminescent powders.

3.1 Preparation of CaS:Eu

CaS:Eu particles were prepared with a solvothermal synthesis method [33]. The starting materials were $CaCl_2.2H_2O$ (Alfa Aesar, 99%), $EuCl_3$ (Alfa Aesar, 99.9%) and sulfur powder. Ethylenediamine ($C_2H_8N_2$), having a boiling point of 117.3°C, a critical temperature of 319.9°C and a critical pressure of 6.21 MPa, was used as solvent. $CaCl_2.2H_2O$ and $EuCl_3.nH_2O$ were dried at 170°C for 2 h under a nitrogen flow and ethylenediamine was cooled to 2°C (P_{vapour}=14.3 hPa at 20°C). An appropriate amount of $CaCl_2$, $EuCl_3$ and sulfur powder (in 15% excess) was added into a Teflon-lined autoclave (Autoclave France Eze Seal, 60ml) and 12.5 ml cooled ethylenediamine was added. The autoclave was maintained at 200°C for 12 h (corresponding to an ethylenediamine vapour pressure of 8300 hPa) and then cooled to room temperature naturally (in about 4 h).

After cooling down, ethylenediamine was separated from the reaction product, which precipitated at the bottom of the Teflon liner. The unreacted

chlorides and sulfur in the autoclave were removed by washing the reaction product with absolute ethanol. Chlorides and sulfur could be separated from sulfides by sonicating the reaction product at about 50°C. This procedure was repeated several times, until only sulfides remained. In order to characterise and make CaS:Eu particles ready for encapsulation, the reaction product was dripped on (100)-oriented silicon wafers and dried in air at 40°C. This procedure was repeated a couple of times.

3.2 Non-Aqueous Sol-Gel

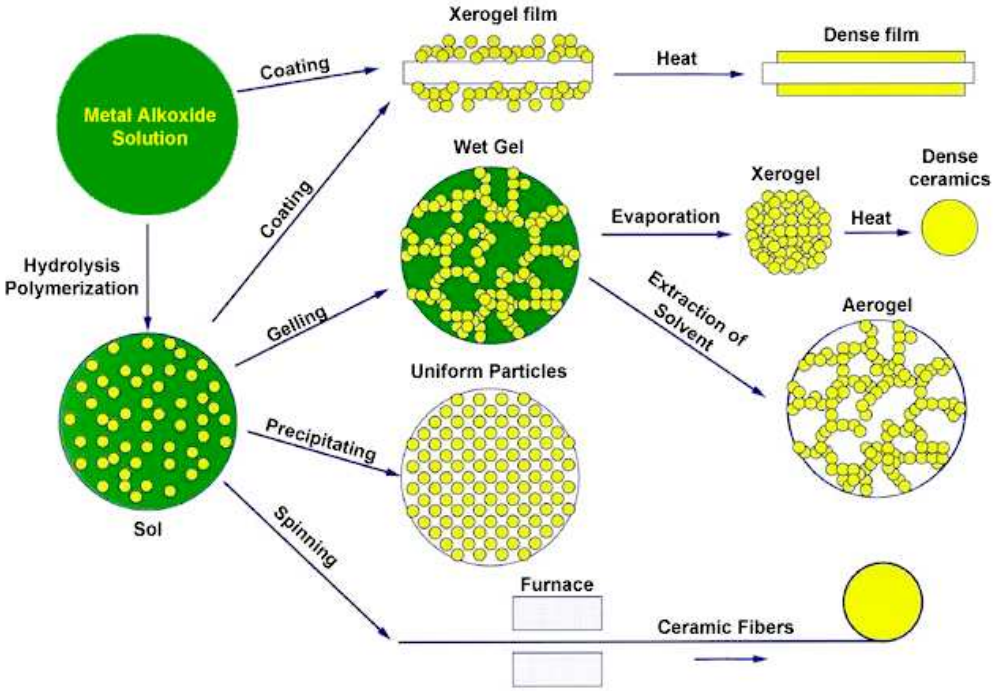

Figure 3.1: Schematic overview of the sol-gel process [34].

The sol-gel process can roughly be defined as the formation of an inorganic solid from a precursor solution by chemical means [35]. By the chemical transformation of the molecular precursor, a final oxidic network with different features can be synthesized [1, 2, 35] as illustrated in figure 3.1. This technique offers the possibility of obtaining metastable materials, achieving superior purity and compositional homogeneity of the products at moderate temperatures with simple laboratory equipment. Generally, either an inorganic metal salt or a metal organic species like a metal alkoxide or acetylacetonate is selected as precursor. Alkoxide precursors are more favourable

than the inorganic metal salts since hydrolysis of the inorganic salts is quite complicated [36] and extra impurities frequently remain in the final oxide materials [3].

There are two crucial reactions leading to an oxide network starting from a metal alkoxide:

(1) Hydrolysis:

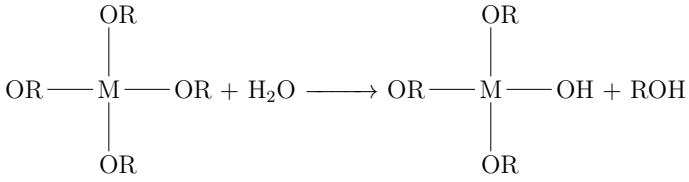

(3.1)

(2) Condensation:

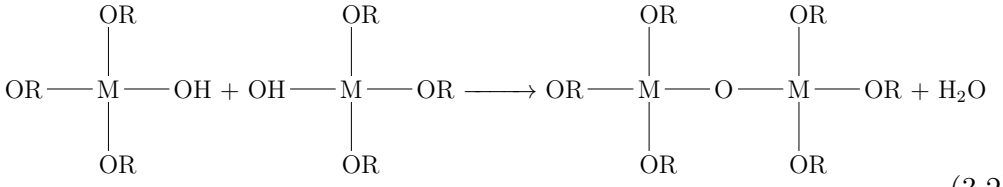

(3.2)

and/or

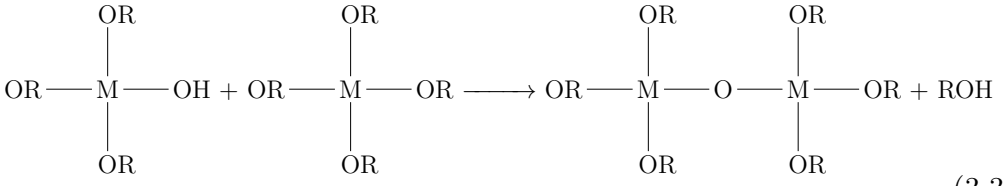

(3.3)

In these chemical equations, M indicates a four-valence metal ion, (OR) is an alkoxy group, (OH) represents a hydroxyl group and (ROH) is an alcohol. The reaction in which an (OH) becomes attached to the metal ion is called hydrolysis. Depending on the water content and pH of the environment, hydrolysis may be accomplished (all (OR) groups are replaced by (OH)) or stopped as the metal is only partially hydrolyzed [1]. Simultaneously, in the condensation reaction partially hydrolyzed molecules link together and produce metal oxide (M-O-M) bonds by producing water (equation 3.2) and/or alcohol (equation 3.3). Polymerization takes place by continuous condensation reactions. The solution containing a stable dispersion of polymers is called sol. There are some parameters which affect the reaction kinetic of hydrolysis and condensation, and lead to variation on the final network and product properties. These parameters are listed as follows [37]:

- Characteristics of the precursor
- Water/alkoxide ratio
- Selection of alcohol
- Catalyst (pH of the environment)
- Reaction temperature

In addition to that, the order of the reaction has a significant effect on the network formation. Heat treatment parameters (time, temperature and atmosphere) have also a big influence on the final product [37].

3.2.1 Effect of precursor

The reaction kinetic is primarily determined by the size and structure of the alkyl group around the metal atom. Larger alkyl groups lead to more steric hindrance and thus slower reactions [1, 2, 37]. For example, the hydrolysis of $Si(OCH_3)_4$ (tetramethoxy silane) is faster than $Si(OC_2H_5)_4$ (tetraethoxy silane) and data for other silicon alkoxides are shown in table 3.1. The nature of the alkyl chain affects not only hydrolysis but also the condensation reaction. The gelation time of silicon alkoxides increases with the length of the alkyl chain [36].

R	k (10^{-2}l.mol^{-1}s^{-1}(H*)$^{-1}$)
C_2H_5-	5.1
C_4H_9-	1.9
C_6H_{13}-	0.83
$(CH_3)_2CH(CH_2)_3CH(CH_3)CH_2$	0.30

Table 3.1: Rate constant k of hydrolysis of tetra-alkoxysilanes $Si(OR)_4$ [2].

The other example of the reaction kinetic is the hydrolysis rate comparison between $Al(OC_4H_9)^s_3$ (aluminium sec-butoxide) and $Al(OC_3H_7)^i_3$ (aluminium isopropoxide): The alkoxides with short alkyl groups typically lead to larger polymer units which are relatively rich with oxygen [37]. The last example is related to the $Ti(OC_4H_9)^s_4$ (titanium butoxide) series, the bond structures are shown in figure 3.2.
The hydrolysis rate decreases depending on the size of alkoxide group, the sequence of the rate from highest to lowest is in titanium butoxide

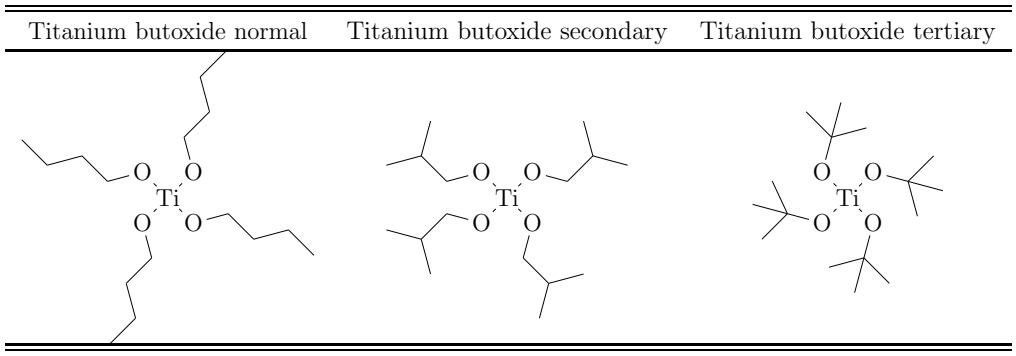

Figure 3.2: Bond structure of the titanium butoxide series.

tertiary>secondary>normal [38].

Alkoxide	δ(M)
$Zr(OEt)_4$	+0.65
$Ti(OEt)_4$	+0.63
$Nb(OEt)_5$	+0.53
$Vo(OEt)_3$	+0.46
$W(OEt)_6$	+0.43
$Si(OEt)_4$	+0.32

Table 3.2: Electronegativity δ(M) on the metal ion for selected metal ethoxides [36].

The nature of the metal atom is as important as the type of alkoxide groups. Table 3.2 shows the comparison of partial charge of metal δ(M) in some transition metal ethoxides with silicon ethoxide. As seen in the table, the partial positive charge of the transition metals is higher than that of silicon. It expresses why hydrolysis and condensation reactions of transition metal alkoxides are faster than those of silicon alkoxides. The other parameter which affects the hydrolysis and condensation kinetic is the unsaturation (N-z). Here N is the coordination number, and z is the oxidation state of the metal (M) atom. Larger (N-z) promotes the hydrolysis reaction [1]. Unsaturation (N-z) of a few tetravalent metals in alkoxides is listed in table 3.3.

As indicated in table 3.3 unsaturation decreases from Ce to Si, it means that hydrolysis reactivity decreases as Ce$\gg$Zr>Ti$\gg$Si. Aluminium alkoxides

Cation	N	(N-z)
Si	4	0
Ti	6	2
Zr	7	3
Ce	8	6

Table 3.3: Unsaturation (N-z) of a few tetravalent metals in alkoxides [39]

.

$Al(OR)_3$ are quickly hydrolyzed in water by producing aluminium mono- or tri-hydroxides [40]. It can simply be explained by unsaturation of the Al^{3+} cation, given that the coordination number of Al^{3+} is 6.

3.2.2 Effect of water/alkoxide ratio

The molar ratio of water to metal alkoxide precursor ($h=H_2O/M(OR)_n$) is the main parameter affecting the nature of the oxide. For the hydrolysis of $M(OR)_4$, theoretically an h value of 2 is enough since water is formed during condensation reaction as a by-product. Additionally, water can be produced by different side reactions such as reaction between alcohols (OR) and carboxylic acids (R'COOH);

$$ROH + R'COOH \rightarrow RCOOR' + H_2O \tag{3.4}$$

Nevertheless, an excess amount of water ($h \gg 2$) is not sufficient to complete hydrolysis and condensation of $M(OR)_4$ and obtain MO_2 [1, 36] because of a reaction kinetic $\delta(OR)>0$ (table 3.4). The most obvious result of an increasing h is acceleration of the hydrolysis reaction. It can also cause more complete hydrolysis and formation of monomers before the condensation process begins. This fact indicates condensation can be regulated by changing the h value.

$h<1$: In this case,the alcohol producing condensation is prevalently observed. Under this condition, an infinite network is rarely produced. Neither gelation nor precipitation can be obtained unless hydrolysis is not carefully controlled.

$1 \leq h \leq z$: Chain polymers can be obtained under such conditions. Table 3.4 indicates that the first step of the hydrolysis ($h<2$) quickly occurs because of $\delta(OR)<0$ and $\delta(Ti)>0$. The partial charge of the (OR) group $\delta(OR)$ becomes more and more positive when $h \geq 2$. This puts a limitation on replacing (OH)

Precursor	h	$\delta(O^iPr)$	$\delta(OH)$	$\delta(^iPrOH)$	$\delta(H_2O)$	$\delta(Ti)$
$Ti(O^iPr)_4$	0	-0.15	-	-	-	-
$Ti(O^iPr)_3(OH)$	1	-0.08	-0.38	+0.02	-0.28	+0.62
$Ti(O^iPr)_2(OH)_2$	2	+0.04	-0.36	+0.15	-0.25	+0.64
$Ti(O^iPr)(OH)_3$	3	+0.28	-0.32	+0.41	-0.18	+0.67
$Ti(OH)_4$	4	-	-0.19	-	+0.01	+0.76

Table 3.4: Effect of h=$H_2O/M(OR)_n$ on the charge distribution in monomeric $Ti(O^iPr)_4$ precursor [36].

with (OR).

h>z: If hydrolysis occurs under excess water condition, cross-linked polymers, particulate gels or precipitation can be obtained. Yoldas [41] reported that the oxide contents of the polymers increased as a function of hydrolysis water.

3.2.3 Effect of alcohol

For alcohol interchange between a metal alkoxide and an alcohol, the equilibrium reaction can be written as follows:

$$M\left(OR\right)_n + R'OH \rightleftharpoons M\left(OR\right)_{n-1}\left(OR'\right) + ROH \tag{3.5}$$

The alcohol interchange possibility has to be taken into account, when metal alkoxide is dissolved in another alcohol than the parent one, because this ligand exchange can change the molecular structure and hydrolytic properties of the metal alkoxide. Consequently, solvent modification by alcohol exchange changes the oxide properties. For example; the surface area of SiO_2 is 305 m^2/g for $Si(OMe)_4$/MeOH and only 169 m^2/g for $Si(OMe)_4$/EtOH [42]. The facility for the interchange strictly depends on two parameters. The first one is the nature of the metal atom; $\delta(M) \gg 0$ facilitates the interchange. For example, transition metal alkoxides show faster exchange rates than silicon alkoxides [36]. The second one is the steric hindrance of the alkoxy group; if R' is less sterically bulky than R, this promotes the interchange reaction. As an example, the alcohol exchange rate decreases as OMe>OEt>O^iPr>OBu^t [1, 36].

3.2.4 Effect of catalyst

To produce oxides with different properties, hydrolysis and condensation rates are regulated by adding acids or bases. Depending on the type of catalyst, the reaction mechanism changes.

Acid catalyst: When an acid is added into the solution, a quick protonation of the negatively charged OR group occurs, this enhances the elimination of ROH molecules. Hence, substitution of all OR groups becomes theoretically possible. The protonation possibility of different alkoxide sides are not the same, and it affects the condensation pathway. The figure 3.3 shows a typical hydrolyzed polymer. [36]:

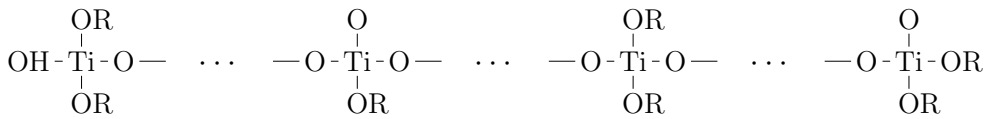

Figure 3.3: Partially hydrolyzed titanium oxo polymer.

Site	δ(OR)	δ(Ti)
A	-0.1	+0.70
B	+0.22	+0.76
C	+0.04	+0.71
D	-0.08	+0.68

Table 3.5: Charge distribution according to the partial-charge model within a titanium oxo polymer.

Partial charges of the (OR) group depending on the sites A-D are listed in table 3.5. As seen in the table the facility for protonation decreases as D$\gg$A$>$C$\gg$B. Consequently, OH groups are mostly generated at the end of the chain [38]. Therefore, under such an acidic condition, condensation occurs between these rapidly formed hydrolyzed species and results in the formation of linear polymers rather than highly branched ones [36]. If a non-stoichiometric amount of water (h is low) is used in the presence of an acid, spinnable sols (capable of being drawn into a fiber) or monolithic gels can be obtained [1].

Base catalyst: In the course of basic catalysts, the reactive precursor attacks the positively charged metal atom. It was observed that using base catalyst for the hydrolysis of $Si(OR)_4$ increased the reactivity; however, the hydrolysis of $Ti(OR)_4$ with base catalyst was more difficult than in acidic or neutral conditions [1,36]. It can result from a decrease of positive charge of Ti by nucleophilic addition of OH^- [1,36]. Consequently, it is expected that the condensation kinetic increases on a regular basis. δ(Ti) values depending on the sites A-D are inserted in table 3.5. Based on these values, it can be expressed that the order of the reactivity for nucleophilic attack decreases as B$\gg$C$\approx$A>D [1, 36]. As seen in figure 3.3, under base catalyzed conditions (also in hydrolysis) nucleophilic fragments such as M-O^- are formed at the middle instead of the end of the chain. Highly branched, more compact polymers are expected to be formed [1, 36]. It may result in mass or surface fractals or uniformly porous materials depending on hydrolysis and condensation ratios.

3.2.5 Effect of reaction temperature

Reaction temperature has also an influence on the oxide product. Higher reaction temperature leads to formation of larger polymers with higher metal oxide contents since diffusion of the molecules is easier at higher temperature [37, 40].

3.2.6 Aqueous versus non-aqueous

Depending on the solvent type, the sol-gel method can be divided into two groups, distinguishing between aqueous and non-aqueous sol-gel methods. In an aqueous sol-gel process, the oxygen for the formation of the nanoparticles is supplied by the water molecules. In a non-aqueous sol-gel process, the oxygen is provided by the solvent (ethers, alcohols, ketones, or aldehydes) or by the organic constituent of the precursor (alkoxides or acetylacetonates) [43]. Although the aqueous sol-gel method is a very powerful technique to synthesize a wide range of materials, there are some limitations on the applications. For example, when precursors with high chemical reactivity such as transition metal alkoxides are used, the hydrolysis reaction can result in precipitation [3,36]. Additionally, the aqueous sol-gel technique has some drawbacks in specific application areas. Er^{3+} doped Al_2O_3 is a well known material as planar waveguide and Al_2O_3 improves the dispersion of Er^{3+}, thus the luminescence efficiency and decay time increase. However, using water during the preparation encourages hydrolysis of Er^{3+} and accordingly the dispersion of Er^{3+} decreases [4, 5]. Alkaline earth sulfide phosphors

are very attractive for display applications, electroluminescent devices, optical information storage and phosphor-converted white light emitting diodes (LEDs) [8]. Notwithstanding, because of the limited stability with respect to water and other atmospheric components, it is not obvious to use sulfides as phosphor hosts. This problem can be solved via encapsulation with an inert film like Al_2O_3 [6,7]. But an excess amount of water used for Al_2O_3 synthesis can lead to decomposition during the encapsulation process instead of protection. These problems can be overcome using a non-aqueous sol-gel technique.

During this study we used the non-aqueous sol-gel approach for two purposes. The first one is the synthesis of metal oxides to encapsulate CaS:Eu particles prepared via solvothermal synthesis. We synthesized two metal oxides namely TiO_2 and Al_2O_3 for this aim. The second one is the synthesis of a luminescent material. We obtained persistent luminescent $CaAl_2O_4$:Eu, Nd via a non-aqueous sol-gel method.

3.3 TiO_2 thin films powders and protection layers

Titanium dioxide thin films and bulk powders were prepared using two non-aqueous sol-gel techniques, summarized in Figure 3.4. The first technique was published by Ungureanu et al. [44] and Legrand-Buscema et al. [45] and the second technique was published by Kajitvichyanukul and Amornchat [46].

In the first technique (method 1), sols were synthesized using titanium(IV) n-butoxide ($Ti(O\text{-}nBu)_4$) (Alfa Aesar, 98%) as precursor and n-butyl alcohol (n-BuOH) (Alfa Aesar, 99.4%) as solvent. Acetylacetone (AcAcH) (Alfa Aesar, 99%) was added as chelating agent to decrease the reactivity of $Ti(O\text{-}nBu)_4$ [44, 45]. In order to begin hydrolysis via an esterification reaction, glacial acetic acid (Alfa Aesar, 99%) was used. To prepare a stable precursor solution, first n-BuOH and acetylacetone were mixed, then $Ti(O\text{-}nBu)_4$ was added to the solution. The molar ratio between acetylacetone and $Ti(O\text{-}nBu)_4$ was 0.3. This mixture was stirred for 30 minutes at room temperature. Acetic acid was slowly added into the alkoxide solution under stirring for 30 minutes at room temperature. A molar ratio between acetic acid and $Ti(O\text{-}nBu)_4$ of 0.2 was utilized. Sols with two different concentrations (0.5 M and 2.4 M) were synthesized (Fig. 3.4a), with viscosity of 3.77 mPa.s and 6.85 mPa.s, respectively. Immediately after the preparation both sols were yellowish and transparent. They remained stable for more than 6 months.

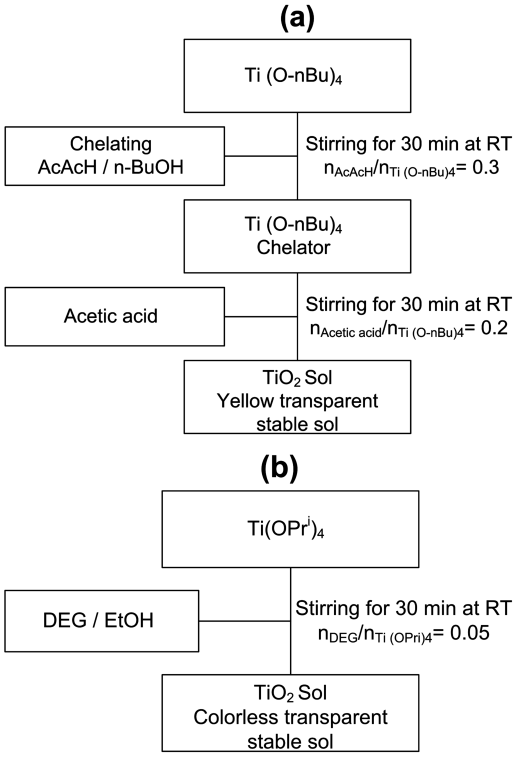

Figure 3.4: The experimental procedure for preparing stable sol of titanium dioxide by method 1 adopted from [44, 45] **(a)** and method 2 adopted from [46] **(b).**

In the second technique (method 2), stable sols were synthesized using Ti-isopropoxide $Ti(O^iPr)_4$ (Alfa Aesar, 97%) as precursor and ethanol (EtOH) (Rotipuran, 99.8%) as solvent. Diethylene glycol (DEG) (Alfa Aesar, 99%) was used to stabilize the sols [46]. $Ti(O^iPr)_4$ was introduced into the mixture of ethanol and DEG. After the solution was stirred for 30 minutes at room temperature, it was transparent and without precipitation. A sol was prepared in this way. The composition of the sol was 1:1:20 for $Ti(O^iPr)_4$, DEG and ethanol in molar ratio, respectively (Fig. 3.4b). The viscosity was 2.26 mPa.s.

In both cases, water was not added into the solution for the hydrolysis reactions. It was partially supplied via an esterification reaction between the glacial acetic acid and n-BuOH for method 1 and via the residual water in ethanol (0.1%) for method 2. Therefore the molar ratio between TiO_2 and water can be estimated at about 1:0.2 and 1:0.05, respectively. Thus, the hy-

drolysis reactions were performed with substoichiometric amounts of water. In this case, partially hydrolysed species are initially formed and concurrently condensation reaction occurs between them [1].

Structural properties were studied for powder samples which were obtained by heat treatment for 2 hours at different temperatures of 250, 320, 350, 400, 450, 500, 550, 600, 620, 700 and 800°C with a heating rate of 10°C/min in air. Single TiO_2 layers were deposited on (100)-oriented silicon wafers and Corning 1737 sodium-free borosilicate glass by spin coating with different spinning rates from 2000 to 6000 rpm for 20 seconds at room temperature. Coated substrates were heat treated at 400 and 500°C in air for 30 minutes and the heating rate was 10°C/min.

In order to protect CaS:Eu luminescent particles against moisture and CO_2 in the air, particles were coated with TiO_2 layers. TiO_2 synthesized following the first method was used for this purpose. Two sols with different concentrations (0.5 M and 2.4 M) were synthesized, with viscosity of 3.77 mPa.s and 6.85 mPa.s, respectively. CaS:Eu particles on silicon substrates were coated with TiO_2 solutions using spin coating with a rotation speed of 800 rpm for both TiO_2 sols for 20 seconds. The coated substrates were then heat treated for 30 minutes in air at 400°C with a heating rate of 10°C/min.

3.4 Al_2O_3 thin films

Although the main purpose to synthesize Al_2O_3 is to encapsulate CaS:Eu particles, it is also very important to understand the effect of the sol on the luminescent particles. Therefore, during this study Al_2O_3 was prepared via two different techniques. In the first year of this research, Al_2O_3 condensed solutions were synthesized following the route described by Yang et al. [47]. Very stable (more than 1 year) alumina sols were synthesized using aluminium isopropoxide [$Al(OC_3H_7)_3$] as precursor, isopropanol (^{i}PrOH) as solvent, nitric acid as catalyst, and acetylacetone (AcAcH) as chelating agent, summarized in Figure 3.5. The solution was prepared using ^{i}PrOH and (2 mol/l) of AcAcH, then $Al(OC_3H_7)_3$ was slowly added into the solution under stirring for 1 h at 65°C. The molar ratio between $Al(OC_3H_7)_3$ and AcAcH is 1:2. Water was added into the solution for hydrolysis with a molar ratio of 0.85:1 for water and $Al(OC_3H_7)_3$, followed by adding ^{i}PrOH to adjust the concentration of $Al(OC_3H_7)_3$ to 30 g/l. After the modified solution was stirred for 3 h at 65°C, the pH was adjusted to 3 with concentrated nitric

acid (HNO_3). The water concentration was approximately 9.5 mg/ml. The Al_2O_3 sol was kept at 75°C until getting a sol having a viscosity in the range of 5-6 mPa.s. Silicon substrates covered with CaS:Eu particles were coated with Al_2O_3 viscous solutions using spin coating with a rotation speed of 800 rpm for both Al_2O_3 sols. The coated substrates were then heat treated for 10 minutes in air at 500°C with a heating rate of 10°C/min. As explained in the experimental procedure, for this synthesis water and a strong acid (HNO_3) were used and both of them are detrimental for CaS:Eu luminescent particles. Therefore it was very useful for us to see the degradation effect of the sol onto particles (§8.3.1.

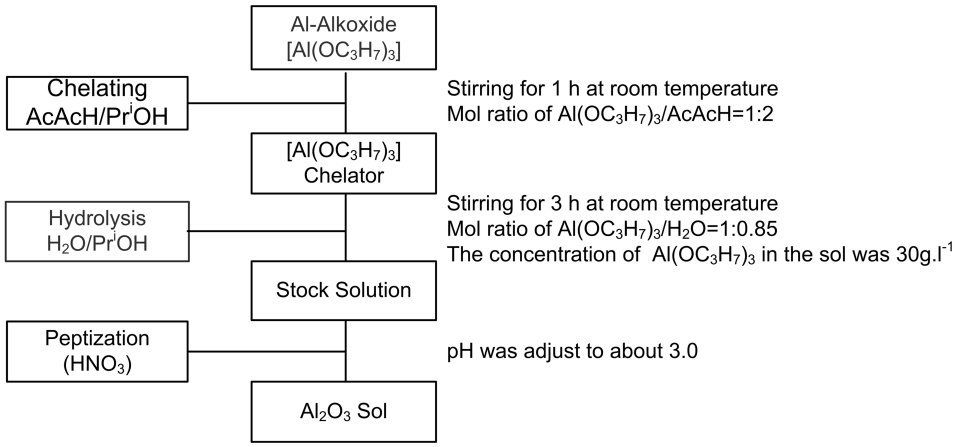

Figure 3.5: The experimental procedure for preparing stable sol of alumina by method 1 [47].

In the second technique, which was developed in-house, aluminium oxide sols were prepared via a non-aqueous sol-gel technique. Three sols were synthesized using anhydrous ethanol (EtOH) (Alfa Aesar, 90%), isopropanol (^{i}PrOH) (Acros, 99.5%) and n-butyl alcohol (n-BuOH) (Alfa Aesar, 99.4%) as solvent. Aluminium sec-butoxide ($Al[O(CH_3)CHC_2H_5]_3$) (Alfa Aesar, 95%) was used as a precursor. Acetylacetone (AcAcH) (Alfa Aesar, 99%) was added as chelating agent to decrease the reactivity of the precursor. The molar ratio between acetylacetone and aluminium sec-butoxide was 1. The concentration of the sols was adjusted to 0.5 M. To prepare stable sols, first the solvent and acetylacetone were mixed, and then aluminium sec-butoxide was added to this mixture. Eventually the solution was stirred for 6 hours at 40°C. Transparent solutions were readily obtained using ^{i}PrOH and n-BuOH as solvent via this route. To obtain a transparent solution using EtOH as a solvent, it was necessary to stir at 40°C. The sol prepared with n-BuOH was

stable for more than 1 year while the sols prepared with EtOH and ^{i}PrOH were stable for 1 and 8 months, respectively, after which precipitation occurred.

Single aluminium oxide layers were deposited on (100)-oriented silicon wafers by spin coating with different spinning rates from 1000 to 6000 rpm for 20 seconds at room temperature. Coated substrates were heat treated at 450 and 650°C in air for 30 minutes and the heating rate was 10°C/min. The layers for IR measurements were deposited on double side polished and (100)-oriented Czochralski-grown silicon wafers by spin coating with a spinning rate of 2000 rpm for 20 seconds at room temperature. After the coating process, samples were heat treated at different temperature from 200°C to 500°C in air for 30 minutes and the heating rate was 10°C/min. Aluminium oxide layers for transparency measurements were also prepared by spin coating on Corning 1737 sodium-free borosilicate glass substrates at 2000 rpm for 20 seconds at room temperature and then heat treated at 500°C in air for 30 minutes (heating rate of 10°C/min).

Protection layers were also prepared via the second technique using n-butyl alcohol (n-BuOH) (Alfa Aesar, 99.4%) as solvent [7]. The deposition of the alumina coatings on CaS:Eu^{2+} particles was performed by spin coating at 800 rpm for 20 seconds. After coating, the coated phosphor layers were heat treated for 30 minutes in air at 500°C with a heating rate of 10°C/min to remove the organic groups.

3.5 $CaAl_2O_4$:Eu,Nd

$CaAl_2O_4$:Eu,Nd luminescent powders were prepared in three stages via a non-aqueous sol-gel method.

In the first stage, the optimum synthesis temperature was determined. Undoped calcium aluminium oxide ($CaAl_2O_4$) powder was successfully synthesized using calcium nitrate tetrahydrate ($Ca(NO_3)_2.4H_2O$) (Alfa Aesar, 99%) and aluminium sec-butoxide ($Al[O(CH_3)CHC_2H_5]_3$) (Alfa Aesar, 95%) as precursor, n-butyl alcohol (n-BuOH) (Alfa Aesar, 99.4%) as solvent and acetylacetone (AcAcH) (Alfa Aesar, 99%) as chelating agent. The molar ratio between acetylacetone and aluminium sec-butoxide and the molar ratio between n-butyl alcohol and aluminium sec-butoxide were adjusted as 1 and 100, respectively. Initially, the 2/3 of n-butyl alcohol and acetylacetone were mixed, and then aluminium sec-butoxide was added to this mixture. Then

the solution was stirred for 4 hours at 40°C. At the same time calcium nitrate tetrahydrate was dissolved in the 1/3 of n-butyl alcohol at 40°C, which took around 20 minutes. Eventually, calcium nitrate tetrahydrate solution was added into the aluminium sec-butoxide solution and the mixture was stirred for 4 hours at 40°C. Very stable and transparent solutions were readily obtained via this route. $CaAl_2O_4$ powders were obtained by heat treatment for 1 hour at different temperature of 800, 900, 950, 1000, 1100 and 1200°C with a heating rate 5°C/min in air.

In the second stage, the influence of the europium concentration was studied. Eu doped $CaAl_2O_4$ powders were prepared in the same way as in the first stage except from adding hydrated europium nitrate into the calcium nitrate tetrahydrate solution and dissolving at 40°C. Eu doped $CaAl_2O_4$ powders were obtained by heat treatment for 1 hour at 900 and 1000°C with a heating rate 5°C/min in air. In this way, we prepared 0.5, 1, 2 and 3% Eu doped $CaAl_2O_4$ powders. In order to reduce Eu^{3+} to Eu^{2+} two different methods were used; namely, annealing under H_2/N_2 (10%/90%) atmosphere and electron beam annealing in vacuum. In the first annealing technique, powders were annealed for 20 minutes at 500, 600, 700, 800, 900 and 1000°C with a heating rate 5°C/min under H_2/N_2 (10%/90%).

In the last stage, the optimum ratio between europium and neodymium for the best persistent luminescent property was examined. Eu and Nd doped $CaAl_2O_4$ powders were synthesized in the same way as the preparation of $CaAl_2O_4$:Eu except from adding neodymium(III) nitrate hexahydrate (Alfa Aesar, 99.9%) into the calcium nitrate tetrahydrate and hydrated europium nitrate mixture and dissolving at 40°C. Eu^{3+} was reduced to Eu^{2+} via electron beam annealing.

3.6 Preparation Instruments

3.6.1 Classic tube furnace annealing

During this study all thermal annealing processes were performed in a Nabertherm 65 cm-long tube furnace. This furnace with an uniform heated length of 25 cm (± 5°C at 1000°C) features highly reproducible temperature profiles and limited temperature fluctuations. The heating rate of the Nabertherm tube furnace can be simply controlled (the maximum heating rate is about 25 °C/min). Alumina crucibles are used to place the samples in the furnace. The tube furnace was also utilized for post-annealing under H_2/N_2 atmo-

sphere. In this case samples in the alumina crucibles were placed in a silica tube.

3.6.2 Electron beam annealing

After the preparation of $CaAl_2O_4$:Eu, Nd powder, it is necessary to reduce Eu^{3+} to Eu^{2+} in order to obtain persistent emission [48]. For this purpose, we used electron beam annealing in addition to post annealing under H_2/N_2 atmosphere. To facilitate the electron beam annealing, powder pellets of 5 mm diameter were pressed.

The electrons are produced by thermionic emission from a tungsten spiral cathode in a Leybold Univex 450 vacuum system. Then, the electrons are accelerated and the beam (8 keV) is focussed on the material in a spot about 1 mm in diameter by a magnetic deflection unit. The system is equipped with a turbomolecular pump in combination with a rotation pump and the base pressure is around $2x10^{-6}$ mbar. The maximum beam power (3.2 kW) can be directed to the material by controlling the current through the cathode. In order to avoid sublimation of the material, the electron beam intensity is adjusted to heat the material around its melting point.

3.6.3 Spin coating

Spin coating is an interesting and facile technique to obtain homogeneous thin films. The substrate mounted horizontally on a rotating platform spins very rapidly and the coating solution is dispensed onto it. Because of the high speed rotation, most of the solution is thrown off, leaving behind a thin, uniform coating. By changing the rotation speed of the substrate and the duration of the spinning, film thickness can precisely be regulated. The other factors assigning the film thickness are the viscosity of the solution and the evaporation rate of the solvent. Combination of cheap instrumentation, homogeneity of films as well as short coating times makes the spin coating technique one of the most applied methods for sol-gel based thin film production.

In this study, a Headway Research Inc., Model EC101 photo-resist spinner was used to obtain homogeneous TiO_2 and Al_2O_3 thin films and protection layers. By changing the spin speed from 1000 to 6000 rpm and the viscosity of sols, we prepared thin films with different thickness. CaS:Eu particles were coated with TiO_2 and Al_2O_3 for 20 seconds at 500 rpm and 800 rpm, respectively.

3.7 Atomic layer deposition (ALD)

Atomic layer deposition (ALD) is a technique based on the pulsed exposure of a surface to a precursor and a reactive gas. The precursor (elemental vapor or volatile compound of the element) reacts in a self-limiting manner with the surface until a monolayer of molecules is chemisorbed (Fig. 3.6a). The excess of the reactant, which is in the gas phase or physisorbed on the surface, is then pumped out of the chamber with an inert gas pulse before exposing the substrate to the other reactant (Fig. 3.6b). The second gas pulse leads to the removal of the ligands around the metal in the precursor (Fig. 3.6c) and the formation of a compound film (Fig. 3.6d).

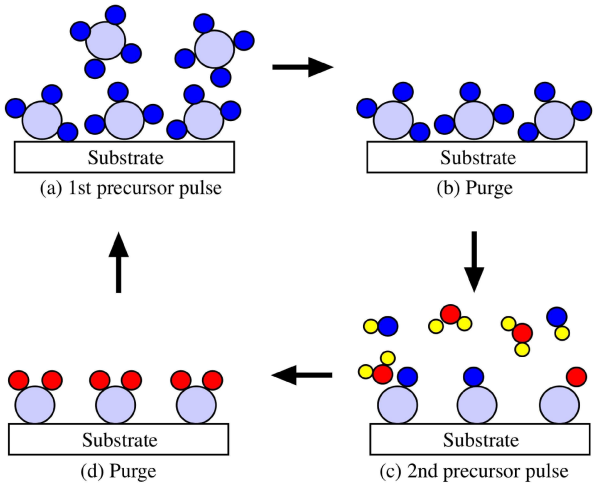

Figure 3.6: Schematic representation of an ALD process [49].

By varying the number of pulses, ALD enables a well controlled deposition of nanometer thin, conformal pinhole-free films on complex substrates with uniformity over large areas. The deposition temperature is low compared to traditional chemical vapor deposition (CVD).

In this work, ALD was used to encapsulate CaS:Eu luminescent particles with conformal Al_2O_3 layers. The deposition of the ALD alumina coating was performed in a home-built system which is shown in figure 3.7 [50]. The reactor was constantly evacuated with a turbomolecular pump and heated to 95°C. The base pressure prior to deposition was about 10^{-4} Pa. Trimethylaluminium (TMA, Sigma Aldrich, 97%) and deionized water were used as aluminium precursor and reactive gas, respectively [51]. The TMA and H_2O

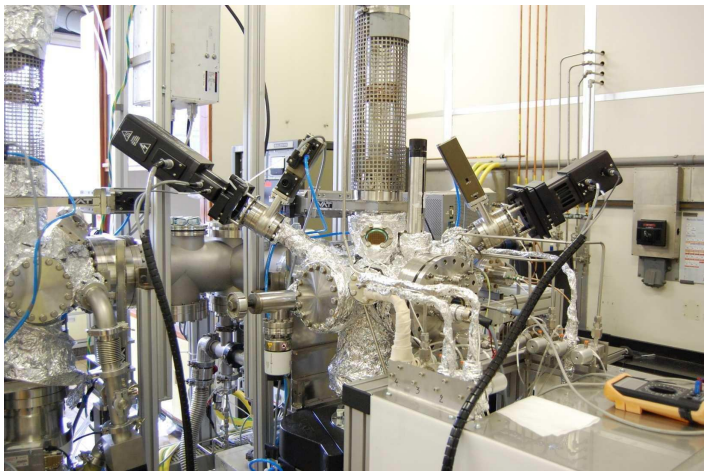

Figure 3.7: Home-built ALD setup in the CoCooN research group.

containers were stored at room temperature and connected to the reactor via heated lines. Using needle valves, the effective pressure of TMA was set to 0.1 Pa and the pressure of H_2O to 0.3 Pa. Gas pulses were delivered by opening computer controlled pneumatic valves. The samples were placed on a resistive heating element, resulting in a deposition temperature of 200°C. One ALD cycle consisted of 2s of TMA, 5s pumping, 5s H_2O vapor and 10s pumping. About 0.1 nm of aluminium oxide was deposited during one cycle. In order to investigate the crystal structure and transparency of the aluminium oxide films, 20 and 100 nm thick aluminium oxide films were deposited on quartz substrates (Heraeus). Aluminium oxide thin films with a thickness of 10 and 20 nm were grown on CaS:Eu. No post-deposition treatments were performed.

Chapter 4

Characterization Techniques and Instruments

In this chapter, the instruments which were utilized to characterize the samples are introduced. Additionally, brief information about the characterization techniques can be found in the present chapter.

4.1 X-ray diffraction

4.1.1 in situ XRD

Crystallization kinetics of the TiO_2 powders were studied in detail via an efficient approach consisting of collecting XRD spectra during the heat treatment, i.e. "in situ" X-ray diffraction (XRD) (Bruker D8-Discovery with Vantec linear Detector and home-made heating stage). The phase transition of the samples was followed during heating from room temperature to 1000°C with a heating rate of 0.1°C/s in a purified helium atmosphere and the diffracted X-rays are collected with a linear CCD detector covering 14 degrees in 2θ.

4.1.2 ex situ XRD

XRD (X-ray Diffraction) measurements were employed to characterize the crystal structure of powders and thin films. A θ-2θ Siemens D5000 diffractometer, equipped with a Cu-Kα X-ray source with a wavelength of 0.15406 nm, and a scintillation detector was used for powder samples. A θ-θ Bruker D8-Discovery diffractometer, equipped with a Cu-Kα X-ray source with a wavelength of 0.15406 nm, and a Lynx eye linear detector was preferred for

thin films characterizations. Figure 4.1 is a schematic representation of a diffractometer. The incident angle θ is always half of the detector angle 2θ.

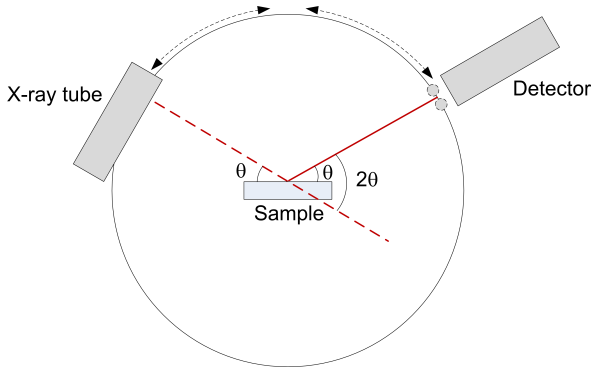

Figure 4.1: Schematic representation of the X-ray diffractometer.

In θ-2θ instruments, when the tube is fixed, the sample and the detector rotate at θ °/min and 2θ °/min, respectively. If we consider a θ-θ configuration, the sample is fixed and the X-ray tube and the detector rotate at a rate -θ °/min and θ °/min, respectively. However, the main difference between the two diffractometers used is the detector. Linear detectors are around one hundred times faster than point detectors (scintillation and solid-state). The speed of these detectors is advantageous for weakly diffracting materials such as thin films.
There are some requirements which need to be fulfilled to take the XRD measurement, as described in paragraphs below.

4.1.2.1 Orientation of the planes

Whether in powders or thin films, only diffraction from diffracting planes parallel to the sample surface can be detected. This condition is easily met in powder samples thanks to crystalline grains with random orientations. When the subject is thin films, certain diffraction peaks can dominate because of the preferential orientation of the grains. However, the XRD pattern of a polycrystalline thin film is often very similar to powder one due to the random orientation of the crystallite grains.

4.1.2.2 Bragg's law

When a crystal is irradiated with X-rays of a fixed wavelength and at certain incident angles, an intense reflection occurs when the wavelengths of

the scattered X-rays interfere constructively. In order for this constructive interference to occur, the differences in the path length must be of the same magnitude as the wavelength of the X-rays. This condition is summarized by Bragg's law and demonstrated in Fig. 4.2.

$$n\lambda = 2d_{hkl}\sin\theta \tag{4.1}$$

and for an orthogonal lattice

$$d_{hkl} = \frac{1}{\sqrt{\left(\frac{h}{a}\right)^2 + \left(\frac{k}{b}\right)^2 + \left(\frac{l}{c}\right)^2}} \tag{4.2}$$

where λ is the wavelength of the incident X-rays, n (a positive integer) is the "order" of reflection, d_{hkl} is the distance between the (hkl) diffracting planes, a, b and c are the lattice parameters, and θ is the scattering angle.

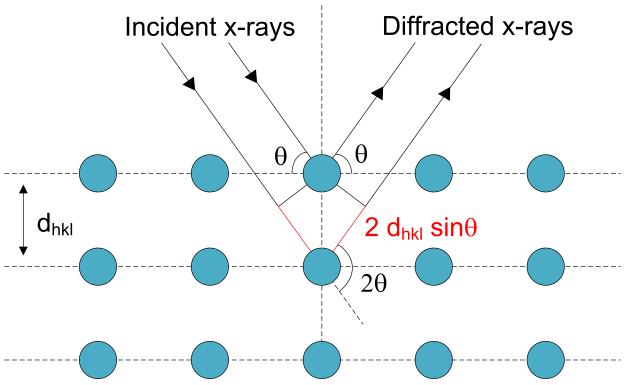

Figure 4.2: Schematic representation of Bragg's law.

4.1.2.3 Intensity of the diffraction peaks

When the Bragg condition is satisfied, the incident X-ray beam is diffracted which appears as a peak in the XRD pattern. Each diffraction can be associated with a set of planes of certain Miller indices. Diffraction from certain planes may not be observed because of the geometrical structure factor F_{hkl}. The shape and content of the unit cell affect the structure factor which is given by

$$F_{hkl} = \sum_{j=1}^{N} f_j e^{2\pi i(hu_j + kv_j + lw_j)} \tag{4.3}$$

Here, f_j represents the scattering power of the atom j in the unit cell and (u_j,v_j,w_j) is the position of this atom. The summation is over the entire unit cell. The square of the structure factor is proportional to the diffraction peak intensity.

$$I \sim |F_{hkl}|^2 \tag{4.4}$$

4.1.2.4 Details of diffraction patterns

After the scan of the crystalline sample, the reflected X-ray intensity is plotted against 2θ to produce an XRD pattern. Combining diffraction peak positions, intensities and widths in the pattern, one can obtain crucial information about the material. For example, an unknown compound can be easily identified using JCPDS (Joint Committee on Powder Diffraction Standards) powder diffraction files. For thousands of compounds, the position, intensity and Miller indices of the diffraction peaks are listed on this file. In addition to that, the crystallite size of the material can be estimated using the width of the diffraction peak by Scherrer's formula.

$$D = \frac{K\lambda}{(B-b)\cos\theta} \tag{4.5}$$

Where D is the average crystallite size, K is the Scherrer constant depending on the shape of the crystallites and the (hkl) values (between 0.7 and 1.7), λ is the wavelength of the X-rays, B is the full-width at half maximum (FWHM) of the diffraction peak, b is the instrumental broadening and θ is the Bragg angle. This equation shows that a small crystallite size leads to broad diffraction peaks.

4.2 Scanning electron microscopy

SEM (Scanning Electron Microscopy) is a surface analyzing technique which is based on electron material interactions. A Scanning Electron Microscope with its high resolution (when bulk objects are examined, instrumental resolution is on the order of 1-5 nm) and its large depth of field is one of the most versatile instruments for the observation and the characterization of heterogeneous organic and inorganic materials [52]. The imaging part of a SEM is formed by the electron column, for which the schematic structure is indicated in Fig. 4.3. The electrons generated and accelerated by an electron gun are focused by electron lenses. The spot size of the electron beam is less than 10 nm. Scan coils sweep the beam across the specimen. When image

magnification is increased, the scan coils are excited less strongly, so that the beam deflects across a smaller area on the specimen. When the electron beam enters the specimen, several signals are produced: secondary electrons (SE), backscattered electrons (BSE), diffracted backscattered electrons which can be that are used to determine crystal structures and orientations, high energy photons (characteristic X-rays that are used for elemental analysis), visible light (cathodoluminescence) and heat as shown in Fig. 4.4. Secondary electrons and backscattered electrons are most often used to produce an image. The intensity signal of secondary electrons and backscattered electrons collected by detectors are amplified for display on the screen. While secondary electrons are used for showing morphology and topography on samples, backscattered electrons are used for illustrating compositional contrast [52].

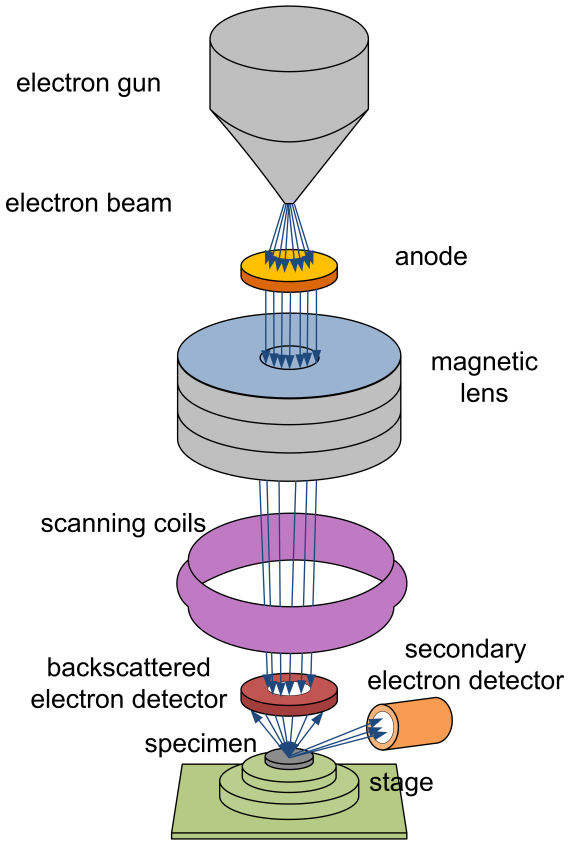

Figure 4.3: Schematic illustration of a SEM setup.

Surface morphology of the specimens was studied using a FEG-SEM (Field Emission Gun Scanning Electron Microscope, FEI Quanta 200F). The FEG

offers a high spatial resolution (< 2.5 nm at 30 kV) and can operate at a wide range of acceleration voltages (between 200 V and 30 kV). It is possible to operate it in high vacuum mode for characterization of conductive materials, low vacuum and environmental SEM (ESEM) modes. The latter allows the imaging and X-ray analysis of wet, nonconductive, unprepared samples, in addition to that the ESEM mode offers a possibility for in situ experiments e.g., in corrosion and oxidation.

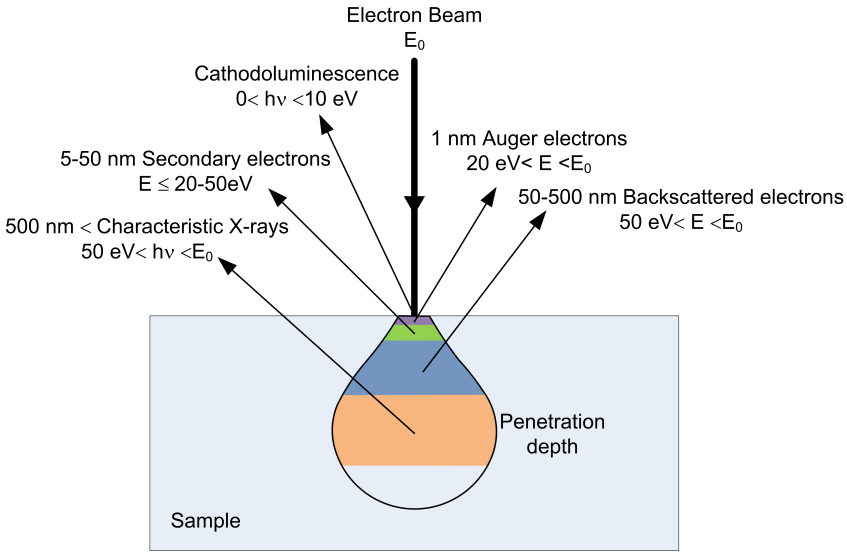

Figure 4.4: Electron interaction volume within a sample.

4.2.1 Energy dispersive analysis of X-rays (EDX)

Electron microscopy does not only offer high resolution imaging, it can also provide elemental analysis via the combination with EDX (Energy Dispersive X-rays spectroscopy). During this research EDX was used to make a quantitative chemical analysis of the samples, by means of a liquid nitrogen cooled Si-Li detector.

When an accelerated electron interacts with the inner shell electron of an atom, it can kick out the electron, leaving a hole (or vacancy). Eventually, this results in the neighbouring outer electron to move into the vacant inner electron shell and in the process emitting an X-ray. The energy of the X-ray is depending on the difference in energy between the energy level that is vacant and the energy level from which an electron falls. Each element produces X-rays which are called "characteristic X-rays" with a unique energy. They

are used to identify the elements present in the sample. Additionally, the concentration of the elements in the sample can be determined in a semi-quantitative way from the intensity of the characteristic X-ray signal. Thus, using SEM in combination with EDX can be used for simultaneous imaging and elemental mapping.

4.3 X-ray photoelectron spectroscopy (XPS)

X-Ray Photoelectron Spectroscopy (XPS) also known as Electron Spectroscopy for Chemical Analysis (ESCA), is an analysis technique used to determine the chemical state and composition of a materials' surface. The maximum information depth is approximately 10 nm. Furthermore, XPS can be utilized for depth profiling by sputtering the sample layer by layer. The sample placed in an ultra-high vacuum environment is irradiated by soft X-rays. The incident X-rays stimulate the ejection of core-level electrons from the atoms of the sample. Although the penetration depth of the X-rays is around 1μm, due to the relatively short mean free path of the electrons, photoelectrons are only emitted from the sample surface. Because an escape of electrons from an insulator surface can cause charging of the sample surface, it is necessary to neutralize this charge effect. A low-energy electron flood-gun is utilized for this purpose. The kinetic energy of a photo-emitted core electron is a function of its binding energy and is characteristic of the element from which it was emitted (equation 4.6).

$$E_K = h\nu - E_B - \Phi \tag{4.6}$$

In this formula, E_K is the kinetic energy of the photoelectron, hν is the energy of the incident X-ray, E_B is the binding energy of the photoelectron, and Φ is the work function of the spectrometer.

When the inner shell electron is ejected by the incident X-ray, an outer electron moves to the core hole. Simultaneously, an Auger electron or a characteristic X-ray is emitted to balance the transition energy. Auger electrons in addition to emitted photoelectrons are used in XPS analysis. An XPS spectrum is obtained by counting the number of photoelectrons as a function of their binding energy. The binding energy corresponding to each peak represents an element present in the sampled volume since the binding energy of a core electron is the finger print of an atom. Moreover the peak area is a measure of the relative amount of the element represented by that peak, the shape and precise position of the peak yield information on the chemical

state for the element.

The chemical composition of the TiO_2 and Al_2O_3 thin films was investigated with XPS. The spectra were acquired on an S-Probe XPS spectrometer from Surface Science Instruments (VG) using monochromatic Al-Kα radiation (1486.6 eV). The angle between the axis of the detector and the sample was 45° and the base pressure of the chamber was $2x10^{-9}$ mbar. The X-ray source was operated at 10 kV, 200 W. Spectra were acquired at 157.7 eV pass energy with a resolution of 0.15 eV. Depth profiles were carried out by Ar^+ sputtering at 4 keV with an argon partial pressure of $1.5x10^{-7}$ mbar and a spot size of 16 mm^2. To avoid artifacts caused by charging of the insulating samples, a charge neutralizer (1 eV) was utilized and the peak positions were calibrated on the C_{1s} peak at 284.6 eV.

4.4 Steady state fluorescence spectrometer

In steady state fluorescence spectroscopy, the material is excited with a continuous light beam and the intensity of the emitted light is recorded. The steady state fluorescence spectrometer at our laboratory is a FS920 (Edinburgh Instruments). It is a sensitive steady state fluorescence spectrometer for accurately collecting photoluminescent excitation and emission spectra in the UV-VIS-NIR spectral range. The spectrometer consists of a xenon arc lamp, two excitation monochromators, a sample chamber, an emission monochromator and a detector (Fig. 4.5).

Xenon arc lamps produce a continuous spectral distribution from 190 to 2600 nm with intense lines between 800 and 1000 nm. The xenon arc lamp is aimed at the entrance slit of the first excitation monochromator. The light from the lamp impinges on the first excitation monochromator in which it is dispersed and the desired excitation wavelength is selected. Low stray light (to about 10^{-8}) and higher spectral resolution (down to 0.05 nm) are achieved by double monochromators. The transmitted beam with a certain bandwidth and spectral resolution passes through the exit slit of the second excitation monochromator and reaches the beam splitter. For monitoring the excitation intensity, a small percentage is diverted to a Si-diode reference detector, while the main part is focussed onto the sample. Emission light from the sample is directed to the emission monochromator by collecting with a lens system. At that point, emission light is filtered to avoid excitation light entering the emission monochromator, which is scanned to determine the wavelength of this emission. The spectral resolution can be controlled by manually adjust-

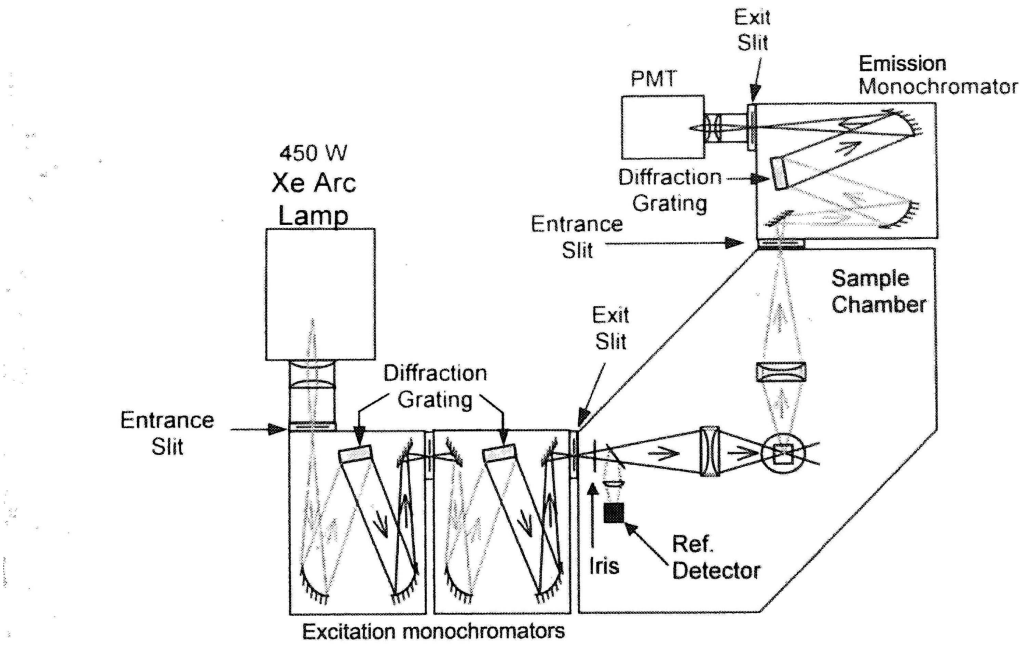

Figure 4.5: Schematic drawing of the Edinburgh Instruments steady state fluorescence spectrometer [53].

ing slit width, using a micrometer screw. The emission light from the sample is detected by a Hamamatsu 928 photomultiplier tube (PMT) in which the signal is amplified (about $1x10^7$) and creates a voltage that is proportional to the emitted intensity. The limit of sensitivity of the PMT is related to the level of dark current which is caused by thermal activation and reduced by cooling the PMT. A Peltier element is used to cool the PMT to about -20°C.

Emission and excitation measurements are done fully automated and controlled by software. When emission spectra are recorded, excitation monochromators are fixed and the diffraction grating in the emission monochromator sweeps. However, during the excitation measurement, the emission monochromator is fixed at a certain wavelength and the excitation wavelength is changed in a specific range. Dwell time of each position has an effect on the emission intensity and signal-noise ratio of the spectrum and it can be varied from 0.1 to 5 s. It is very import to have emission or excitation spectra which are free from any instrumental effect; therefore, spectral correction is done for the entire emission and excitation range by software using standard correction files.

4.4.1 In situ steady state fluorescence spectrometer

The chemical stability of the phosphor layers was inspected with an in situ photoluminescence measurement during accelerated aging of the uncoated and coated samples at 80°C and 80% relative humidity. The measurements were executed in a Clima Temperature Systeme (CST), CS-40/200 humidity chamber in the Centre for Microsystems Technology (CMST) laboratory. The experimental setup is indicated in Fig. 4.6. PL intensities of the sample in the humidity chamber were measured with an HR2000+ luminescence spectrometer (Ocean Optics). This spectrometer provides a resolution of 0.75 nm (FWHM) and also it can capture and store a full spectrum into memory almost every millisecond when the spectrometer is interfaced to a computer via USB. Samples were excited by a LED with an emission wavelength of 440 nm. Using a Bif400-UV/VIS Y-shaped optical fiber cable (Ocean Optics) with a 400μm core diameter excitation light from the LED to the sample and emission light from the sample to the spectrometer were separated. The spectra were recorded every 10 minutes during at least 15 hours.

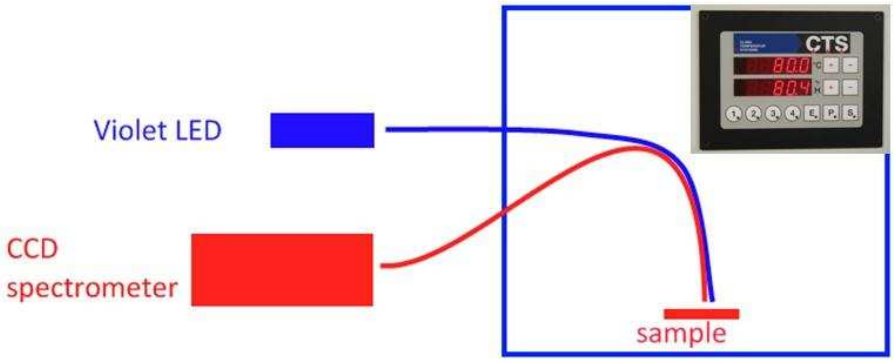

Figure 4.6: Experimental setup for the aging test.

4.4.1.1 Optical transmission measurements

Transparency measurements of the films were executed by means of a Cary 500 UV-Vis-NIR spectrophotometer. Using this instrument is it possible to obtain very accurate transmission spectra between 175 and 3000 nm in a short time. The spectrometer consists of two light sources; namely, tungsten halogen from visible to near-IR and a deuterium arc lamp for UV, and two detectors; namely, a high performance R928 photomultiplier tube as UV-Vis detector and an electrothermally controlled lead sulfide photocell as near-IR

detector. Corning 1737 sodium-free borosilicate glasses and quartz were used as substrate.

4.5 Spectroscopic ellipsometry

Spectroscopic Ellipsometry (SE) is a very sensitive optical technique devoted to the analysis of surfaces. The measurement is based on the change in polarization caused upon specular reflection from a surface. Linearly polarized incident light with parallel (p) and perpendicular (s) electric field components is generally elliptically polarized after reflection (fig 4.8).

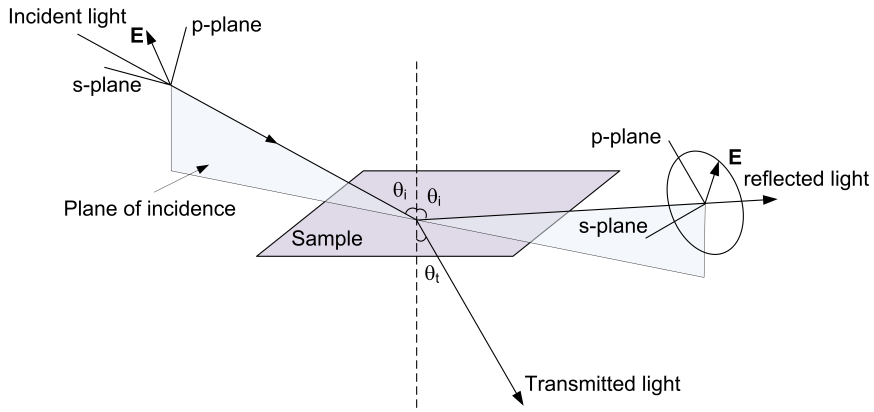

Figure 4.7: Reflection and transmission of the light.

The reflected light has undergone amplitude and phase changes for both p- and s-components of the incident beam. Ellipsometry measures the changes of these components, commonly written as:

$$\rho = \frac{r_p}{r_s} = \tan(\Psi)e^{i\Delta} \tag{4.7}$$

In this formula, Ψ and Δ indicate the amplitude ratio and phase shift, respectively. r_p and r_s are the reflection coefficients of p- and s-components of the electric field and they are directly related to optical constants of the material by assuming the ambient is air (Fresnel equation):

$$r_p = \frac{n\cos\theta_i - \cos\theta_t}{n\cos\theta_i + \cos\theta_t} \text{ and } r_s = \frac{\cos\theta_i - n\cos\theta_t}{\cos\theta_i + n\cos\theta_t} \tag{4.8}$$

where n is the refractive index of the material.

In order to acquire information about the film thickness and optical constants, it is necessary to construct an appropriate optical model. Ellipsometric parameters Ψ_{model} and Δ_{model} are calculated using parameters in the model. Then the calculated Ψ_{model} and Δ_{model} are used to compare the calculated data to experimental (measured) data. Fitting quality is determined by a comparison between model-generated curves and experimental data. The mean squared error (MSE) quantifies the difference between model and experimental curves. Although a small MSE is necessary, it is not sufficient to decide the proposed model is correct. To determine the best model in addition to knowledge about the sample, physical laws should be considered. Otherwise a fitting with a small MSE without physical significance can be easily obtained.

Optical constants and thickness of TiO_2 and alumina thin films were determined via SE, J.A. Woollam Co. Inc., M-2000FI at an angle of incidence of 65°. Fitting was performed over the region of 250- 1700 nm, using the Complete Ease software (Woollam Inc.). The refractive index of the thin films was calculated at 632.8 nm. Porous thin films have different optical properties than the bulk of the same material. To estimate the average effective optical and/or electrical parameters of porous thin films, Bruggeman's or Maxwell Garnett's equation can be used. The effective refractive indices of the films were calculated using the Bruggeman effective medium equation [54]. The Bruggeman effective medium equation for two-component systems is given by

$$f\frac{n_1^2 - n_{eff}^2}{n_1^2 + 2n_{eff}^2} + (1-f)\frac{n_2^2 - n_{eff}^2}{n_2^2 + 2n_{eff}^2} = 0 \tag{4.9}$$

where n_{eff} is the effective refractive index of the thin film. The refractive index of the first and second component is represented by n_1 and n_2. The volume fraction of the first component is indicated by f.

4.6 Thermal analysis

Thermogravimetric analysis (TGA) measures the changes in substance weight as a function of temperature or time in a controlled atmosphere. The TGA technique is very useful to analyze materials that exhibit either mass loss or gain due to decomposition, oxidation or loss of volatiles. Differential thermal analysis (DTA) measures the temperature difference between the substance and an inert reference as the heat flow to the substance and reference remains the same. This differential temperature (ΔT) is then plotted against

temperature. Two kind of peaks can be observed in a DTA curve, namely endothermic and exothermic peaks. The endothermic peaks where ΔT is negative may represent melting, vaporisation, sublimation and desorption. The exothermic peaks where ΔT is positive may indicate crystallisation, adsorption, polymerisation and catalytic reactions. Simultaneous TGA-DTA measures both heat flow and weight changes in a material as a function of temperature. This simultaneous measurement allows to determine melting, crystallization and degradation steps of the materials [55, 56].

TGA and DTA of the sols were carried out using a SDT 2960-TA instrument in the Department of Inorganic and Physical Chemistry. The measurements were done at a heating rate of 10°C/min beginning from room temperature in a flowing air environment.

4.7 Fourier transform infrared spectroscopy

Infrared (IR) spectroscopy is based on the fact that molecules absorb specific frequencies that are characteristic of their structure. Fourier transform infrared (FT-IR) spectroscopy uses a measurement technique in which an interference pattern is converted to an IR spectrum [57, 58]. The IR beam from the source enters the interferometer where the beam is split towards the moveable mirror and the fixed mirror. If there is no sample between interferometer and detector, the two reflected beams recombine and interference of them is measured by the detector. The signal is called an interferogram which is a kind of spectral encoding consisting of information about every infrared frequency which comes from the source. If a sample is present, an absorption occurs, thereby modifying the interferogram. The final infrared spectrum is formed from the interferogram by Fourier transformation. The resulting spectrum is the intensity of IR light as a function of the frequency. It consists of specific regions related to different kinds of bonds and vibration of these bonds (stretching or bending). Using a reference table in which the absorption frequencies for different types of bonds are listed, an unknown material can be identified [58]

In this work, the spectra were recorded from 400 to 4000 cm^{-1} with a Bruker IFS66V spectrometer. The resolution was 3 cm^{-1}, and 600 scans were used for every sample. The background spectra were recorded using an uncoated double side polished Si substrate.

Chapter 5

Literature data

5.1 White-light emitting diodes (LEDs)

White-light emitting diodes (LEDs) challenge traditional incandescent, fluorescent and halogen lamps for general lighting. They have several advantages such as long life time (longer than 30000 hours), low power consumption, small size and short light up time. Additionally, LEDs do not contain toxic chemicals like mercury [59]. There are two primary ways to produce white light from LEDs. The first one is the multi-colored method in which white light is produced by mixing different colors from three different LEDs [60,61].

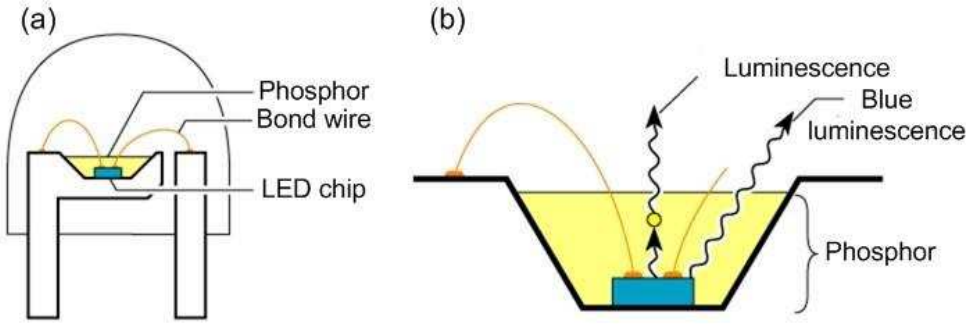

Figure 5.1: (a) Structure of a white LED consisting of a GaInN blue LED chip and a phosphor encapsulating the chip. (b) Detailed view [62].

The second and also the more popular one is the phosphor-converted method. In this method, a blue emitting semiconductor diode based on gallium nitride (GaN) or indium gallium nitride (InGaN) is covered with a phosphor layer commonly Ce^{3+} doped $(Y,Gd)_3Al_5O_{12}$ (YAG:Ce) [27, 60, 61]. A schematic

representation of the phosphor-converted white LED is shown in Fig. 5.1. The emission spectrum, which is a combination of blue light from the LED chip and yellow light from the phosphor, is shown in Fig. 5.3. Using this YAG:Ce based approach, only cold white light can be obtained. As seen in the spectrum, the emission from YAG:Ce lacks a significant contribution in the red part of the spectrum. Therefore, using this material warm-white light sources cannot be obtained, and also the color rendering index is low.

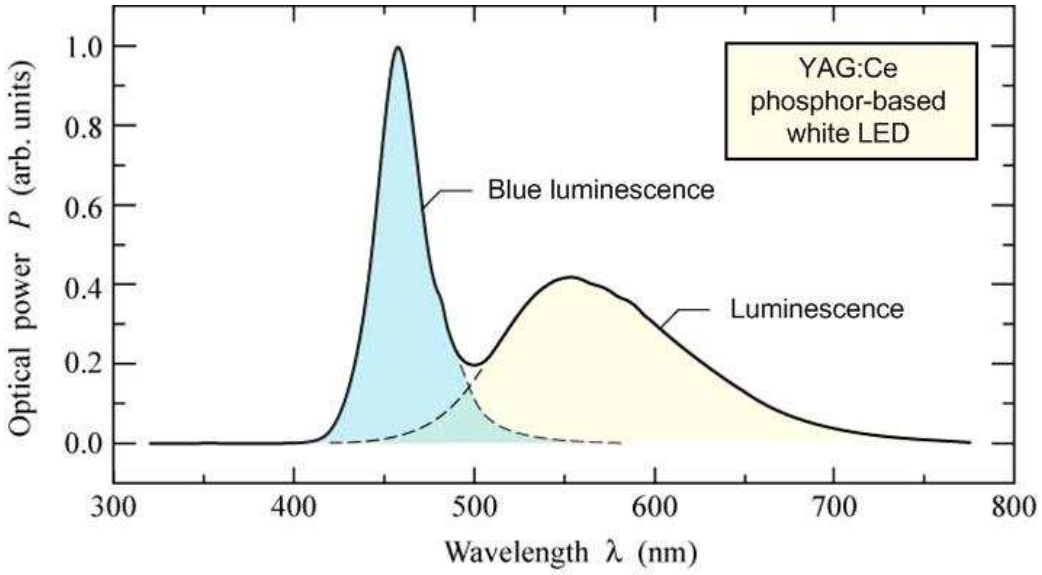

Figure 5.2: Emission spectrum of a phosphor-based white LED manufactured by Nichia Corporation (Anan, Tokushima, Japan) [62].

The poor color rendering problem can be overcome by trichromatic white LEDs comprising two phosphors, the first emitting between 520 and 570nm (green) and the second emitting between 590 and 660 nm (red) [11, 17, 27]. CaS:Eu^{2+} with an intense red emission can be used as red phosphor for phosphor-converted white LEDs [11, 17, 60]. CaS:Eu^{2+} is also an interesting electroluminescent material, as it can be used in flat panel displays as red phosphor [63, 64].

5.2 CaS:Eu^{2+}

5.2.1 Luminescence of CaS

Although the emission of CaS:Eu^{2+} is much stronger, undoped CaS can also show luminescence. Pandey and Sivaraman [65] reviewed the luminescence properties of calcium sulfides prepared with different methods (table 5.1). They compared CaS single crystals prepared with floating hot zone and iodine transport techniques. They reported that the emission spectrum of undoped CaS exhibits a strong dependency on the preparation method. This is quite evident, since this emission is related to defects in the CaS.

Crystal type	Synthesis method	Emission wavelengths (nm)
Single crystal	floating hot zone	352
Single crystal	iodine transport	352 <u>425</u>
Polycrystalline	reduction of sulfates	<u>360</u> 485 530

Table 5.1: Maxima of the emission peaks of undoped CaS prepared by different techniques [65]. Dominant emission peaks are underlined.

The single crystal CaS prepared by floating hot zone method has only one emission peak at 352 nm, while the CaS prepared by the iodine transport method has two emission peaks at 352 nm and 425 nm, with the latter being stronger. At room temperature, the polycrystalline CaS has three peaks which are located at 360, 485 and 530 nm. The last two emission peaks are very weak. The peaks accompanying the main emission peak around 360 nm were assigned to presence of trace levels of oxygen [12, 65]. Brightwell et al. [12] observed that at 77 K, the emission wavelength of the polycrystalline CaS shifts from 360 to 380 nm and no extra peak is present in the spectrum. Moreover, the emission intensity at 77 K is twice as high as at room temperature [12]. The excitation spectra of CaS at 360 and 380 nm consist of one peak with a maximum at 240 nm [12]. This excitation peak corresponds to band gap transition in CaS (band gap energy of CaS is around 4.88 eV [66]). It is interesting to know these defect emissions to distinguish and identify the luminescence characteristics of doped CaS.

5.2.2 Luminescence of CaS:Eu^{2+}

There are several reports in literature regarding the luminescence properties of CaS:Eu^{2+} prepared with different techniques such as solid state re-

action, wet chemical synthesis, solvothermal synthesis and microwave heating [33, 63, 67, 68]. It has an emission at 652 nm with a FWHM (Γ) of 1460 cm^{-1} (68 nm) [25, 69]. The red shift (D) is the energy difference between the lowest $4f^6 5d$ excited state of Eu^{2+} when incorporated in CaS and when Eu^{2+} is in the free (gaseous) state. It is a combination of the crystal field splitting and the centroid shift. The red shift for CaS:Eu^{2+} is 17766 cm^{-1}. The Stokes' shift (ΔS) is 1329 cm^{-1} [25].

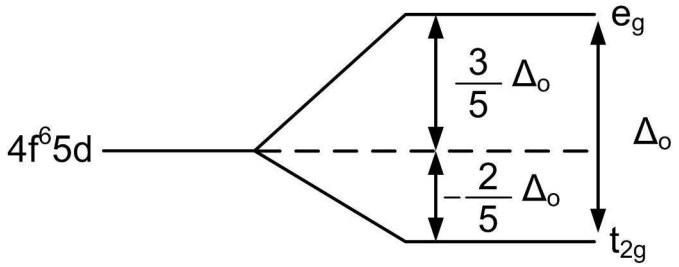

Figure 5.3: Crystal field splitting diagram of 5d orbital in an octahedral symmetry.

In the case of octahedral symmetry the 5d orbital of Eu^{2+} is split into e_g and t_{2g} levels by the crystal field and the crystal field splitting parameter (Δ_o) is approximately 15000 cm^{-1}. Detailed explanation of the crystal field splitting can be found in § 2.1.8.2. The excitation spectrum consists of two bands which are located at the high energy side (250-400 nm) and low energy side (400-600 nm) [32, 70, 71]. While the direct excitation from the $4f^7(^8S_{7/2})$ ground state to the $4f^6 5d$ (t_{2g}) excited state is responsible for the low energy side excitation band, the high energy side excitation band is due to the combination of the CaS bandgap transition and the excitation to the $4f^6 5d$ (e_g) state in Eu^{2+} [32, 70, 71].

5.2.3 Degradation of CaS

CaS:$Eu^{2+}$is a promising material for phosphor-converted white LEDs and flat panel displays as red phosphor [63,64]. Nevertheless, the lack of stability with respect to water, oxygen and carbon dioxide in air hinders usage of CaS as phosphor host [8, 11–15, 17, 18]. As an example, during the operation of high power LEDs, the chips can reach relatively high temperatures of 450 K. Degradation of the alkaline earth sulfides is accelerated by temperature and decomposition products such as sulfur dioxide and hydrogen sulfide gases evolve from the surface. Therefore, the decomposition causes not only a de-

crease in the light intensity, but also a reduction in the reflectivity of silver inside the LED due to the chemical reaction between the released hydrogen sulfide gas and the silver pad under the LED chip [11].

Suzuki et al. [72] investigated the degradation of CaS at room temperature in different conditions such as under N_2 and in air, water or KOH solutions (with different concentrations). They observed that

- Presence of O_2 enhances the hydrolysis of CaS. Moreover, contact with atmospheric CO_2 results in $CaCO_3$ formation and it also accelerates the hydrolysis of CaS.
- The fastest hydrolysis occurs when they used water as a solvent.
- Lower and higher pH values increase the hydrolysis. The slowest hydrolysis takes place when pH is around 11.

García-Calzada and colleagues [73] studied the decomposition of CaS at room temperature in air saturated with water. They reported that sulfur as H_2S gas is released during the first 48 hours, then there is no change in sulfur concentration. They concluded that calcium carbonate ($CaCO_3$) and sulfur-oxygen salts of calcium (such as $CaSO_3$, $CaSO_4$) are formed due to decomposition of CaS and they create an impervious layer on the CaS particles. This layer shows a high resistance to pass gases and water. Therefore, they impede the further degradation.

In addition to atmospheric conditions, particle size is another factor which influences the degradation process. Madarász et al. reported [13] that, as expected, in the same conditions small particles degrade faster than bigger ones. In the same study [13] they compared the oxidation ratio of SrS with CaS and concluded that SrS oxidizes slower than CaS.

5.2.4 Luminescence of $CaSO_4$:Eu

Formation of $CaSO_4$ due to degradation of CaS can be determined by different techniques such as XRD, potentiometry and SEM-EDX [72–74]. In addition to these techniques, PL measurements can be utilized to determine the formation of $CaSO_4$ due to the decomposition of Eu doped CaS.

$CaSO_4$:Eu can accommodate both divalent and trivalent Eu ions [75–78]. The emission and excitation wavelengths of $CaSO_4$:Eu are indicated in Fig.

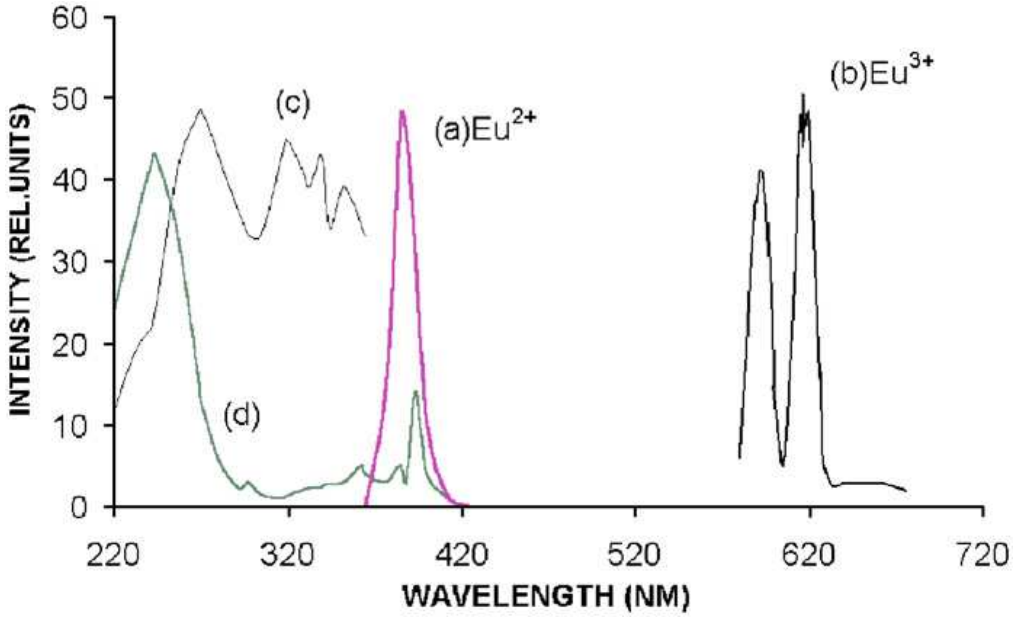

Figure 5.4: Typical photoluminescence of Eu^{2+} and Eu^{3+} in $CaSO_4$: (a) Eu^{2+} emission (for 320 nm excitation), (b) Eu^{3+} emission (for 245 nm excitation), (c) Eu^{2+} excitation (for 385 nm emission), (d) Eu^{3+} excitation (for 615 nm emission) [75].

5.4 [75]. The emission peak located at 385nm is associated with the $^5P_{7/2}$-$^8S_{7/2}$ transition of Eu^{2+} [77] and the excitation peaks at 270, 320, 335 and 350 nm are due to the f-d transitions of Eu^{2+} [78]. The emission peaks at 593, 618, 695 and 702 nm indicate the f-f transition for Eu^{3+} ion [77, 78]. While the excitation peak at 255 nm is correlated with the charge transfer band of Eu^{3+}, the excitation peaks at 315, 385 and 395 nm are related to the f-f transitions of Eu^{3+} [78].

5.2.5 Stability improvement of CaS:Eu^{2+}

In order to overcome the stability problem of CaS, a number of studies were reported. Brightwell et al. tried to improve the stability of CaS by producing highly crystalline samples using two different ways. In 1982, they used vapour phase transport with a halogen carrier [79] and in 1988, they utilized H_2S flow [12]. However, the use of H_2S gas is not recommended due to its toxicity. The most common way to improve the stability of sulfides is covering the phosphor surface with a coating layer. Plenty of encapsulation techniques have been utilized to enhance the stability of sulfide phosphors [11, 14–18, 80–83]. Organic materials [84], nitrides [83] and oxides [11, 14–18, 82, 83]

have been used as protection coating for sulfide phosphors. The properties of the protection coating are as important as the coating technique. In order to improve the stability of sulfides by encapsulation with an inert film, the film should be thermally and chemically stable. Organic coatings can not resist high temperature thus they are not favorable for coating application. In addition, the encapsulation should be transparent to the excitation and emission light of the incorporated luminescent particles. The film should also homogeneously coat the particle surfaces. Nishio et al. [80] coated ZnS:Cu with a double layer using chemical vapor deposition (CVD). The first layer is a metal oxide film as heat resistive coating and the second layer is a silicon nitride film for moisture resistance. They claimed that even coating with only the first layer improves the stability of the phosphor but the second layer is necessary for better stability. They compared the times for which the brightness of uncoated and coated phosphors falls to half its initial value at 50°C and 90% relative humidity (RH); it is only 10 hours for the uncoated phosphor while it is 100 and 400 hours for phosphor coated with only the first layer and double coated phosphor, respectively. Fan et al. [81] used atomic layer deposition (ALD) to coat the ZnS:Cu surface with AlOOH and they compared it to CVD. They have shown that after 100 hours at 50°C and 90% RH, the phosphor coated with ALD retains 70% of its initial brightness, while the one coated with CVD has 57% left of the initial brightness (the brightness of the uncoated sample is not measurable anymore after 100 hours ageing). The results are impressive, however these techniques need special equipment and expensive instruments, therefore sol-gel is the an interesting option to explore.

$Ca_{0.8}Sr_{0.2}S:Eu^{2+},Tm^{3+}$	Initial PL intensity (%)	PL intensity after 20 days (%)
uncoated	100	18
coated with $2wt.\%$ Al_2O_3	88	83
coated with $5wt.\%$ ZnO	83	74
coated with $2wt.\%$ SiO_2	94	84
coated with $5wt.\%$ TiO_2	98	82

Table 5.2: Luminescent intensities of uncoated and coated $Ca_{0.8}Sr_{0.2}S:Eu^{2+},Tm^{3+}$ before and after 20 days treatment at room temperature and 90% RH [14, 15].

A wet chemical technique was used by Guo et al., to coat $Ca_{0.8}Sr_{0.2}S:Eu^{2+},Tm^{3+}$ particles with a particle size of 40 μm by ZnO, Al_2O_3, TiO_2 and SiO_2 [14,15].

In this technique, they have dispersed the $Ca_{0.8}Sr_{0.2}S:Eu^{2+},Tm^{3+}$ particles in aqueous solution of ZnO, Al_2O_3, TiO_2 and SiO_2 precursors. They examined the degradation of the uncoated and coated particles at room temperature and at 90% RH. Their observations are listed in table 5.2. They reported that coating with oxides using wet chemical techniques causes the loss of some luminescence intensity due to irregular reflection of emission light by the coated particles. Nevertheless, it is still worth coating; they observed that after 20 days, the uncoated phosphor has only 18% of the initial intensity. However, coated with Al_2O_3, ZnO, SiO_2 and TiO_2 they retain 83%, 74%, 84% and 82% of the initial intensity, respectively.

5.3 Optical and structural properties of TiO_2

Among the inorganic oxides, TiO_2 is a well known material due to its broad application area. In order to prepare TiO_2 fine powders and films, a wide range of techniques has been used such as hydrothermal methods [85,86], electron beam evaporation [87, 88], DC and RF magnetron sputtering [44, 89], solvothermal synthesis [90, 91] and sol-gel methods [44, 92–95]. Among these techniques the sol-gel method offers several advantages: fine powders and films with high homogeneity can be prepared using simple equipment, the thickness and the porosity of the films can be easily controlled by changing the concentration of the sol and large surface areas can be coated by spin or dip coating.

When precursors with strong reactivity towards water (like titanium alkoxides) are used, the hydrolysis reaction can result in precipitation [35]. The problem can be overcome using nonaqueous sol-gel techniques with titanium chloride [92, 96, 97] or titanium alkoxides [44–46] as precursor. In case of the reactions using $TiCl_4$ as a precursor, TiO_2 forms under release of a large amount of HCl gas. Because HCl gas is toxic and chlorine impurities often remain in the final oxide material [98], titanium alkoxides like titanium n-butoxide and titanium isopropoxide as precursor may be preferred. In order to increase the stability of the solutions from titanium alkoxide precursors, it is not sufficient to switch to a non-aqueous sol-gel route. Indeed, a chelating agent is still needed in a non-aqueous sol-gel route to obtain highly stable sols [44–46, 90, 95].

Crystalline TiO_2 has three polymorphs which are brookite, anatase and rutile. Although anatase and rutile have the same crystal structure (tetragonal, D_{4h}), their lattice parameters are different ($c/a>1$ for anatase, $c/a<1$ for ru-

tile). Brookite has an orthorhombic structure with space group D_{2h}. Brookite is rarely found in nature and to synthesize brookite thin films certain conditions are required [99]. Therefore there is a lack of information on optical properties of brookite thin films. Band gap (E_g) values and refractive indices of anatase and rutile titanium dioxides are listed in table 5.3. In the table, n_e represents the refractive index for light perpendicular to the optical axis of the crystal and n_o is the refractive index for light parallel to the optical axis of the crystal. Note that refractive indices can strongly depend on the preparation technique of the material, e.g. in the case of high porosity.

Structure	Band gap E_g (eV)	n_o	n_e
Anatase	3.20	2.49	2.56
Rutile	3.03	2.61	2.91

Table 5.3: Band gap of bulk anatase and rutile TiO_2 [100–103]. The refractive indices (n_o and n_e) are at 589 nm.

Hu et al. [94] investigated the effect of solvents used in the preparation on properties of TiO_2 thin films. They reported that adding isopropanol as co-solvent into ethanol and titanium isopropoxide solution reduces the refractive index. An increase in the annealing temperature results in a decrease in refractive index. Film thickness and optical constants of a number of thin films were determined using spectroscopic ellipsometry. The Cauchy dispersion model has been used to calculate the refractive index of TiO_2, films by Wang [104] and Jiang [90]. Eiamchai et al. [105] and Horprathum et al. [106] used the Cody-Lorentz dispersion model to calculate band gap energy and refractive index of TiO_2 films and they claimed that the Cody-Lorentz dispersion model offers more realistic results than the Cauchy dispersion model. Using the Cauchy dispersion model, the refractive index close to the band gap cannot accurately be determined [105, 106] but it results in good fitting in the transparent region of the material [107].

5.4 Optical and structural properties of Al_2O_3

Al_2O_3 has several metastable polymorphs (so called transition aluminas) such as γ , δ, θ, η but the best known one is the thermodynamically stable α-Al_2O_3 (corundum form) [108, 109]. α-Al_2O_3 is one of the most widely used ceramics [110]. Amorphous Al_2O_3 is as attractive as crystalline Al_2O_3. It is frequently used as protective coating [15, 111–113] and it can be used as

water repelling coating [114].

To synthesize aluminium oxide films several techniques have been used such as E-beam evaporation, laser deposition, reactive magnetron sputtering, RF magnetron sputtering, atomic layer deposition and sol-gel [115–117]. Depending on the preparation technique, the optical properties and thickness of the films can change easily. The refractive index which is typically in the range of 1.4-1.72 is lower than that of bulk α-Al_2O_3 (1.76) because of the higher density of bulk α-Al_2O_3. Al_2O_3 has a broad transparency window from UV to IR [118, 119] thus it can be used as optical coating [15, 112].

Besides the techniques listed above, non-aqueous sol-gel synthesis has been also used to prepare Al_2O_3 but there is a very limited number of publications about this subject. The non-aqueous sol-gel method is commonly used to prepare Er^{3+} doped Al_2O_3 powder [5, 47, 120–122]. Dong et al. [5, 120, 121], Zhu et. al [122] and Yang et al. [47] used aluminium isopropoxide ($(Al(OC_3H_7)_3)$) as precursor and isopropanol (^{i}PrOH) as solvent. Different from these preparation techniques, Acosta et al. synthesized alumina gels using aluminum isopropoxide ($(Al(OC_3H_7)_3)$) and aluminum chloride ($AlCl_3$) as starting materials [123]. Additionally, Zhou and colleagues [124] synthesized γ-Al_2O_3 nanocrystals using aluminum acetylacetonate as precursor and benzylamine as the solvent.

5.5 $CaAl_2O_4$

Monocalcium aluminate, $CaAl_2O_4$ (CA) is a system which consists of CaO (C) and Al_2O_3 (A). It is frequently used as cement in very different areas from construction to dental applications [125–127]. It can also be used as optical and structural ceramic [125–127]. Some amorphous calcium aluminate compositions show photosensitivity, therefore they are potential candidates for optical information devices [127]. Vijaya et al. suggest Sr added $CaAl_2O_4$ for the detection of volatile organic compounds [128]. In addition to these application areas, rare earth doped $CaAl_2O_4$ is a well known luminescent material [19, 48, 129–131].

Calcium aluminate has different phases such as C_3A ($Ca_3Al_2O_6$), CA ($CaAl_2O_4$), C_5A_3 ($Ca_5Al_6O_{14}$),and $C_{12}A_7$ ($Ca_{12}Al_{14}O_{33}$). When $CaAl_2O_4$ is prepared by conventional methods, one of the main problems is the formation of multiphase systems. Besides calcium aluminates in different phases it is possible to have CaO and some aluminium oxide compounds in monocalcium alumi-

nate [125, 127, 128, 131–133]. Presence of extra phases in $CaAl_2O_4$ depends on heat treatment conditions, the mole ratio of Ca and Al and presence of extra chemicals such as boric acid (H_3BO_3) [131, 134]. The phase diagram of calcium aluminates prepared using solid-state reaction between $CaCO_3$ (CaO) and Al_2O_3 and is given in Fig. 5.5 [131]. This figure summarizes the temperature and composition dependency of phases.

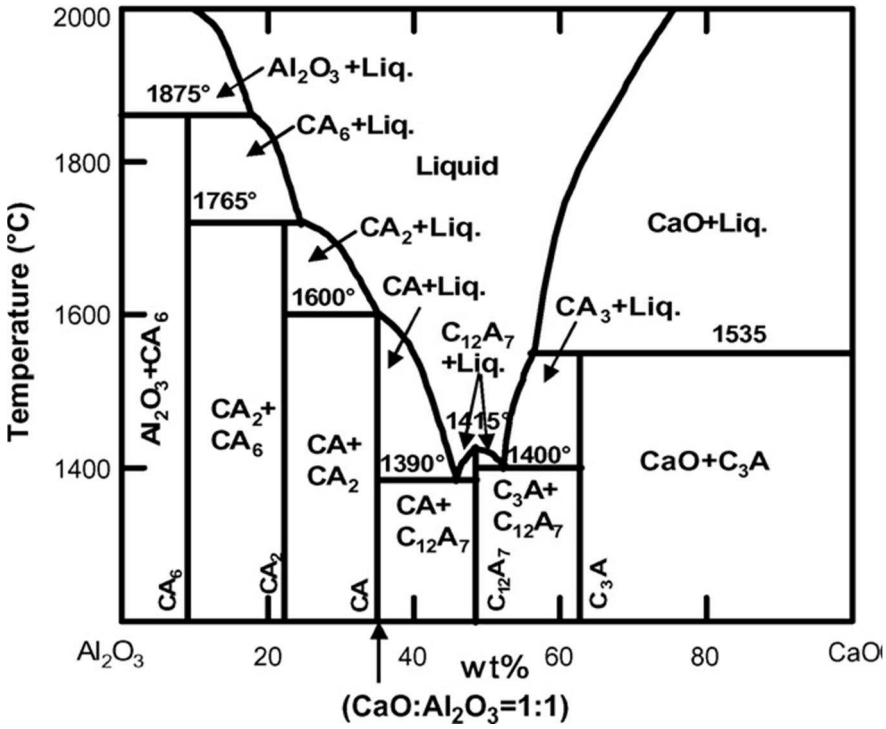

Figure 5.5: Phase diagram of CaO-Al_2O_3 systems [131].

Figure 5.5 indicates that monocalcium aluminate can be obtained up to 1600°C. Monocalcium aluminates in two different crystal structures can also be synthesized by the sol-gel method, they are hexagonal and monoclinic [130, 135, 136]. The hexagonal one is formed at relatively lower temperatures than the monoclinic one. Aitasalo et al. [130] and Janáková [137] obtained metastable hexagonal $CaAl_2O_4$ with space group $P6_3$ (Z=6) and lattice parameter a=8.74 Å and c=8.08 Å at 850°C using the sol-gel method and they also reported that the transition from hexagonal to monoclinic phase occurs around 1050°C, although it depends on the duration of the heat treatment. However, using a spray-drying and calcination process at 930°C orthorhombic $CaAl_2O_4$ with lattice parameters a=8.744 Å, b=8.093 Å, and c=15.148 Å was prepared by Douy and Gervais [133]. They also reported that at 1500°C

pure monoclinic $CaAl_2O_4$ was obtained [133].

The reported minimum temperature to synthesize monoclinic $CaAl_2O_4$ is 1250°C [135]. In literature, it is possible to find two monoclinic $CaAl_2O_4$ structures with different lattice parameters but crystallized in the same space group. The first one was reported in 1976 by Hörkner and Müller-Buschbaum [138]. They claimed that monoclinic $CaAl_2O_4$ has a stuffed tridymite type structure with $P12_1/n1$ as the space group (a=8.700 Å, b=8.092 Å, c=15.191 Å, and β=90.17°) [138]. In this monoclinic $CaAl_2O_4$, there are three different Ca sites. Two of them are six coordinated sites with octahedral symmetry where the Ca-O average distances is 2.4 Å and the other one is a nine coordinated site with trigonal anti-prism symmetry, which has longer Ca-O distances (average 2.8 Å) [135, 139]. The second one was published by Ito et al. They reported that $CaAl_2O_4$ has high pressure monoclinic phase with space group of $P12_1/c1$ (a=7.950 Å, b=8.620 Å, c=10.250 Å and β=93.10°). In this monoclinic $CaAl_2O_4$, there are two different sites for the Ca cation, each with 9-fold coordination [140].

5.6 Luminescence of doped $CaAl_2O_4$

$CaAl_2O_4$ was doped with Mn by Singh et al. [141]. They observed two broad peaks at 540 and 710 nm under laser excitation at 488 nm. Wang et al. [142] prepared $CaAl_2O_4$:Ce^{3+} and $CaAl_2O_4$:Mn^{2+}, Ce^{3+} using solid state reaction and investigated the luminescence properties of this material. Under excitation at 362 nm the single doped system shows an emission with a maximum at 412 nm while the double doped system has an emission with a maximum at 522 nm [142]. They also observed persistent luminescent emission at 525 nm during over 10 h for $CaAl_2O_4$:Mn^{2+}, Ce^{3+} [142]. Nevertheless, the most popular doping element for $CaAl_2O_4$ is europium in the case of persistent luminescence. Europium can be trivalent (Eu^{3+}), divalent (Eu^{2+}), or both of them together in $CaAl_2O_4$. Janáková and et al. [137] prepared Eu^{3+} doped hexagonal and monoclinic $CaAl_2O_4$.
They observed $^5D_0 \rightarrow {}^7F_1$ and $^5D_0 \rightarrow {}^7F_2$ transitions in the emission spectra of both Eu^{3+} doped $CaAl_2O_4$ phases. This reveals that Eu^{3+} occupies at least two different sites in both structures (this has already been explained in section 2.1.8.1) [137]. However, there is a main difference in the emission spectra between monoclinic and hexagonal phases. The strongest emission peak is located at around 616 nm for the monoclinic phase while it is at around 611 nm for the hexagonal one (Fig. 5.6). The excitation spectrum of the Eu^{3+} doped monoclinic phase is also slightly different from that of

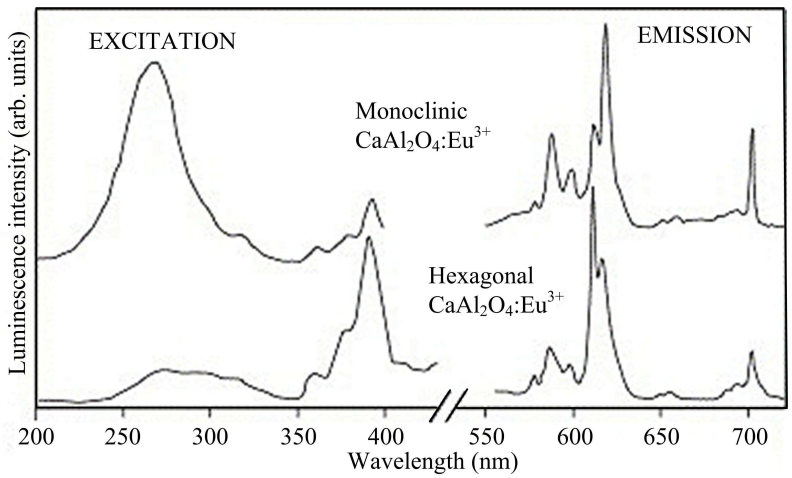

Figure 5.6: Steady-state photoluminescence spectra of monoclinic and hexagonal $CaAl_2O_4$: Eu^{3+} at room temperature. Emission was recorded at λ_{exc}=300 nm and excitation at λ_{em}=613 nm [137].

the hexagonal one, the spectrum of the hexagonal phase is dominated by the intraconfigurational $^7F_0 \rightarrow {}^5L_6$ transition peaking at around 395 nm, while the spectrum of the monoclinic phase is dominated by a strong UV band peaking at around 260 nm which is ascribed to $O^{2-} \rightarrow Eu^{3+}$ charge transfer [137](Fig. 5.6).

Different techniques have been used to prepare Eu^{2+} doped $CaAl_2O_4$ such as solid state reaction, co-precipitation, microwave, Pechini, combustion, spray-drying, laser-heated pedestal growth, floating zone and sol-gel [129, 130, 133, 140, 143–147]. In most of the techniques a heat treatment under reducing atmosphere is necessary to obtain Eu^{2+} [130, 135, 136]. Aitasalo et al. [135] synthesized hexagonal and monoclinic $CaAl_2O_4$:Eu^{2+}. The single luminescence band of the hexagonal $CaAl_2O_4$:Eu^{2+} is at 448 nm which is at slightly longer wavelength than that of the monoclinic one (440 nm). They associated the band position shift with crystal field splitting of the 5d configuration being strongly affected by the environment [135]. They also concluded that the monoclinic phase is the most favorable phase of $CaAl_2O_4$ for luminescence application due to its higher luminescent intensity [135].

Eu^{2+} doped $CaAl_2O_4$ shows persistent luminescence characteristics [130, 135, 143]. Murayama et al. [148] used several co-dopants to increase the afterglow luminescence of Eu^{2+} doped $CaAl_2O_4$. They compared the afterglow characteristics of them with $CaAl_2O_4$: Eu^{2+}. Their observations are summarized

in table 5.4. Clearly, $CaAl_2O_4$: Eu, Nd (Eu: 0.5 *mol*%, Nd: 0.5 *mol*%) presents the longest decay profile. Co-doping does not always improve the afterglow luminescence of $CaAl_2O_4$: Eu. For example, using La, Mn, Sn or Bi as co-doping activator results in a lower afterglow luminescence intensity.

Co-dopant	Relative afterglow intensity after 100 min
-	1.00
Nd	27.78
Sm	13.89
Dy (2.5 *mol*%)	1.99
Tm	20.67
La	0.90
Ce	2.18
Pr	1.26
Gd	1.40
Tb	2.31
Ho	2.66
Er	1.09
Yb	1.42
Lu	1.38
Mn	0.54
Sn	0.81
Bi	0.53

Table 5.4: Influence of co-dopants on the afterglow of $CaAl_2O_4$: Eu. Co-dopant concentration is 0.5 *mol*%,otherwise it is specified [148].

Chapter 6

Luminescence and degradation of $CaS:Eu^{2+}$

6.1 Motivation

Rare earth doped alkaline earth binary and ternary sulfides have a special place in luminescent materials because of their relatively low synthesis temperature and broad emission spectra upon doping with europium and cerium [8, 149]. Particularly to obtain red or orange emission $CaS:Eu^{2+}$ and $SrS:Eu^{2+}$ are considered suitable candidates [11, 33, 69]. $Ca_{1-x}Sr_xS:Eu^{2+}$ phosphors with a strong absorption in the blue region are currently also used in white-light emitting diodes. Compared to the standard phosphor, YAG:Ce, the emission of $Ca_{1-x}Sr_xS:Eu^{2+}$ peaks at longer wavelengths, which allows the fabrication of light emitting diodes (LEDs) with lower color temperature and improved color rendering [8]. In addition to wavelength converters in LEDs, alkaline earth sulfide phosphors are employed in different areas such as displays [8], electroluminescent devices [9] and optical information storage [10]. Nevertheless, the lack of stability with respect to water and other atmospheric components hinders usage of the alkaline earth sulfides as phosphor hosts [8, 11–15]. One of the main goals of this study is to find a way to improve the stability of sulfides and we chose $CaS:Eu^{2+}$ as a model system due to its very high sensitivity against atmospheric conditions. If we can enhance the stability of $CaS:Eu^{2+}$, we can apply the same technique to other sulfides as well. But first of all, it is very important to know the properties and also the decomposition profile of the material which has to be protected. Therefore, a separate chapter on $CaS:Eu^{2+}$ is included in this thesis.

All CaS:Eu^{2+} micro-particles in this thesis were prepared using a solvothermal synthesis method. This technique is described in section 3.1. This method has several advantages over traditional preparation techniques and some of them are listed below:

- **Lower synthesis temperature**. For example, crystalline CaS:Eu^{2+} is synthesized using the solvothermal method at only 170°C. When crystallites of the same material are prepared using a solid state reaction, typically 1000-1200°C [70, 150, 151] is required.

- **Environmentally friendly**. In solvothermal synthesis, no toxic gases like H_2S are used. In addition to that the required energy for the synthesis is quite low when compared to traditional methods.

- **Diffusion and growth control**. These can be done by choosing a suitable solvent. Also by adding capping agents, size and shape of the materials can be controlled.

After the synthesis, CaS :Eu^{2+} particles were kept in ethanol, to prevent degradation caused by humidity. Typical particle sizes were between 0.25 and 0.75 μm, with clearly defined crystal faces. Phosphor layers were obtained by dripping the suspension on a (100)-oriented silicon substrate and drying in air at 40°C. This process was reiterated a number of times until complete coverage of the substrates with CaS :Eu^{2+} particles was obtained.

This chapter begins with crystallographic and luminescent characterization of CaS :Eu^{2+} particles. Then we will deal with the degradation of CaS :Eu^{2+} in two conditions.

6.2 Crystallographic and luminescent characterization of CaS :Eu^{2+}

CaS:Eu particles have a face-centered cubic crystallographic structure with a lattice constant of 0.57 nm. Figure 6.1 indicates the XRD spectrum of a drop-coated CaS:Eu layer and the reference peak positions and diffraction intensities of CaS (ICDD file no. 65-7852). When the reference peak ratios are compared with the experimentally obtained ratios, it observed that they are almost equal. This means that there is no specific orientation for the CaS:Eu particles when deposited on a substrate.

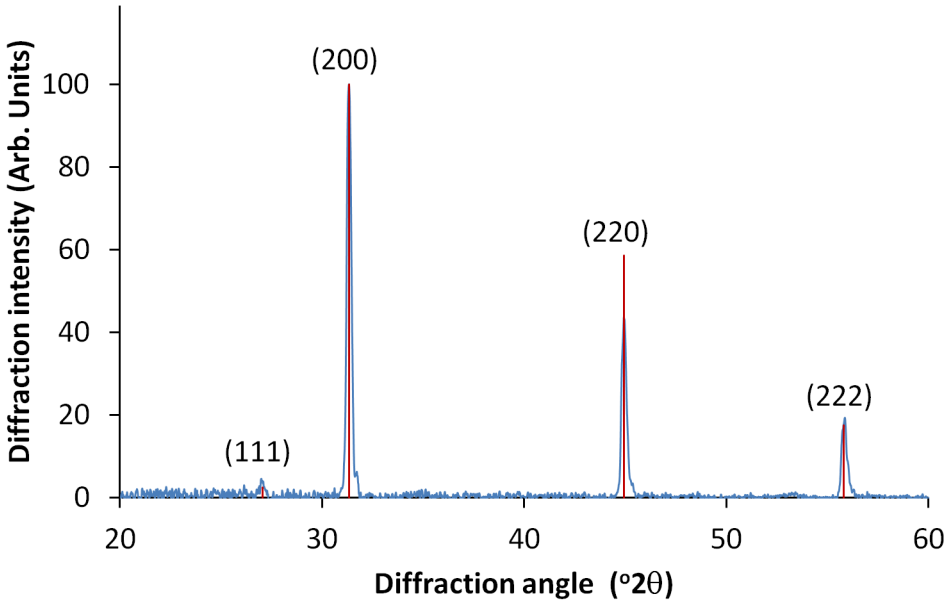

Figure 6.1: Diffraction pattern of CaS:Eu crystallites. The red lines indicate the peak positions and diffraction intensities of CaS (data from ICDD file no. 65-7852).

A SEM image of CaS:Eu particles is shown in Fig. 6.2. Octahedral shaped particles are seen and particle size range is rather limited (between 0.25 and 0.75 μm).

Due to the cubic crystal structure of CaS, the 5d orbital of Eu^{2+} splits in two levels e_g and t_{2g}. Explanation in detail about the crystal field splitting of Eu^{2+} can be found in section 2.1.8.2. The PL excitation and emission spectra of CaS:Eu layer are shown in Fig. 6.3. Measurements were carried out at room temperature. The excitation measurement is probed at an emission wavelength of 650 nm. While the direct excitation from the $4f^7$ ($^8S_{7/2}$) ground state to the $4f^65d$ (t_{2g}) excited state is responsible for the low energy (high wavelength) side excitation band peaking at 450-500 nm, the high energy (low wavelength) side excitation band between 250 and 300 nm is due to the combination of the CaS bandgap transition and the excitation to the $4f^65d$ (e_g) state in Eu^{2+}. The emission measurement is carried out at an excitation wavelength of 450 nm. A single peak at 650 nm with a FWHM of 68 nm is seen in the emission spectrum of CaS:Eu layer which is in line with the literature data [32, 69]. This peak is assigned to the transition from the $4f^65d$ (t_{2g}) excited state of Eu^{2+} to the $4f^7$ ($^8S_{7/2}$) ground state of Eu^{2+} [20].

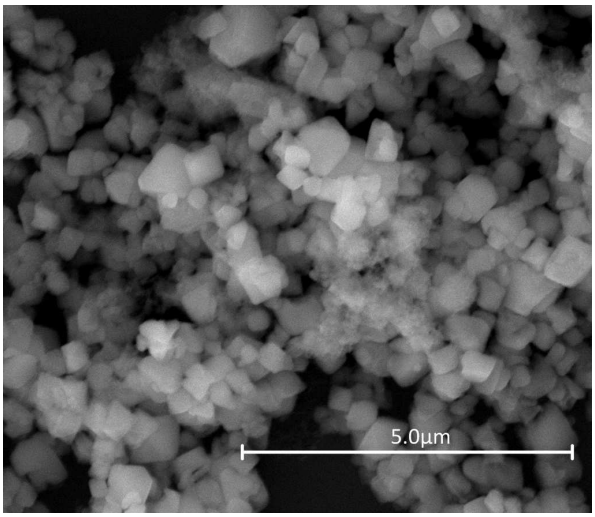

Figure 6.2: SEM image of CaS:Eu.

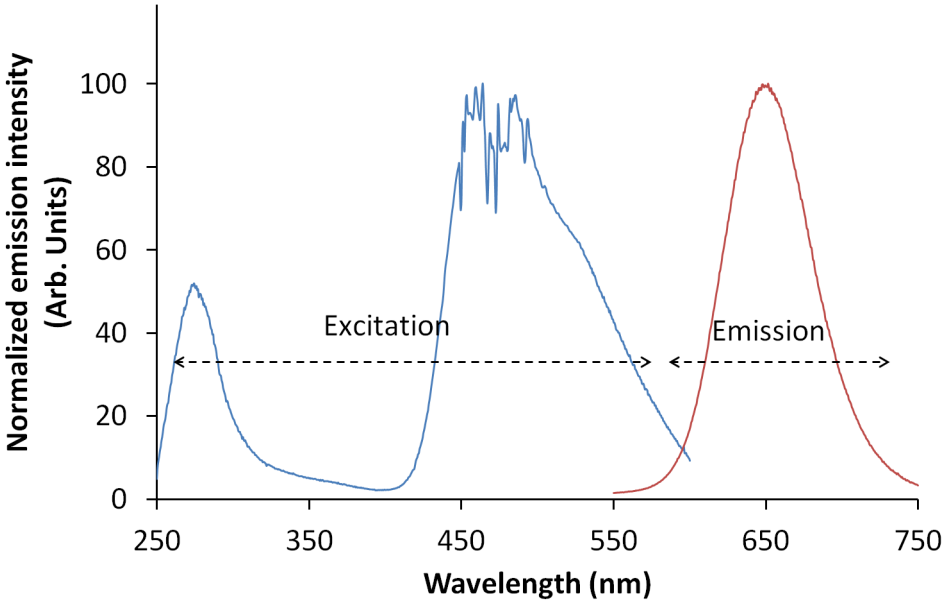

Figure 6.3: Normalized emission and excitation spectra of CaS:Eu. The excitation spectrum is recorded at an emission wavelength of 650 nm. The emission spectrum is recorded at an excitation wavelength of 450 nm.

6.3 Degradation study of CaS:Eu^{2+}

CaS:Eu^{2+} is unstable with respect to water, oxygen and carbon dioxide in air (§5.2.3). During this study, to improve the stability of CaS:Eu^{2+}, it was

coated with TiO_2 or Al_2O_3 layers. However, it is also important to know the details of the decomposition of CaS:Eu^{2+}. Therefore, the degradation study of CaS:Eu^{2+} is observed under two conditions. In the first one, a CaS:Eu^{2+} layer is put in a humidity chamber at 80°C and 80% relative humidity (RH) and this is called "low temperature degradation". The chemical stability of the phosphor layers is inspected with an in situ photoluminescence measurement during accelerated aging of samples in the humidity chamber. Additionally after this treatment, the effects of the degradation of the CaS :Eu^{2+} particles are investigated.

In the course of this study TiO_2 and Al_2O_3 prepared via sol-gel method are used as protection layer for CaS:Eu^{2+}. After the coating, heat treatments at 400°C and 500°C are necessary to remove the organic compounds from the TiO_2 and Al_2O_3 layers, respectively. To assess the influence of the heat treatment on particle decomposition, uncoated phosphor layers were also subjected to heat treatment at 400°C, 450°C and 500°C for 30 min in air (second condition). This experiment is called "high temperature degradation". The influences of the degradation of the particles are studied after the heat treatment.

6.3.1 Low temperature degradation

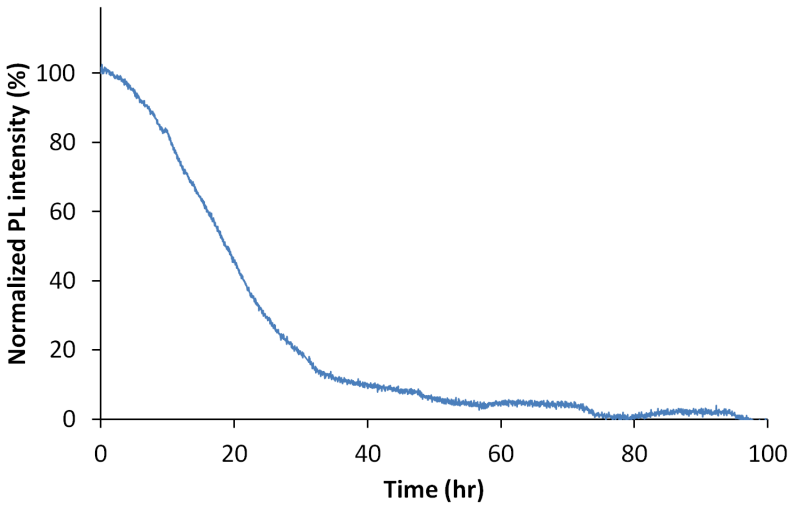

Figure 6.4: PL intensity of CaS:Eu layer as a function of time at 80°C and 80% RH.

Low temperature degradation of CaS:Eu is observed in a humidity chamber

at 80°C and 80% RH. PL intensities of the CaS:Eu layer as a function of the exposure time are shown in Fig. 6.4. This figure expresses that after 30 h the PL emission of uncoated CaS:Eu has almost entirely disappeared. After 75 h, the PL intensity of the uncoated phosphor is not detectable anymore.

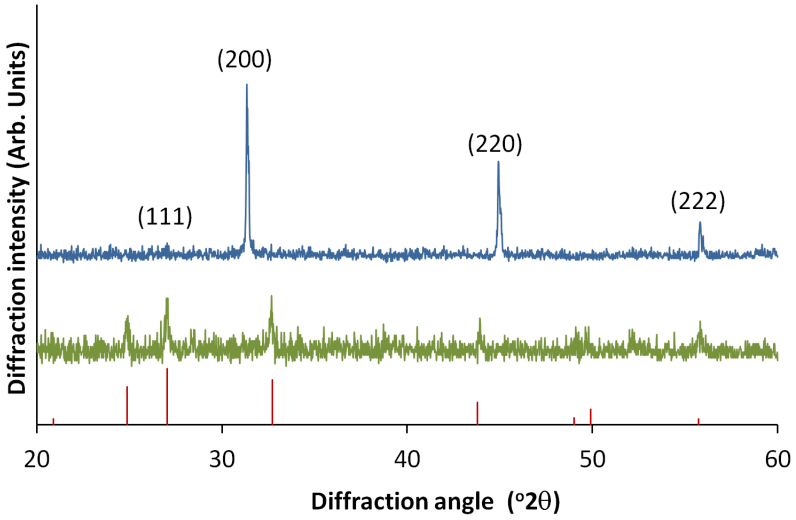

Figure 6.5: XRD spectra of CaS :Eu^{2+} particles, before (blue line) and after (green line) 100 h of accelerated ageing at 80°C and 80% RH. The reference diffraction peaks of CaS (ICDD file No. 65-7852) are indicated. Red lines represent the peak positions of $CaCO_3$ (data from ICDD file No. 72-0506).

The XRD patterns of CaS:Eu before (blue line) and after (green line) 100 h aging are presented in Fig. 6.5. The peaks related to CaS disappear after the accelerated ageing process and only $CaCO_3$ peaks with small intensity are observed. This is evidence of the decomposition of CaS to $CaCO_3$ in the presence of CO_2 and H_2O at lower temperature (equation 6.1) [72,152]. Since amorphous components can not be detected by means of the XRD measurement, we could not identify the amorphous reaction products, which might be formed during reaction of CaS with H_2O.

$$CaS + H_2O + CO_2 \rightarrow CaCO_3 + H_2S \tag{6.1}$$

García-Calzada and colleagues [73] also studied decomposition of CaS powder with an average particle size of 18.6 μm. They investigated the decomposition at room temperature in air saturated with water. They observed that while sulfur as H_2S gas is released during the first 48 hours, there is no change

in sulfur concentration afterwords, since $CaCO_3$ and sulfur-oxygen salts of calcium such as $CaSO_3$ and $CaSO_4$ created an protection layer on the CaS particles. In contrast to our observation, the strongest peak still belongs to CaS in the XRD diffraction pattern of the solid sample decomposed for 11 days in the García-Calzada and colleagues' study. We attribute this change to particle size difference. The particles which we used during this study are almost 20 times smaller in diameter than that of García-Calzada and colleagues used. As Madarász et al. reported [13], small particles decompose faster than bigger ones. It could be that small particles decompose before an impervious layer forms.

6.3.2 High temperature degradation

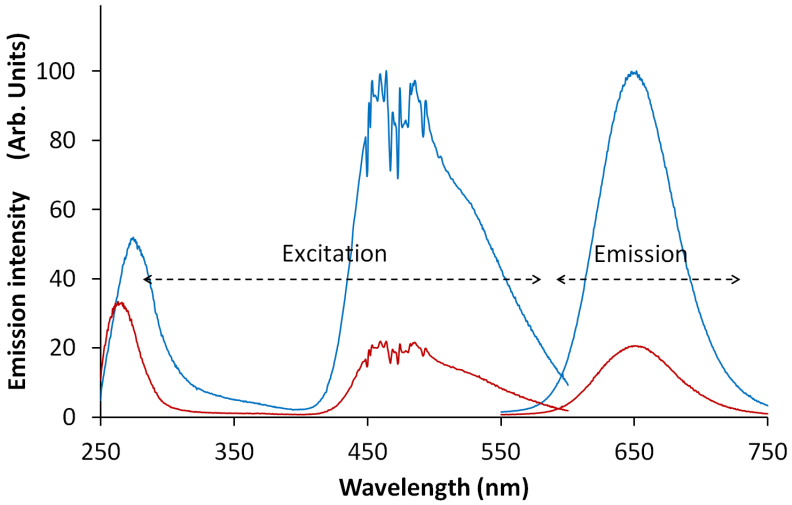

Figure 6.6: PL emission and excitation spectra of CaS:Eu before (blue line) and after heat treatment (red line) at 500°C for 30 min in air. The excitation spectrum is recorded at an emission wavelength of 650 nm. The emission spectrum is recorded at an excitation wavelength of 450 nm.

PL excitation spectra of CaS:Eu^{2+} before (blue line) and after (red line) heat treatment at 500°C for 30 min in air are shown in Fig. 6.6. The excitation spectra are recorded at an emission wavelength of 650 nm. The shape of the low energy side excitation band, which is the excitation to the $4f^6 5d$ (t_{2g})state in Eu^{2+}, does not change. Nevertheless, the intensity of the peak decreases after treatment. The high energy side excitation band between 250 and 300 nm is a combination of the CaS band gap transition and the excitation to

the 4f^{6}5d (e_g)state in Eu^{2+}. A decrease of the CaS:Eu^{2+} particle size due to the partial decomposition results in a relative increase of the intensity of the excitation peak from the CaS band gap because of the different absorption lengths for both processes. This changing of the relative ratio between these two peaks results in a shift of the high energy side band in the excitation spectrum of CaS:Eu^{2+} [7]. PL emission spectrum of CaS:Eu before (blue line) and after heat treatment at 500°C for 30 min in air (red line) are presented in Fig. 6.6. The emission spectra are recorded at an excitation wavelength of 450 nm. As expected, the PL intensity decreases after heat treatment. The PL intensity reduces to 21% of the initial intensity after a heat treatment at 500°C.

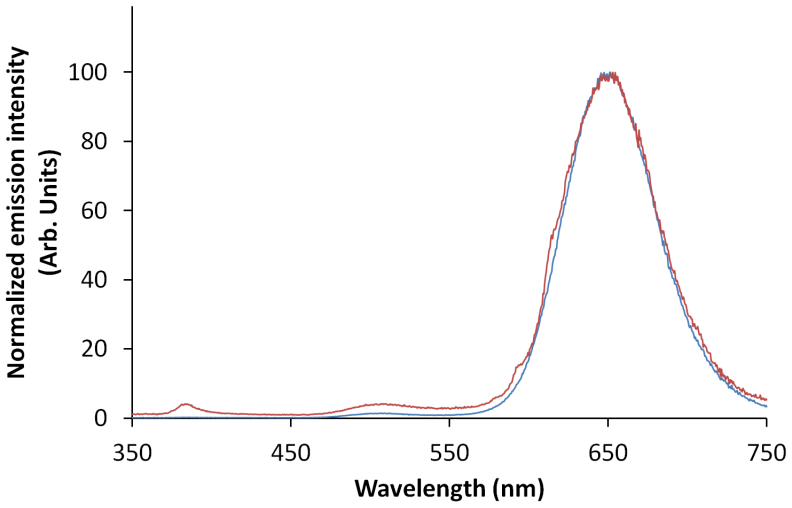

Figure 6.7: Normalized PL emission spectra of CaS:Eu^{2+} before (blue line) and after (red line) heat treatment at 500°C for 30 min in air recorded at an excitation wavelength of 275 nm.

To monitor whether $CaSO_4$ is formed or not upon degradation, the PL emission spectra recorded at an excitation wavelength of 275 nm of CaS:Eu^{2+} before (blue line) and after (red line) heat treatment at 500°C for 30 min in air are shown in Fig. 6.7. The small emission peak at 385 nm is formed after heat treatment and this peak is correlated with $CaSO_4$:Eu^{2+} [75–78]. This indicates the (partial) decomposition of CaS:Eu^{2+} to $CaSO_4$:Eu^{2+}. The broad peak at 500 nm could not be identified. As seen in Fig. 6.7, there is a deformation in the red emission peak after the heat treatment. This presumably suggests the formation of other luminescent centres such as Eu^{3+} [75–78].

Number of cycles	PL intensity after annealing at 400°C (%)	PL intensity after annealing at 450°C (%)	PL intensity after annealing at 500°C (%)
0	100	100	100
1	74	50	21
2	49	34	31
3	42	38	33
4	39	42	33
5	35	38	34

Table 6.1: PL emission intensity at 650 nm as a function of annealing temperatures and the number of treatments.

In order to do further research on decomposition process of CaS:Eu, successive heat treatments at three different temperatures were performed. The results are summarized in table 6.1. As seen in this table, using higher temperatures accelerates the decomposition process. The first heat treatment at 400°C results in 74% of the initial PL emission intensity, while the samples have only 50% and 21% left after annealing at 450 and 500°C, respectively. After the second treatment, the PL intensities at 650 nm of the samples do not decrease anymore and they have almost the same values. It indicates the formation of a protective layer such as $CaCO_3$, $CaSO_3$ or $CaSO_4$ as Madarász et al. suggested [13].

The PL emission spectrum recorded at an excitation wavelength of 275 nm already indicates the formation of $CaSO_4$ and for more details about the compounds, which are formed during degradation of CaS:Eu, XRD measurements were performed. The XRD spectra of CaS:Eu before and after annealing at 400°C and 500°C are presented in Fig. 6.8. The XRD spectrum indicates the formation of two $CaSO_4$ phases after the first heat treatment at 400°C and 500°C. No peaks related to $CaCO_3$ are seen in the spectrum. This expresses that at low temperatures, CaS decomposes to $CaCO_3$ while at higher temperatures it decomposes to $CaSO_4$. The XRD spectrum also highlights the acceleration of CaS decomposition with an increase in temperature.

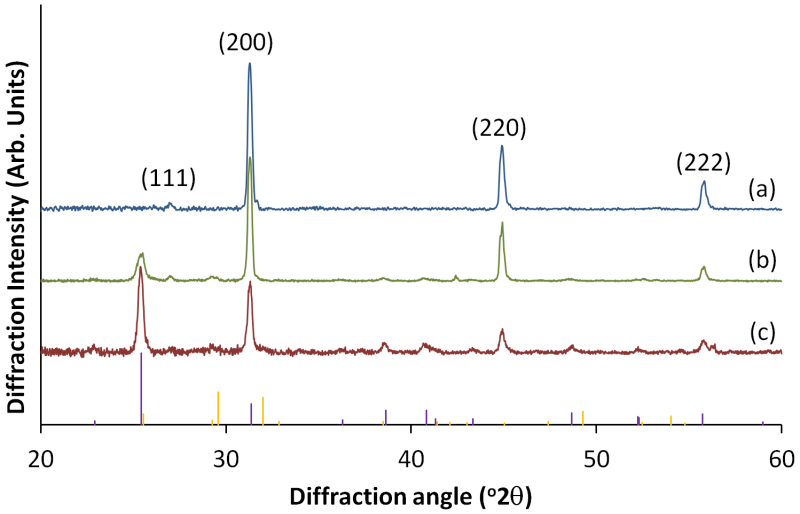

Figure 6.8: XRD spectra of CaS:Eu^{2+} particles, before (a) and after heat treatment at 400°C (b) and 500°C for 30 min in air. The reference diffraction peaks of CaS (data from ICDD file No. 65-7852) are indicated. Purple lines represent the peak positions of $CaSO_4$ (data from ICDD file No. 37-1496) and orange lines represent the peak positions of γ-$CaSO_4$ (data from ICDD file No. 89-1458).

6.4 Conclusions and perspectives

In this chapter degradation of CaS:Eu^{2+} particles prepared with solvothermal synthesis was investigated under two conditions. In the first condition, a silicon substrate covered with CaS:Eu^{2+} particles was kept in a humidity chamber at 80°C and 80%. Under this condition, formation of crystalline $CaCO_3$ was observed by the partial decomposition of CaS (Fig. 6.5). However, the diffraction peaks of $CaCO_3$ are much smaller than those of CaS. This expresses the formation of amorphous phases whose chemical composition can not be determined by XRD. It is also observed that in 18 hours, the PL emission intensity reduces to half of the initial intensity (Fig. 6.4).

In the second condition, decomposition of CaS:Eu^{2+} is examined after heat treatment at 400, 450 and 500 °C in air. Under this condition, degradation of CaS to $CaSO_4$ is recorded by XRD and PL emission measurements (Figs. 6.7 and 6.8). Additionally, it was observed that while in the first stage of heat treatment, temperature has a big influence on the degradation rate (degradation rate is increased by temperature), after a second treatment there is a limited effect of temperature on the degradation. This fact is

presumably related to formation of $CaSO_4$ which covers the CaS surface and acts as protection layer. After the second treatment this layer reaches a certain thickness and does not allow to pass gases and water (table 6.1).

Chapter 7

TiO_2 powders and thin films

7.1 Motivation

TiO_2 is a well known inorganic oxide due to its broad application area. Although for most of these applications anatase TiO_2 is favoured, rutile TiO_2 is commonly used in the paint industry as a white pigment in paints, as it scatters light more efficiently, is more stable and more durable than anatase pigments [153]. TiO_2 is transparent in the visible range and has a wide optical band gap [90,104,105,154,155]. This, together with its chemical and thermal stability, makes TiO_2 an excellent candidate for optical coatings [44,92,156]. During this study TiO_2 prepared with a non-aqueous sol-gel method was used as protection coating but we could not disregard the other potential application areas like water and air purification. TiO_2 coatings with high photoactivity are attractive as photocatalytic, self-cleaning or anti-fogging materials (due to their superhydrophylicity) and for solar energy conversion [94, 95, 157]. Therefore, TiO_2 prepared during this study as protection layers, was also subject of Lisanne Van Puyvelde's master thesis [158] as photocatalytic material.

This chapter focuses on TiO_2 prepared with two non-aqueous sol-gel ways, more details about the preparation methods can be found in section 3.3. Using the first way, two sols with different concentrations (0.5 M and 2.4 M) were synthesized. The viscosity of the 0.5 M sol is 3.77 mPa.s and that of the 2.4 M sol is 6.85 mPa.s. The TiO_2 sol prepared in the second way has a viscosity of 2.26 mPa.s. Using these methods powders, thin films and protection layers were fabricated. This part starts with thermal analysis of the sols. After discussing crystallization and phase transformations of powder samples, morphology, thickness and optical properties of thin films

will be exposed. Lastly, the performance of TiO_2 as protection layer will be evaluated. Several results in this chapter were published in the Journal of Sol-Gel Science and Technology [3].

7.2 Thermal analysis (TGA/DTA)

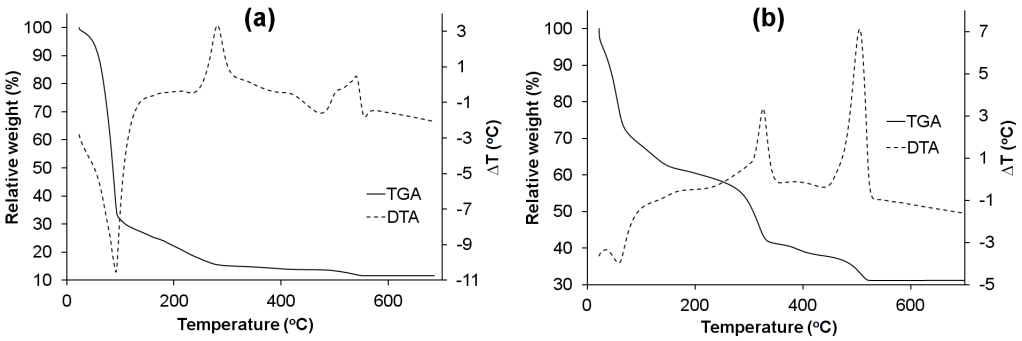

Figure 7.1: The TGA/DTA analysis of TiO_2 sols synthesized by method 1 **(a)** and 2 **(b)** with a heating rate of 10°C/min in an air flow.

Figure 7.1a and b show TGA and DTA on TiO_2 sols prepared using method 1 and method 2, respectively. For method 1, most of the solvent evaporates below 100°C (boiling point of n-butyl alcohol is 118°C). Weight loss between 100 and 270°C is considered to be due to the volatilization and thermal decomposition of the remaining organics like butanol, acetyl acetone and acetate groups during gelation. The weight loss in the temperature range 270-535°C is related to loss of carbon groups in the structure. Above 535°C the weight loss curve levels off. The TGA-DTA on the sample prepared with method 2 shows that three important weight loss steps from room temperature to 510°C take place. The first weight loss (from room temperature to 65°C) results from evaporation of the solvent, note that some of the solvent (ethanol) has already evaporated before the measurement due to its low boiling point (78°C). Therefore, the first weight loss is lower when it is compared to Fig. 7.1a. This also affects the total weight loss, total weight loss is only 69% in method 2, while it is 89% for method 1. The second weight loss (from 65 to 325°C) corresponds to the calcination of organic compounds and the last (from 325 to 510°C) is due to loss of carbon groups in the structure [44].

7.3 Crystallization and phase transformations of powders

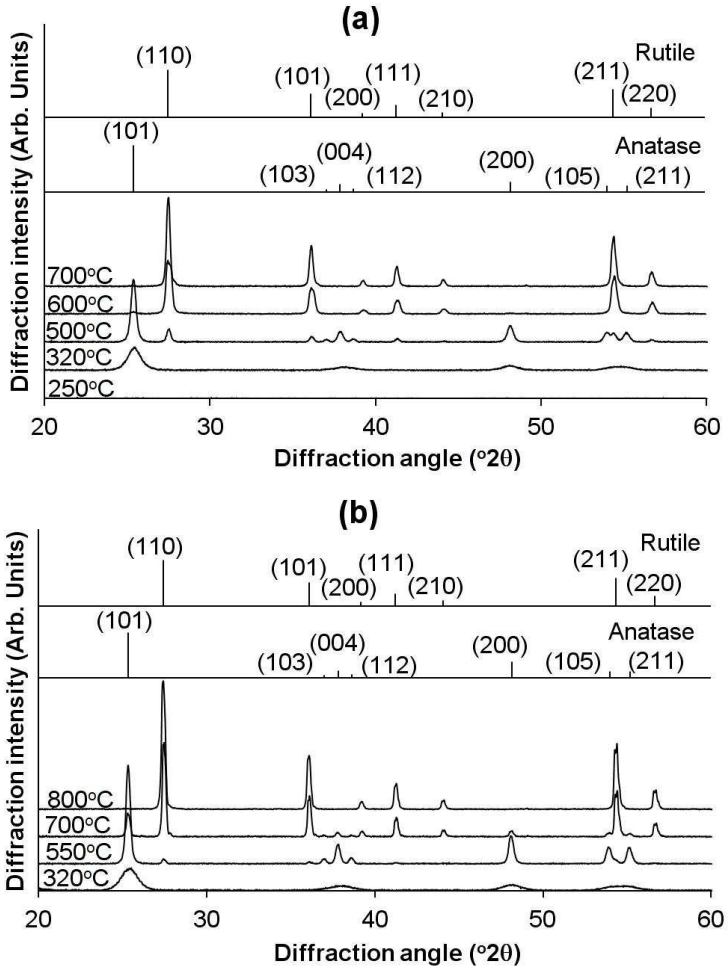

Figure 7.2: XRD spectra of TiO_2 powders prepared using method 1 **(a)** and 2 **(b)** heat treated at various temperatures in air for 2 h with anatase and rutile peaks representing data from ICDD file No. 21-1272 and ICDD file No. 21-1276, respectively.

Figure 7.2 presents the XRD spectra of TiO_2 powders prepared with both methods and heat treated at different temperatures for 2 h with a heating rate of 10°C/min in air. The powder heat treated at 250°C is amorphous while the one heat treated at 320°C is pure anatase. This is in line with the DTA result at 320°C (Fig. 7.1a) where we observed an exothermic peak. In method 1 samples, the rutile phase begins to form when the temperature is

around 500°C which is also revealed in the DTA result (Fig. 7.1), but the anatase phase is still present. When the XRD spectra at 500 and 600°C are compared, it is clear that rutile TiO_2 is getting more dominant at 600°C, with still some small peaks which are related to the anatase phase, while the peaks for the rutile phase are relatively intense. At 700°C the TiO_2 powder has been converted to pure rutile for the samples prepared with method 1. The transition from anatase to rutile begins around 550°C for TiO_2 powders prepared with the second method (Fig. 7.2b). The sample heat treated at 700°C still has the mixed anatase-rutile phase, in contrast to TiO_2 powders prepared with the first method. Pure rutile phase formation for the samples synthesized with method 2 was obtained at 800°C. When the TGA, DTA and XRD results for methods 1 and 2 are combined, it indicates that the preparation technique does not have a pronounced effect on the transition temperatures in powders from amorphous to anatase and from anatase to rutile when heated in air.

The colour of the powder heat treated at 250°C is gray. Although crystallization occurs around 320°C in air for both types of samples (methods 1 and 2), the colour of the powder remains gray upon annealing to 320°C, while the powder annealed at 350°C in air is white. There are two reasons for the gray colour of the TiO_2 powders; the first one is the low annealing temperature which is not enough to remove organic constituents from the structure [159], the second one is the lack of oxygen in the structure [89]. Increase of the heat treatment temperature in air results in rapid oxygen uptake, leading to more stoichiometric titanium dioxide.

The X-ray diffraction peaks of the powders show a significant broadening due to the small size of crystallites. The average crystallite sizes (D) were calculated from the most intense diffraction peak (101) using Scherrer's formula (equation 4.5). Variation of the crystallite size of anatase TiO_2 powder prepared via method 1 as a function of heat treatment temperature is shown in Fig. 7.3. It is seen that with increasing annealing temperature, the size of the anatase crystallites increases from 12.8 nm at 320°C to 23.1 nm at 450°C. Another important parameter for particle grown is reaction time. The particle size is 15 nm after annealing at 350°C for 2 h, but increases to 19.5 nm after annealing at 350°C for 10 h. The formation of the rutile phase around 500°C is accompanied by a drastic increase in anatase crystallite size, as seen in Fig. 7.3. TiO_2 powder prepared with method 2 shows a similar tendency but with slightly smaller crystal size. For example, at 350°C the crystal size of powder prepared with method 2 is 9 nm, while that of powder prepared with method 1 is 15 nm.

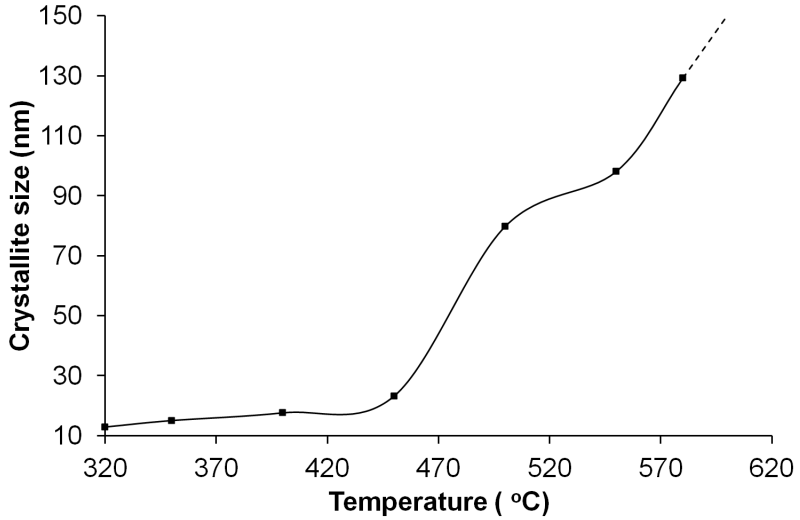

Figure 7.3: Crystallite size of anatase TiO_2 powder prepared using method 1 as function of annealing temperature (annealing for 2 h in air).

In order to investigate the effect of the heating atmosphere, helium was used as an inert atmosphere during heat treatment. The powder samples were heat treated in He atmosphere for 2 h at different temperatures of 400, 500, and 600°C with a heating rate 10°C/min. Upon comparison, it was obvious that changing the heating atmosphere from air to helium is shifting the phase transition temperature from anatase to rutile to higher values for both methods. Upon heating in air, transition temperatures from anatase to rutile for methods 1 and 2 are around 500 and 550°C, respectively (Fig. 7.2) while for both synthesis methods, TiO_2 powder heat treated at 600°C in helium atmosphere is still anatase. Although the powder annealed at 350°C in air is already white, the colour of powders annealed at 600°C in He is still gray.

The effect of the preparation technique on the phase transition was studied by in situ XRD. Figure 7.4 indicates the evolution of the intensities of the main XRD-peaks for anatase and rutile from TiO_2 powder prepared using method 1 and method 2, during heating under helium atmosphere from room temperature to 1000°C with a heating rate of 6 °C/min. Both TiO_2 powders were heat treated beforehand at 250°C in air with a heating rate of 10 °C/min, in order to remove most of the organics. For the powder synthesized by method 1, the transition from amorphous to anatase under He begins at around 500°C and the transition from anatase to rutile starts around 820°C

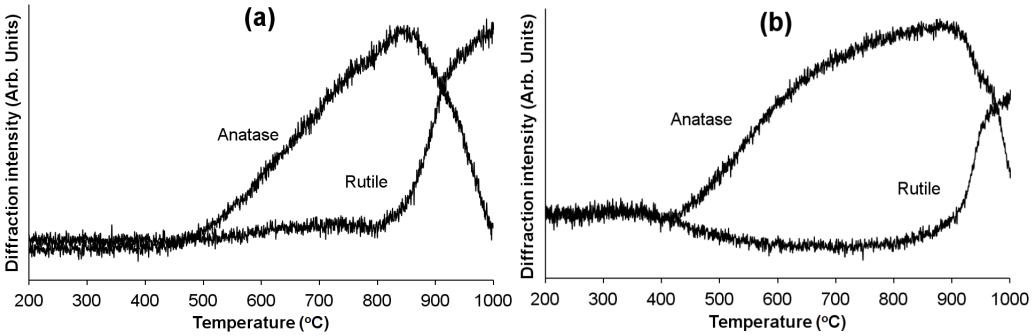

Figure 7.4: Evolution of the intensities of the main XRD-peaks for anatase and rutile from TiO_2 powder prepared using method 1 **(a)** and method 2 **(b)** as a function of anneal temperature in helium atmosphere with heating rate 6 °C/min.

(Fig. 7.4a). The transition from amorphous to anatase in helium atmosphere for the powder prepared using method 2 occurs at lower temperature than for synthesis method 1 (Fig. 7.4b). However, the transition temperature from anatase to rutile in helium atmosphere is higher than for method 1. It is clear that using method 2 to prepare the samples and heat treating them in helium atmosphere results in a broader temperature range for obtaining anatase TiO_2. Note that even after a heat treatment at 1000°C in helium atmosphere, the colour of the powders is gray instead of white which indicates the presence of oxygen vacancies in the structure [89].

7.4 Morphology, thickness and optical properties of thin films

Figure 7.5 shows XRD spectra of TiO_2 thin films prepared with method 1 after spin coating on a Si substrate, annealed at 320 and 700°C in air with a heating rate of 10 °C/min for 2 h. The XRD spectrum of the film annealed at 320°C indicates that the formation of anatase occurs just like for the TiO_2 powder prepared with method 1 annealed at 320°C. The XRD spectrum of the TiO_2 thin film annealed at 700°C shows peaks related to both anatase and rutile. A thin film prepared with method 2, after heat treatment at 750°C in air with a heating rate of 10 °C/min for 2 h was still anatase (Fig. 7.5). When the XRD results of powders and thin films are compared, it is clear that the anatase phase remains stable at higher temperatures in thin films. This may be attributed to stress effects related to structural limitation

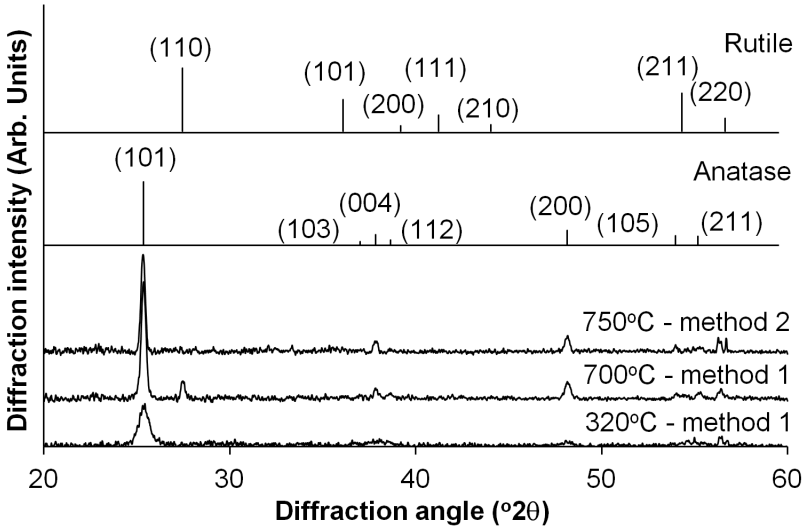

Figure 7.5: XRD spectra of TiO_2 thin films on silicon substrate prepared using method 1, heat treated at 320 and 700°C and prepared using method 2, heat treated at 750°C in air for 2 h with anatase and rutile peaks representing data from ICDD file No. 21-1272 and ICDD file No. 21-1276, respectively.

on reorganisation and changing the phase on the film ans substrate interface.

For all thin films heat treated in air, crystallization begins at 320°C no matter which substrate (glass or silicon) is used. XRD spectra of TiO_2 films on silicon and glass substrate are shown in Fig. 7.6. The films were synthesized with method 2 and then heat treated at 550°C in air with a heating rate of 10 °C/min for 2 h. As seen in Fig. 7.6, TiO_2 films have only anatase phase at 550°C unlike the corresponding powder samples, where some rutile was present (see Fig. 7.2b). It is also clearly seen in Fig. 7.6 that there is no effect of substrate type on the crystallization of films.

Film thickness and optical constants of a number of thin films were determined using spectroscopic ellipsometry. The optical properties of the TiO_2 films were modelled using the Cody-Lorentz dispersion model. This model includes the normal dispersion and the absorption behaviour of typical films in the vicinity of the band gap and thus it offers more realistic result in both transmitting and absorbing regions [105] [106] [160]. The optical model included surface roughness [105] [106]. The latter was found to be below 6.5 nm in all cases and not accounted for in further analysis.

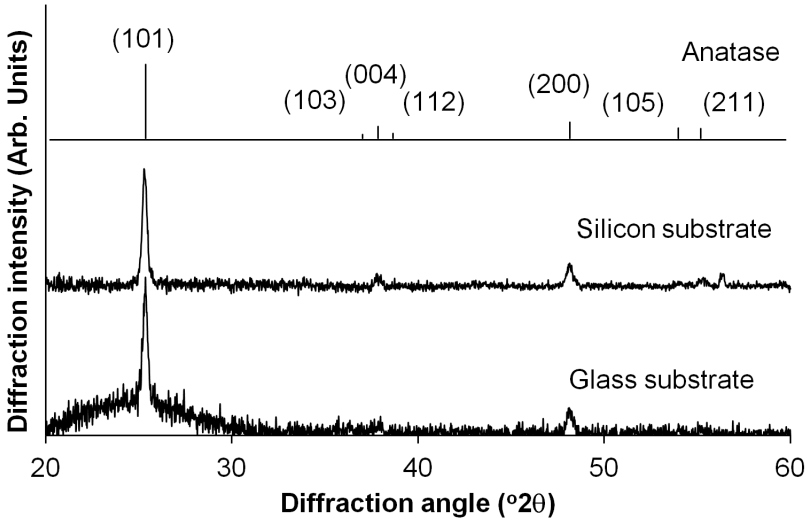

Figure 7.6: XRD spectra of TiO_2 thin films prepared using method 2 on glass and silicon substrates heat treated at 550°C in air for 2 h with anatase peaks representing data from ICDD file No. 21-1272.

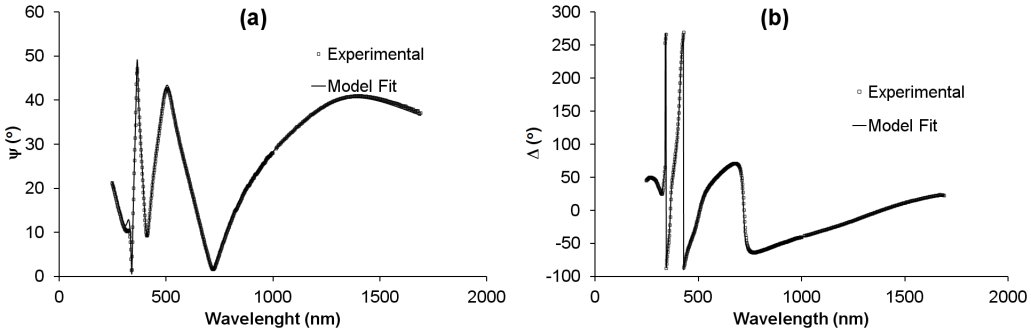

Figure 7.7: Experimental and fitting result of ψ - λ **(a)** and Δ - λ **(b)** of TiO_2 thin film prepared using method 1, spin coated at 2000 rpm on silicon substrates and heat treated at 400°C.

As an example, figure 7.7 shows the measurement and fitting results of the ellipsometric angles ψ and Δ as a function of wavelength (λ) of a TiO_2 film prepared using method 1 and heat treated at 400°C. As seen in this figure the experimental data are in excellent agreement with the model fit curves.

Table 7.1 summarizes the results from spectroscopic ellipsometry analysis on TiO_2 films. The influence of the viscosity was investigated using the films prepared in the same way but with different viscosity. Comparing sample

Sample	Viscosity (mPa.s.)	Substrate	Spin speed (rpm)	Annealing temperature (°C) and time	Thickness (nm)	n @ 632.8 nm	Band gap energy (eV)
A	3.77	Si	5000	400, 30 min	29.9	2.22	3.43
B	6.85	Si	5000	400, 30 min	149.9	1.92	3.39
C	6.85	Si	2000	450, 120 min	161	2.11	3.33
D	6.85	Si	2000	700, 120 min	141	2.32	3.38
E	6.85	Si	2000	500, 30 min	81.8	2.09	3.34
F	6.85	Glass	2000	500, 30 min	163.5	1.96	3.43
G	6.85	Si	6000	400, 30 min	138.3	1.92	3.38
H	6.85	Si	2000	400, 30 min	201.5	2.05	3.38
I	6.85	Glass	5000	500, 30 min	107.9	1.95	3.40

Table 7.1: Influence of deposition conditions on the thickness and optical properties of TiO_2 films prepared by method 1.

A and B, it was observed that increasing the viscosity leads to thicker films with lower refractive index. This indicates that increasing the viscosity results in an increased porosity of the films. Increasing the heating temperature induces thinner films with higher refractive index. The influence of the heating temperature was studied using the same thin films heated to different temperatures (e.g., samples C and D). These two samples were prepared to investigate the differences between thin films and powders; hence they were heat treated for 120 min. An increase in temperature results in denser and thinner films. This effect is expected: at higher temperature, grain growth (Fig. 7.3) and compacting of the film leads to a decrease in porosity and consequently to decrease in thickness. The substrate type also influenced the thickness and the refractive index of films. Using a glass substrate resulted in thicker films with lower refractive index such as sample E and F in table 7.1. It may be related to different surface morphology of glass and Si substrates. The effect of the spin speed was also investigated (samples G and H). Using lower spin speed to coat the substrate led to thicker layers and higher refractive index. In these two synthesis techniques no additional water was used; partial hydrolysis of precursors occurs with esterification reaction for method 1 and residual water in ethanol for method 2. Therefore condensation starts before hydrolysis is complete. Condensation between incompletely hydrolyzed species gives rise to weakly branched (extended) cluster-cluster growing. Such weakly branched systems finally yield densely packed film after heat treatment [1].

Using the measurement and equation 7.1, the absorption coefficient, α, was calculated between 250 and 1700 nm:

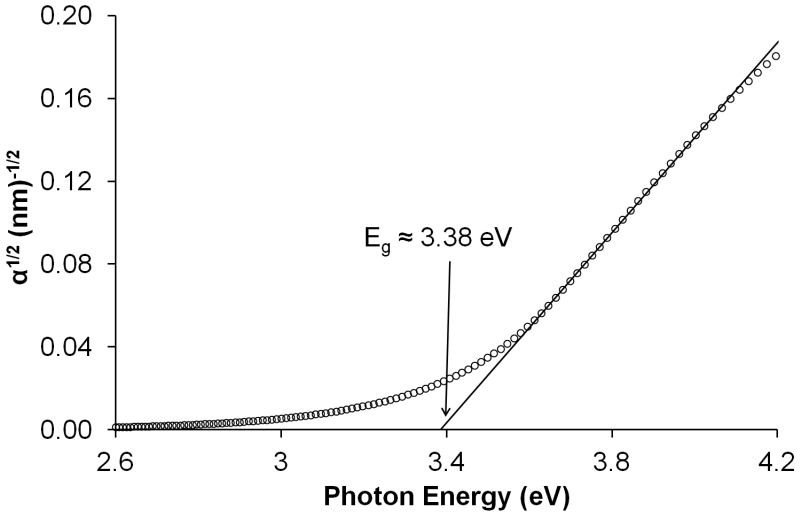

Figure 7.8: Fit of $\alpha^{1/2}$ as a function of the photon energy of the same thin films as in figure 7.7 with a linear trend line.

$$\alpha = \frac{4\pi k}{\lambda} \tag{7.1}$$

Where λ is the wavelength and k is the extinction coefficient (the imaginary part of the refractive index). When the square root of the absorption coefficient is plotted as a function of photon energy, E, the indirect allowed optical band gap energy, E_g, can be deduced from the intersection of the linear part of the curve with the x-axis [104, 105, 154].

$$\alpha = \alpha_o \left(E - E_g\right)^2 \tag{7.2}$$

Here α_o is a constant. An example of the plot of $\alpha^{1/2}$ versus photon energy of the thin film mentioned in Fig. 7.7 is illustrated in Fig. 7.8, including a trend line of the linear part of the curve. The optical band gap energy of the thin films prepared with the solution with the viscosity of 6.85 mPa.s (method 1), spin coated on Si substrate at different speeds and heat treated at different temperatures from 400 to 700°C is 3.37±0.03 eV. The optical band gap energy of the former films on glass substrate is 3.43±0.03 eV. Similar values can be found in the literature [104, 105, 154, 155]. As seen in table 7.1, no significant effects of the film preparation on the band gap were found, even when the film was partially converted to the rutile phase.

Figure 7.9a presents high magnification SEM images of a TiO_2 film prepared using method 1; the thickness of the film is 201.5 nm, the refractive index

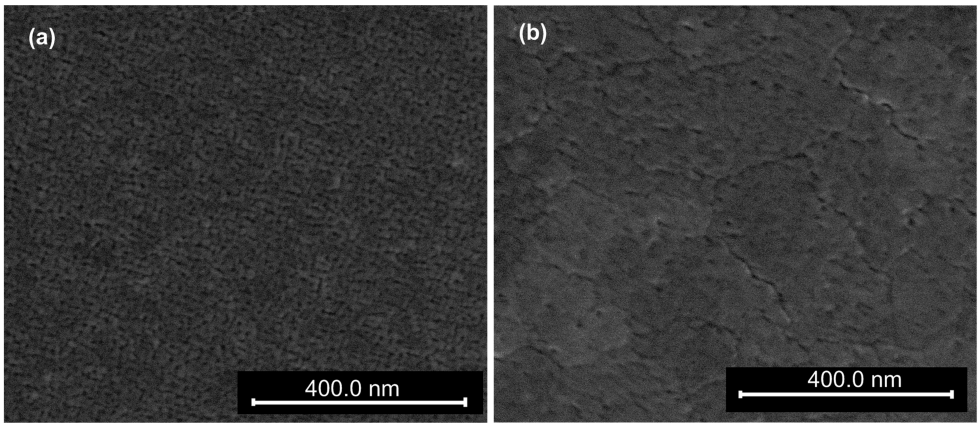

Figure 7.9: SEM images of TiO_2 films on Si prepared using (a) method 1, (b) method 2.

is 2.05 and the average crystal size (as calculated from XRD) is 15.2 nm. Figure 7.9b presents the SEM images of a TiO_2 film prepared using method 2; the thickness of this film is 110.8 nm, its refractive index 2.17 and the average crystal size is 25.7 nm. Both films present a homogeneous and crack free surface. It is seen in Fig. 7.9a, b that the film prepared with method 2 has a larger grain size, consistent with the XRD results.

7.5 TiO_2 as a protection layer

It was mentioned at the beginning of this chapter that the main purpose to prepare TiO_2 thin films is to use them as protection layer. So far we only dealt with the characteristics of standalone TiO_2 powders and thin films.

One of the main requirements for protection layers is transparency. If the film is not fully transparent at the excitation (450 nm) and emission (650 nm) wavelengths of CaS:Eu, it causes a decrease in the emission intensity. Transmission spectra of TiO_2 films on Corning 1737 substrates prepared by method 1 are shown in Fig. 7.10. After the spin coating at 2000 (F) and 5000 rpm (I), samples were heat treated at 500°C for 30 min. Optical constants of these samples were also calculated using spectroscopic ellipsometry and they are listed in table 7.1.

A 0.7 mm thick Corning 1737 substrate has a 70% transmission at 300 nm and the refractive index at 589.3 nm of the Corning 1737 substrate is 1.518. The transmission spectra were divided by the transmission of Corning 1737

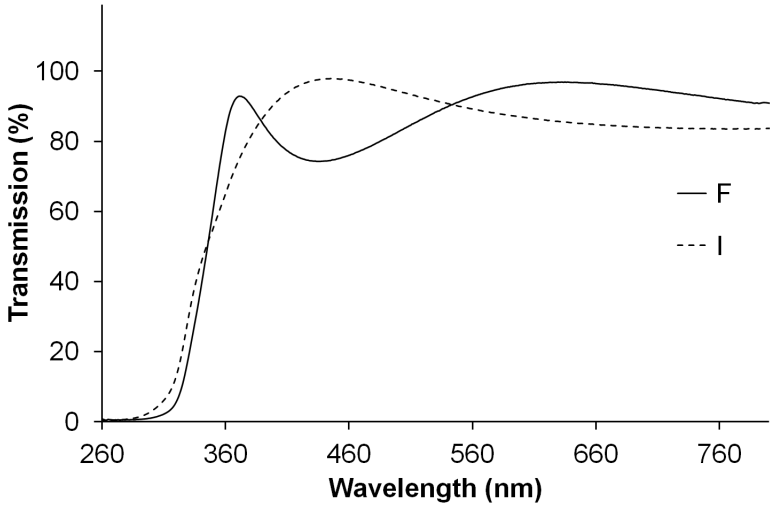

Figure 7.10: Transmission spectra of TiO_2 films prepared by method 1, spin coated at 2000 rpm (solid line, sample F) and 5000 rpm (dashed line, sample I) on Corning 1737 substrates. Thin films were heat treated at 500°C for 30 min.

glass. As seen in the Fig. 7.10, interference fringes are getting visible by increasing the thickness of the films. As also seen in the transmission spectra of the TiO_2 films, they are fully transparent at excitation and emission wavelengths of CaS:Eu.

Before examining the effectiveness of TiO_2 as protection layer, we investigated the compatibility of TiO_2 sols and CaS:Eu^{2+} particles by adding the particles into the TiO_2 sols. The PL emission intensities at 650 nm of CaS:Eu^{2+} particles in ethanol, in TiO_2 sols prepared with method 1 and 2 were recorded as a function of time (Fig. 7.11). Measurements were recorded at an excitation wavelength of 450 nm. CaS:Eu^{2+} particles settle down with time, thus a decrease in the emission intensity is observed (Fig. 7.11, line a and b). During the preparation of both sols, although water is not added into the solutions, it is produced as a side product and it is used during hydrolysis. However the presence of water is still possible in the sols after the preparation. In this case, water quantity is crucial for coating the CaS:Eu^{2+} particles to protect against moisture. If the water quantity is high, the CaS:Eu^{2+} particles decompose immediately in the TiO_2 sol as seen in Fig. 7.11(line c). Using method 1 to prepare TiO_2 looks better than method 2 due to the higher emission intensity of CaS:Eu^{2+} in the sol. Therefore we continued with TiO_2 prepared with method 1 to protect CaS:Eu^{2+}. The

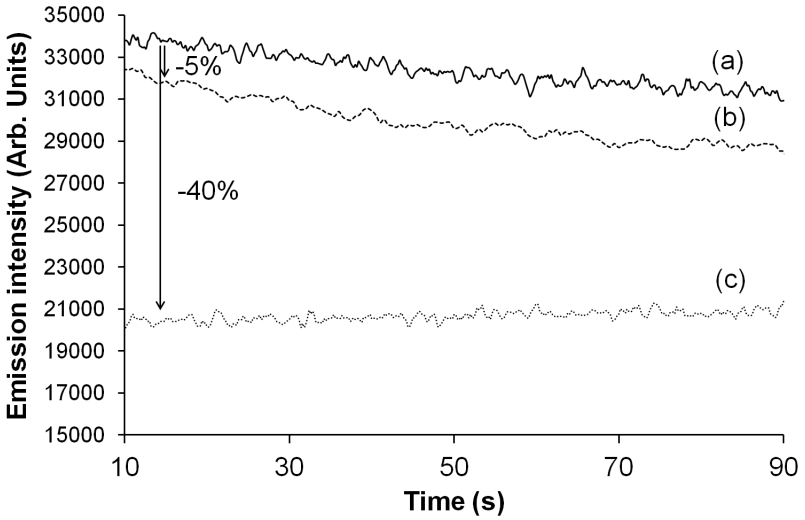

Figure 7.11: Kinetic scans of CaS:Eu^{2+} particles in ethanol (a), in TiO_2 sols prepared with method 1 (b) and 2 (c). The measurements were recorded at excitation wavelength of 400 nm and emission at 650 nm.

coating technique of CaS:Eu^{2+} with TiO_2 is explained in section 3.3.

The XRD spectrum of the CaS:Eu^{2+} particles coated with TiO_2 (1 layer) prepared using the sol with a viscosity of 6.85 mPa.s is presented in Fig. 7.12. This XRD spectrum shows that during the coating the reaction between CaS:Eu^{2+} and TiO_2 sol results in the partial degradation of CaS:Eu^{2+} to $CaCO_3$. However, we observed that after the annealing of uncoated CaS:Eu at 400°C for 30 min, CaS:Eu decomposed to $CaSO_4$:Eu (§6.3.2 and Fig. 6.8). The formation of $CaCO_3$ indicates that during the heat treatment of coated particles, the reaction between CaS:Eu and released carbonate groups from the TiO_2 layer may dominate the other reactions which may result in formation of $CaSO_4$.

Figure 7.13 shows the SEM image of the coated CaS:Eu using TiO_2 (1 layer) with viscosity of 6.85 mPa.s. After the coating a deformation on the particles' surfaces is observed. It is associated with the decomposition of the particles. The TiO_2 layer around the particles is not homogeneous in contrast to TiO_2 films (Fig. 7.9) and also it is seen in Fig. 7.13 that the TiO_2 layer is peeling from the Si substrate. These effects may be due to the large thickness of the film (thicker than 300 nm) and the presence of particles on the Si substrate surface.

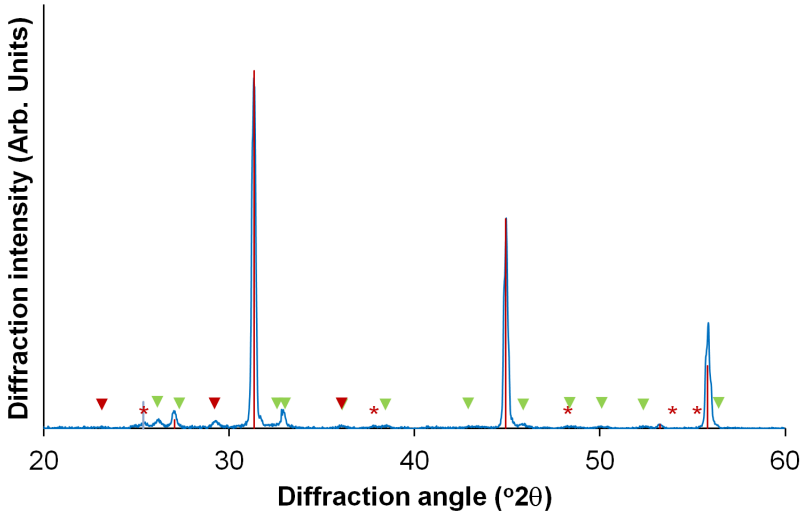

Figure 7.12: XRD spectrum of the CaS:Eu^{2+} particles coated with TiO_2 (1 layer) prepared using the sol with a viscosity of 6.85 mPa.s. Red lines represent the peak positions of CaS (data from ICDD file No 65-7852). Red stars show the peak positions of anatase TiO_2 (data from ICDD file No. 21-1272). Green and red triangles indicate aragonite $CaCO_3$ (data from ICDD file No. 41-1475) and calcite $CaCO_3$ (data from ICDD file No. 72-1937), respectively.

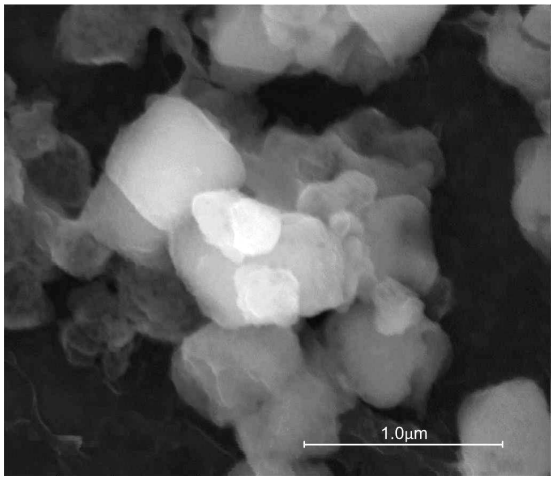

Figure 7.13: SEM image of the coated CaS:Eu using TiO_2 (1 layer) with viscosity of 6.85 mPa.s.

The PL excitation and emission spectra of uncoated (blue line) and coated (red line) CaS:Eu are shown in Fig. 7.14. TiO_2 (1 layer) with a viscosity

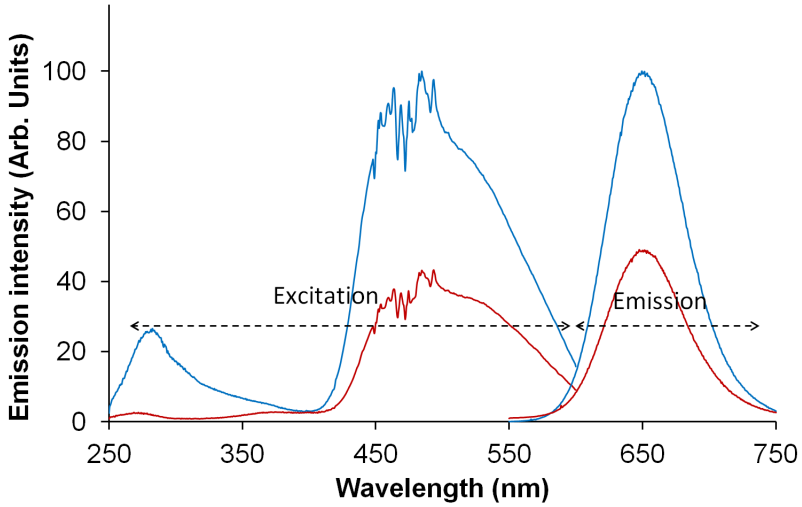

Figure 7.14: PL emission and excitation spectra of uncoated (blue line) and coated (red line) CaS:Eu using TiO_2 with a viscosity of 6.85 mPa.s. The excitation spectrum is recorded at an emission wavelength of 650 nm. The emission spectrum is recorded at an excitation wavelength of 450 nm.

of 6.85 mPa.s was used for coating. The optical band gap energy of TiO_2 is about 3.4 eV (365 nm). The excitation spectra were recorded at an emission wavelength of 650 nm. The peak at low energy side of the excitation spectrum of CaS:Eu^{2+} does not change by coating with TiO_2. However, the peak at high energy side of the excitation spectrum disappears by coating. When CaS:Eu^{2+} particles are coated with TiO_2, optical absorption of TiO_2 (at 350 nm) suppresses the high energy transition of CaS:Eu^{2+} if TiO_2 is thick enough. A dramatic decrease of the high energy side peak intensity in the excitation spectra (Fig. 7.14) indicates that CaS:Eu^{2+} particles are rather well coated with TiO_2. The emission spectrum is recorded at an excitation wavelength of 450 nm. Coated CaS:Eu^{2+} has a broad emission band at 650 nm, which is the same as that of uncoated CaS:Eu^{2+} (Fig. 7.14).

We also investigated the effect of the number of coatings. TiO_2 with a viscosity of 6.85 mPa.s was used for coating. After each coating, the coated CaS:Eu^{2+} layer was heat treated at 400°C for 30 min. The emission spectra of CaS:Eu^{2+} before and after coating are given in Fig. 7.15. The emission spectra were recorded at an excitation wavelength of 450 nm. After the first coating, the emission intensity decreases to 50% of the initial intensity. After the second coating, the emission intensity reduces to 23% of the initial intensity and after that the emission intensity does not decrease anymore.

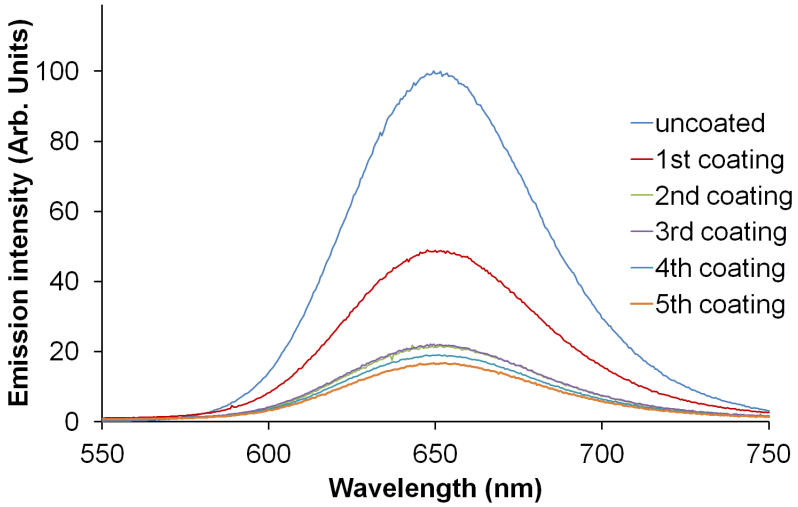

Figure 7.15: PL emission spectra of CaS:Eu^{2+} before and after coating using TiO_2 with viscosity of 6.85 mPa.s recorded at an excitation wavelength of 450 nm.

When we compare the degradation of uncoated CaS:Eu after a number of heat treatments at 400°C for 30 min (table 6.1) with CaS:Eu coated with a number of TiO_2 layers (Fig. 7.15), it can be clearly seen that coating with TiO_2 accelerates the decomposition of CaS:Eu at 400°C.

Although we observed that TiO_2 accelerates the decomposition of CaS:Eu at 400°C, we thought that maybe one layer of TiO_2 can already protect CaS:Eu against moisture. To evaluate TiO_2 as protection layer, CaS:Eu coated with 1 layer of TiO_2 with viscosity of 6.85 mPa.s was kept in a humidity chamber at 80°C and 80% RH. PL intensities of the uncoated and coated CaS:Eu layers as a function of time at 80°C and 80% RH are shown in Fig. 7.16. The figure expresses that coating TiO_2 layer does neither slow down nor prevent the degradation of CaS:Eu.

All these experiments were also done using TiO_2 with viscosity of 3.77 mPa.s, but no spectacular differences were observed.

7.6 Conclusions and perspectives

This chapter focused on the crystallization, morphology and optical properties of TiO_2 powders and thin films. In addition to that it included the

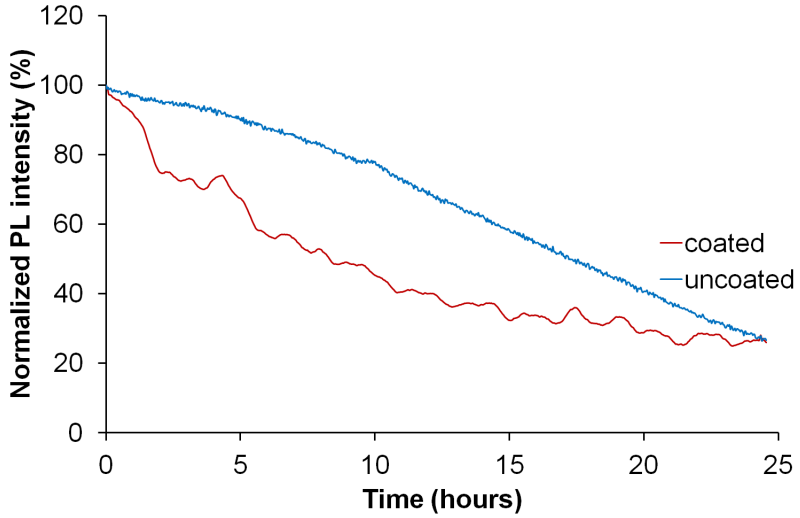

Figure 7.16: PL intensities of the uncoated sample and samples coated with TiO_2 film (1 layer) samples as a function of time at 80°C and 80% RH.

investigation of TiO_2 films as protection layer. TiO_2 bulk powder as well as TiO_2 thin films on Si and glass substrates were obtained using two non-aqueous sol-gel techniques. Powders prepared by both methods crystallize around 320°C. Anatase TiO_2 powder is obtained over a broader temperature range when using method 2. Using helium atmosphere instead of air during the heat treatment delayed the formation of the rutile phase for both methods, although it did not affect the transition temperature from amorphous to anatase. The films were homogeneous and their thickness was less than 250 nm for a single coating. By changing the heating temperature, spin speed and viscosity of the solution, films with several thicknesses and refractive indices were obtained. The crystallization of the films was similar on single crystal Si (100) and amorphous Corning 1737 glass substrates. During the examination of the performance of TiO_2 films as protection layers, we observed 50% loss in the emission intensity of the coated particles. This fact is associated with reaction between CaS and the TiO_2 layer during heat treatment. In addition to that, an accelerated aging tests at 80°C and 80% RH reveal that the TiO_2 layer does not protect particles in these conditions. It can be related to the pore structure of the TiO_2 layer. TiO_2 films are anatase at 400°C. The grain boundaries may act as shortcut for diffusion of atmospheric gases [161]. Therefore the lack of protection by TiO_2 layer may associated with this. A wettability test of the TiO_2 films revealed that films had hydrophilic surface. The bad protection feature of the TiO_2 layers may also be related to this property. Although the main purpose of all these examinations is to asses

the performance of TiO_2 as protection layer, we observed that TiO_2 prepared by both methods is not suitable for this application.

Chapter 8

Al_2O_3 thin films

8.1 Motivation

Aluminium oxide is a versatile and technologically important material because of its wide transparency window from ultra-violet to mid-infrared [6, 119, 162], good thermal and chemical stability [4, 110], and superior electrical and mechanical properties [163, 164]. Especially aluminium oxide in thin film form has a broad application range including use as water-repellent coating [114, 165], dielectric [164] and sensing layer [5] and optical [166] and protective coating [6, 15, 111, 115, 118]. These application areas make synthesis and characterization of aluminium oxide films attractive. Sol-gel is an interesting technique to synthesize aluminium oxide films, as it has several advantages over other techniques (see section 1).

In this study we synthesized Al_2O_3 thin films for use as protection layer. Al_2O_3 sols were prepared using two different non-aqueous sol-gel methods to understand the effect of the sol on the luminescent particles. Details about the preparation techniques are given in section 3.4. While a strong acid was used in the first technique, no acid was used in the second one. The optical properties of the Al_2O_3 thin films, which are prepared by method 2, were investigated. In order to observe the influence of the solvent on the optical properties of films, three different alcohols were used. In this chapter, after discussing the optical properties of Al_2O_3 thin films, we assess Al_2O_3 for protection purposes and in the end we will compare Al_2O_3 protection layers prepared by non-aqueous sol-gel and ALD techniques.

8.2 Optical and structural properties of Al_2O_3 thin films

All Al_2O_3 thin films, which are discussed in this section, were prepared with a non-aqueous sol-gel method developed in-house using anhydrous ethanol (EtOH), isopropanol (^{i}PrOH) and n-butyl alcohol (n-BuOH) (method 2).

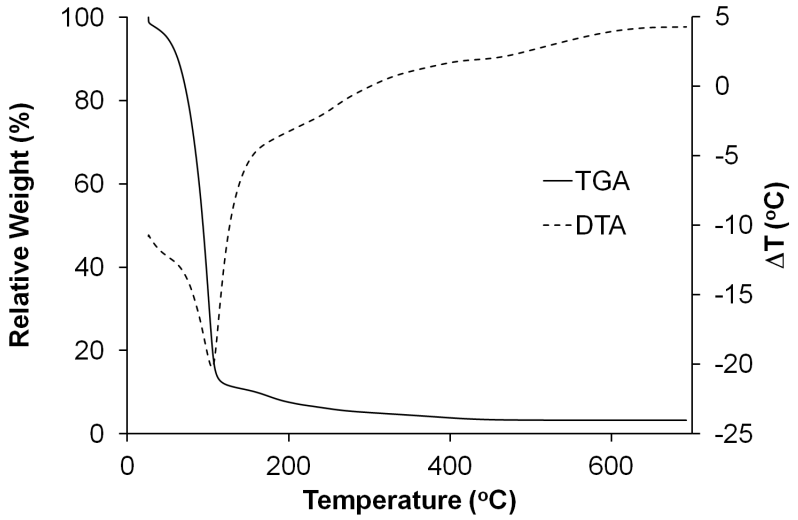

Figure 8.1: The TGA/DTA analysis of aluminium oxide sol synthesized using n-BuOH as solvent with a heating rate of 10°C/min in an air flow.

To find the optimum heat treatment temperature for amorphous aluminium oxide, TGA and DTA were performed. Since the TGA and DTA results of the three sols are quite similar, we only show them for aluminium oxide sol prepared with n-BuOH as an example (Fig. 8.1). In the TGA curves, two main weight loss stages are observed, in the range from 35 to 200°C and 200 to 500°C (Fig. 8.1). The first weight loss is around 92.4% and induced by evaporation of water and thermal decomposition of the organics. The second one is correlated with the loss of carbon groups in the structure [3] and weight loss is only 4.3%. The weight loss during the dehydroxylation is very low as compared with the weight loss during the evaporation of water and the decomposition of organics [167]. Therefore it is not entirely clear from these measurements whether hydroxides are still present after the heat treatment. Consequently, other analytical techniques, such as XPS and FTIR, were applied to evaluate whether pure alumina thin films, without hydroxides, were obtained after heat treatment.

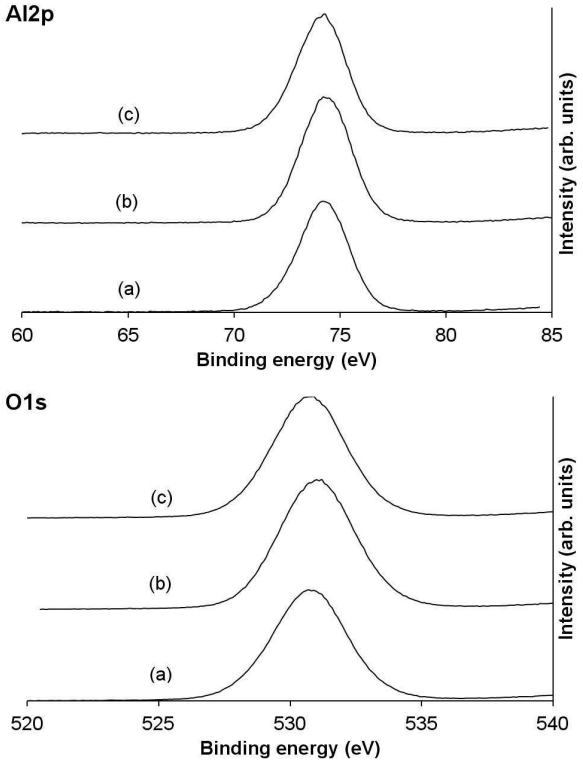

Figure 8.2: XPS spectra of Al and O in aluminium oxide thin films prepared with EtOH **(a)**, ^{i}PrOH **(b)** and n-BuOH **(c)** after heat treatment at 500°C.

For the characterization of amorphous materials x-ray diffraction techniques are not suitable. Hoewever, XPS can be useful, as information on the chemical composition and elements' binding state can be obtained. In addition to this, it can also be used to determine different phases of amorphous alumina. The binding energy of Al hardly varies (0-0.5 eV) between the different alumina phases. However, oxygen core level binding energies have a larger sensitivity to changing environments and can thus be used for phase identification [168]. If the thin films would contain more than one phase, two or more peaks and also shifting in the peak position can be expected in the O1s photo peak. Figure 8.2 shows the high resolution XPS spectra of Al2p and O1s core lines of the thin films prepared using EtOH, ^{i}PrOH and n-BuOH as solvent. The spectra were recorded after the surface of the thin films was sputtered by argon to remove the surface contaminants. All thin films for XPS analysis were coated on Si substrates and heat treated at 500°C. As seen in the figure, the peaks of Al2p and O1s are very symmetrical. This suggests

only one contribution to the peaks. Table 8.1 summarizes the results of the XPS measurements of the thin films. The peak positions and the symmetry in the O1s core lines of the samples imply that the samples only consist of an aluminium oxide phase. The peak positions and the oxygen/aluminium ratio are consistent with Al_2O_3 [118,168,169]. The reported binding energies of Al2p and O1s are at around 74.30 eV and 531.0 eV, respectively. In case of the presence of hydroxide in the films, a shoulder at around 532.3 eV in the O1s peak would be expected [118, 168, 169].

Film	Al2p (eV)	O1s (eV)	O/Al ratio
Prepared with EtOH	74.2	530.7	1.46
Prepared with ^{i}PrOH	74.2	531.2	1.50
Prepared with n-BuOH	74.3	530.9	1.53

Table 8.1: XPS results of aluminium oxide films heat treated at 500°C.

The chemical composition and bonds of the aluminium oxide thin films on double side polished silicon wafers were also analyzed by FT-IR spectroscopy. Figure 8.3 shows the FT-IR absorption spectra of the thin films before and after heat treatment at 200 and 500°C, for the three solvents.

Based on the temperature dependency, the spectra can be divided into two parts. The first part consists of the peaks at frequencies higher than 1020 cm^{-1}, and the second part comprises the peaks below 1020 cm^{-1}. As clearly seen in Fig. 3, after the heat treatment at 200°C the peaks located in the second part give place to two weak and broad peaks.

The broad peak with a maximum at 3620 cm^{-1} in Fig. 8.3 is due to the stretching mode of O – H groups [118, 170–173]. This peak disappears after a heat treatment at 500°C. This implies that after a heat treatment at 500°C neither water nor aluminium oxide hydroxide are present in the samples. This result is in line with XPS measurements. The absorption bands between 3000 and 2850 cm^{-1} result from asymmetric and symmetric stretching of aliphatic C – H bonds [169] and they disappear after heat treatment at 200°C as confirmed by TGA curves (Fig. 8.1). Two intense absorption peaks located between 1650 and 1500 cm^{-1} are assigned to C = O stretching vibration of acetylacetone and acetic acid [118, 173, 174]. There may be a contribution of the H_2O rocking vibration at 1600 cm^{-1} to the spectra. The peaks between 1500 and 1320 cm^{-1} are assigned to a mixture of C – H bending coming from carbon-hydrogen bonds in the CH_2 and CH_3 groups. C – H

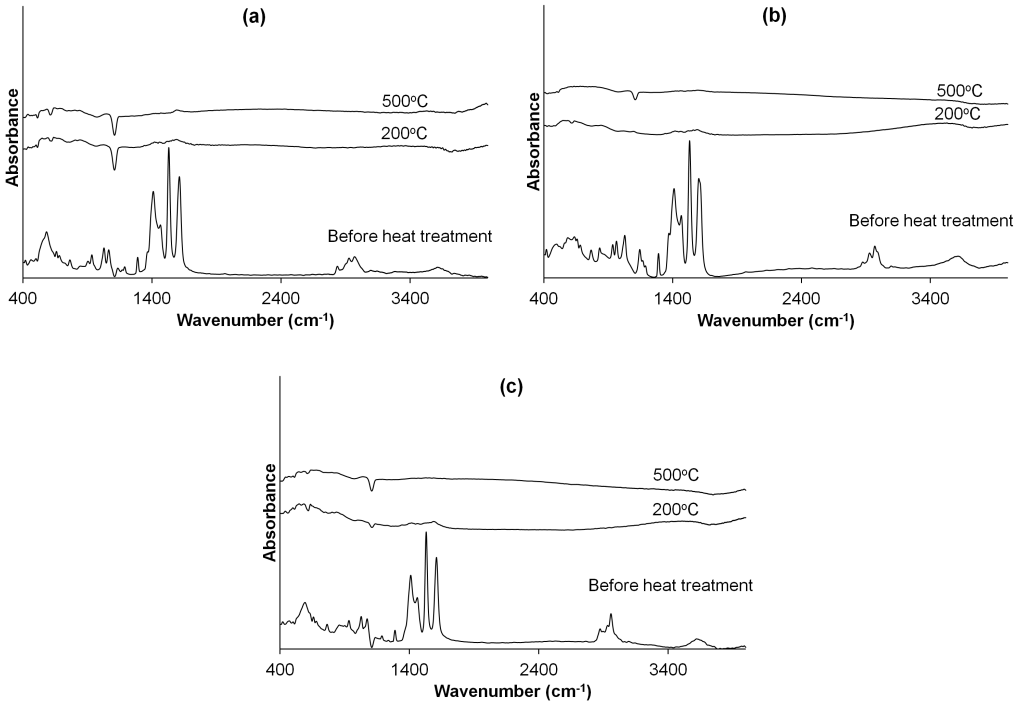

Figure 8.3: FT-IR absorption spectra of aluminium oxide films prepared with EtOH (a), ^{i}PrOH (b) and n-BuOH (c) before and after heat treatment at 200 and 500°C. For clarity, the spectra of the samples annealed at 200 and 500°C are vertically shifted.

wagging and twisting vibrations occur at 1290 cm^{-1}. The peaks between 1200 and 1120 cm^{-1} are assigned to various C – C band vibrations. Two peaks between 1120 and 1020 cm^{-1} are identified as C – O stretching bands. The broad bands located at lower frequency region (between 1000 and 400 cm^{-1}) are related to aluminium oxide [4, 175–177]. When the samples were heated at 200°C, the shape of these bands changed due to the formation of aluminium oxide or oxide hydroxide from aluminium hydroxide. In alumina, aluminium can occupy three different geometries with oxygen which are octahedral (AlO_6), pentahedral (AlO_5) (amorphous structure) and tetrahedral (AlO_4). When aluminium ions have octahedral coordination (AlO_6), the Al - O stretching and bending modes are seen in the region 500-750 cm^{-1} and 350-450 cm^{-1}, respectively. If they have tetrahedral symmetry (AlO_4), the Al - O stretching and bending modes appear in the narrow range 750-850 cm^{-1} and 250-320 cm^{-1}, respectively. The transition alumina phases consist of octahedral (AlO_6) and tetrahedral (AlO_4) geometries [4, 175, 176]. The

broad and smooth absorption band without any fine structure in the wave number range from 500 to 900 cm^{-1} characterizes the amorphous aluminium oxide [177]. As seen in Fig. 8.3, although the samples prepared with EtOH and n-BuOH after annealing at 500°C contain both octahedrally (AlO_6) and tetrahedrally (AlO_4) bound aluminium ions, in the sample prepared with ^{i}PrOH after annealing at 500°C the amorphous structure is dominant. Note that the apparent negative absorption peak at 1110 cm^{-1} is due to a difference in interstitial oxygen concentration in the Czochralski-grown Si substrates [178]. The reduction of interstitial oxygen might be explained by the formation of oxygen thermal donors [179] due to the heat treatments.

Optical constants and thicknesses of a number of films were determined via spectroscopic ellipsometry. Because of the transparency of aluminium oxide from UV to IR [6, 119, 162], the Cauchy dispersion model was used to calculate the optical constants. The optical model included surface roughness; however, it was found to be lower than 12 nm for all samples. Porosity of the films was calculated using the Bruggeman effective medium approximation (EMA) [54]. Reference data such as Cauchy coefficients and refractive index for aluminium oxide were supplied from literature (1.76 at 632.8 nm) [180].

Sample	Solvent	Spin speed (rpm)	Annealing temperature (°C)	Thickness (nm)	n @ 632.8 nm	Porosity (%)	MSE
A	EtOH	4000	450	69	1.56	26	6.80
B	^{i}PrOH	4000	450	82	1.55	27	8.99
C	n-BuOH	4000	450	55	1.57	25	7.20
D	EtOH	4000	650	48	1.54	28	4.87
E	^{i}PrOH	4000	650	75	1.54	29	10.55
F	n-BuOH	4000	650	51	1.54	29	5.05
G	EtOH	6000	450	59	1.58	24	6.43
H	^{i}PrOH	6000	450	70	1.57	25	7.83
I	n-BuOH	6000	450	47	1.60	22	7.10

Table 8.2: Spectroscopic ellipsometry results of aluminium oxide films.

Table 8.2 summarizes the results from the spectroscopic ellipsometry analysis on aluminium oxide thin films. The effect of the solvent on the film properties was studied by preparing thin films with different solvent but using the same conditions. When the samples heat treated at 450°C are compared (A, B and C and G, H, and I), changing alcohol from ^{i}PrOH to EtOH and n-BuOH decreases the thickness of films by 16 and 33%, respectively. When D, E,

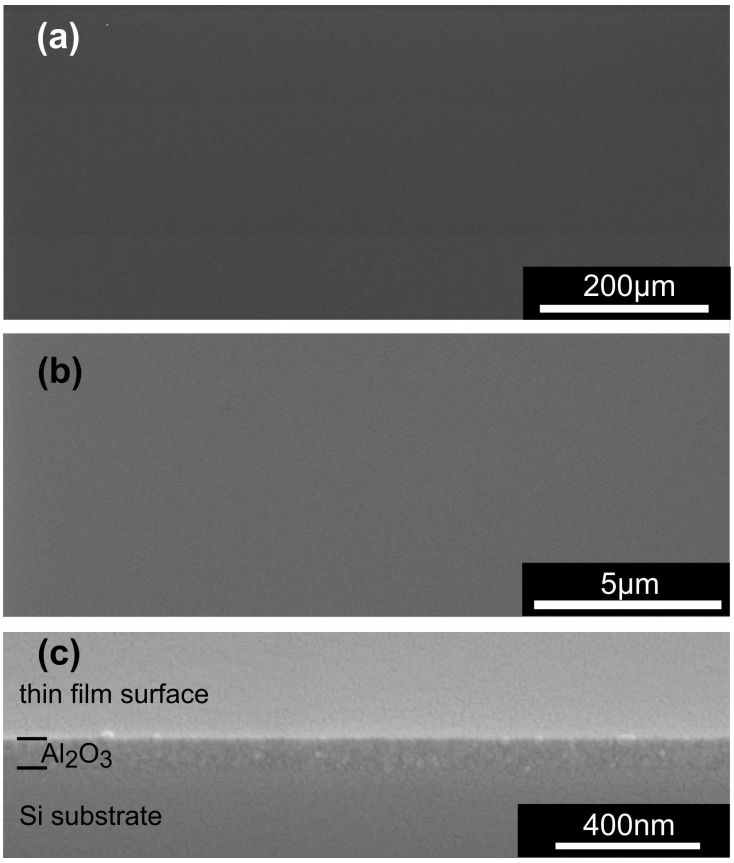

Figure 8.4: SEM image of an aluminium oxide thin film prepared with EtOH and heat treated at 500°C. **(a)** and **(b)** top view of the sample, **(c)** cross-section of the sample, observed at a grazing angle of 15°.

and F (heat treated at 650°C) are compared, changing alcohol from ^{i}PrOH to EtOH and n-BuOH results in a thickness decrease of 36 and 32%, respectively. Because of the different sizes, polarities and also evaporation rates of the solvents, they present different behaviours during hydrolysis and condensation. Although substitution of the alcohols has an effect on the thickness, it does not have noteworthy effects on the porosity and consequently also not on the refractive index. Increasing the heating temperature from 450 to 650°C results in a significant decrease of the thickness of the film prepared with EtOH and a small increase of the porosity in all samples. A decrease in the film thickness with an increase in heating temperature can be expected due to the densification of the film. Because of dehydroxylation during the heat treatment, removing OH groups leaves behind pores in the film and an increase in the porosity has been observed. The effect of the spin speed on

thickness and refractive index was also investigated (e.g., A, B, C and G, H, I). When the spin speed is increased, a thinner film is obtained with the same refractive index.

The surface properties of the films were investigated via SEM and the films prepared with the three solvents had similar surface properties, all of them homogeneous and crack free. As an example, SEM images of the thin film prepared with ethanol and spin coated at 2000 rpm then heat treated at 500°C are presented in Fig. 8.4.

8.3 Al_2O_3 as a protection layer

8.3.1 Al_2O_3 prepared with sol-gel

As we have shown in section 6.3, the presence of water causes decomposition of CaS:Eu particles. In section 7.5, degradation of CaS:Eu particles was observed when they were immersed in TiO_2 sols (Fig. 7.11). Even the presence of tiny amounts of water results in a drastic decrease in emission intensity which indicates degradation of particles (Fig. 7.11). In this section we go further and use a strong acid (HNO_3) to prepare Al_2O_3 sols (method 1). The PL emission intensities at 650 nm of CaS:Eu^{2+} particles in ethanol and in Al_2O_3 sol prepared with method 1 were recorded as a function of time (Fig. 8.5). Measurements were recorded at an excitation wavelength of 450 nm. As clearly seen in the figure, the PL emission intensity drops to 80% of the initial intensity immediately after the particles are added into the Al_2O_3 sol. After only 70 seconds, no more than 7% of the initial intensity is measured. Clearly a very fast degradation of CaS:Eu is associated with the presence of a strong acid and water in the Al_2O_3 sol. These measurements reveal that an excess amount of water or strong acid used for Al_2O_3 synthesis can lead to decomposition during the encapsulation process instead of protection. Therefore Al_2O_3 synthesized using method 1 was not used as protection layer.

After showing the detrimental effect of strong acid and water on CaS:Eu particles, in the remainder of this chapter we will limit the discussion to Al_2O_3 protection layers prepared with method 2. In the previous section, we have already shown the optical properties of the Al_2O_3 layers synthesized using EtOH, ^{i}PrOH and n-BuOH. However, we tested only Al_2O_3 layers synthesized using n-BuOH as protection coating, since this Al_2O_3 sol is the most stable one (§3.4).

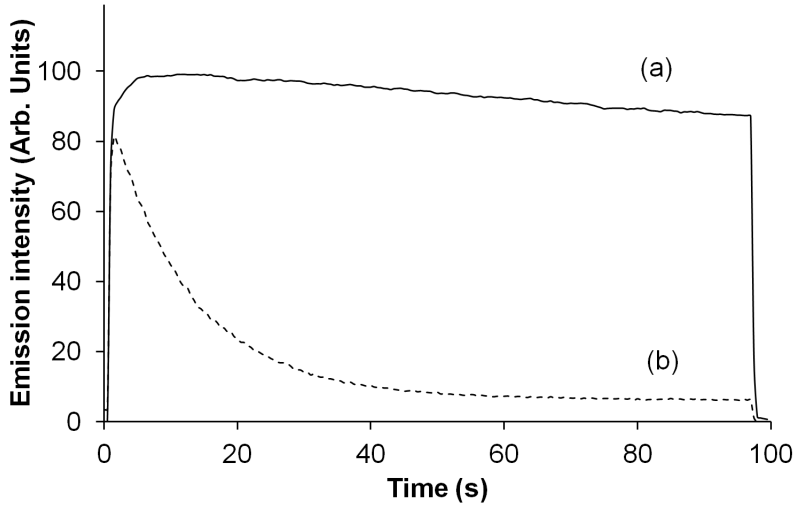

Figure 8.5: Kinetic scans of $CaS:Eu^{2+}$ particles suspension in ethanol (a), in Al_2O_3 sol prepared with method 1 (b). The measurements were recorded at excitation wavelength of 400 nm and emission at 650 nm.

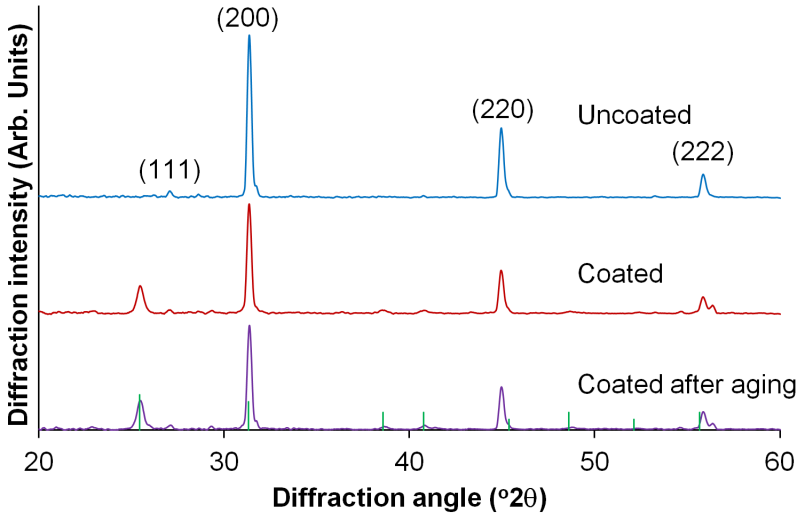

Figure 8.6: XRD spectra of the uncoated $CaS:Eu^{2+}$ particles (blue line), the $CaS:Eu^{2+}$ particles coated with alumina film before (red line) and the coated $CaS:Eu^{2+}$ particles after (purple line) 100 h of accelerated aging (80°C and 80% relative humidity). The lattice planes of CaS (data from ICDD file No. 65-7852) are indicated. Green lines represent the peak positions and diffraction intensities of $CaSO_4$ (data from ICDD file No. 37-0184).

The XRD spectra of uncoated and coated CaS:Eu^{2+} particles before and after 100 h of accelerated aging (80°C and 80% relative humidity) are presented in Fig. 8.6. The intensity of the (200) diffraction peak of CaS reduced to 70% after coating and it remained the same after 100 h of accelerated aging. In contrast to TiO_2, coating with Al_2O_3 causes the decomposition of CaS to $CaSO_4$. The decomposition of CaS to $CaSO_4$ during heat treatment at 500°C for 30 min was also observed (§6.3.2 and Fig. 6.8). After the aging, the diffraction pattern remained the same as after the coating (Fig. 8.6). This emphasizes that the alumina layer hinders the oxidation of CaS particles during aging.

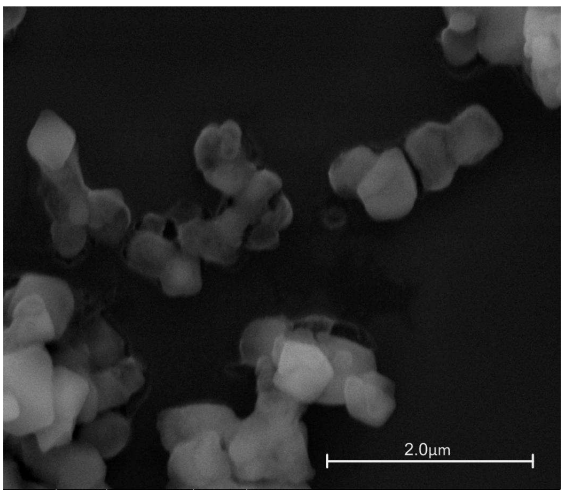

Figure 8.7: SEM image of the coated CaS:Eu with Al_2O_3 (1 layer).

Figure 8.7 shows the SEM image of the CaS:Eu coated with Al_2O_3 (1 layer). After coating, slight deformation of the particles' surfaces is observed. It is associated with the decomposition of the particles. The Al_2O_3 layer is quite homogeneous except for cracks around the particles.

The PL excitation and emission spectra of CaS:Eu^{2+} before (blue lines) and after (red lines) coating are shown in Fig. 8.8. The excitation and emission spectra were recorded at an emission wavelength of 650 nm and at an excitation wavelength of 450 nm, respectively. In addition to the blue shifting at higher energy side in the excitation spectra after coating, there is a decrease in the intensity of the excitation peak at lower energy side. The high energy side excitation band between 250 and 300 nm is a combination of the CaS band gap transition and the excitation to the $4f^6 5d$ (e_g) state in Eu^{2+}. These facts imply that the phosphor particles become smaller through decomposi-

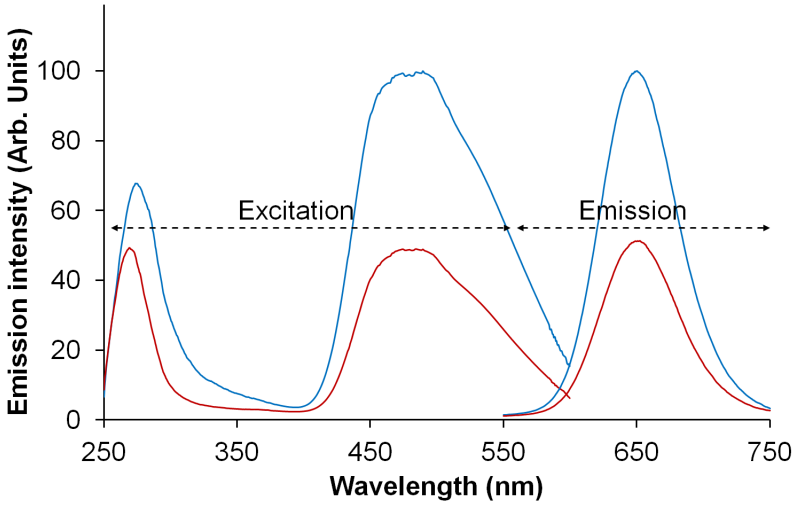

Figure 8.8: PL emission and excitation spectra of uncoated (blue line) and coated (red line) CaS:Eu using Al_2O_3. The excitation spectrum is recorded at an emission wavelength of 650 nm. The emission spectrum is recorded at an excitation wavelength of 450 nm.

tion, and the direct excitation probability of Eu^{2+} is getting decreased. This results in a relative increase of the intensity of the excitation peak from the CaS band gap, which is observed as a shift of the high energy side band in the excitation spectrum of CaS:Eu^{2+} [7]. Although water was not used for the synthesis of the alumina sol, water was produced by the condensation reaction and this may be the reason for the partial decomposition of CaS:Eu^{2+}. The intensity of the emission peak at 650 nm (Fig. 8.8) reduces to half after coating nevertheless there is no shift or deformation in the peak.

When the emission spectra of heat treated uncoated CaS:Eu^{2+} particles (Fig. 6.6) and coated particles (Fig. 8.8) are compared, it can be seen that the emission intensity of uncoated particles decreases to 20% although the coated particles which were heat treated at the same temperature as the uncoated one, show only a decrease to 50%. This highlights that the alumina layer prevents the particle from decomposition during the heat treatment.

Figure 8.9 shows the PL emission spectra of uncoated (blue line) and coated (red line) CaS:Eu^{2+} at an excitation wavelength of 275 nm. A small peak at 385 nm was observed after coating (red line, Fig. 8.9), this peak is an evidence of a small amount of $CaSO_4$:Eu^{2+} in the phosphor. However, the peak at 650 nm does not change with coating, it indicates that there is no

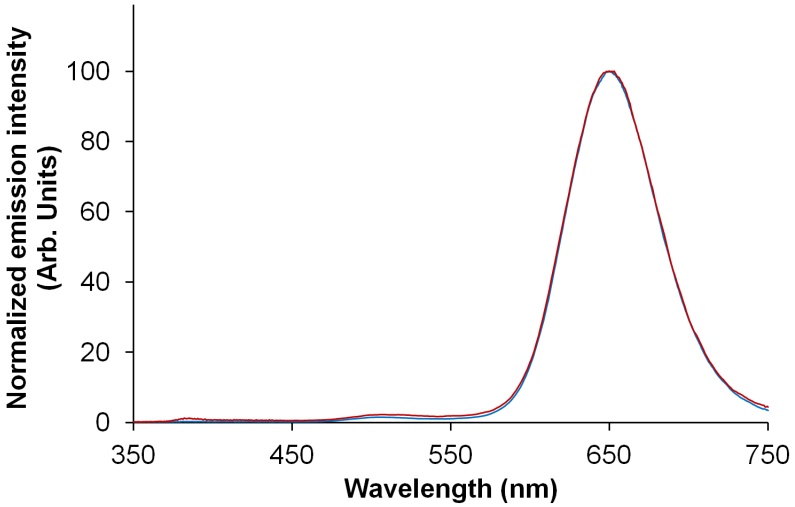

Figure 8.9: PL emission spectra of uncoated (blue line) and coated (red line) CaS:Eu^{2+} recorded at an excitation wavelength of 275 nm.

$CaSO_4$:Eu^{3+} in the phosphor after coating with Al_2O_3.

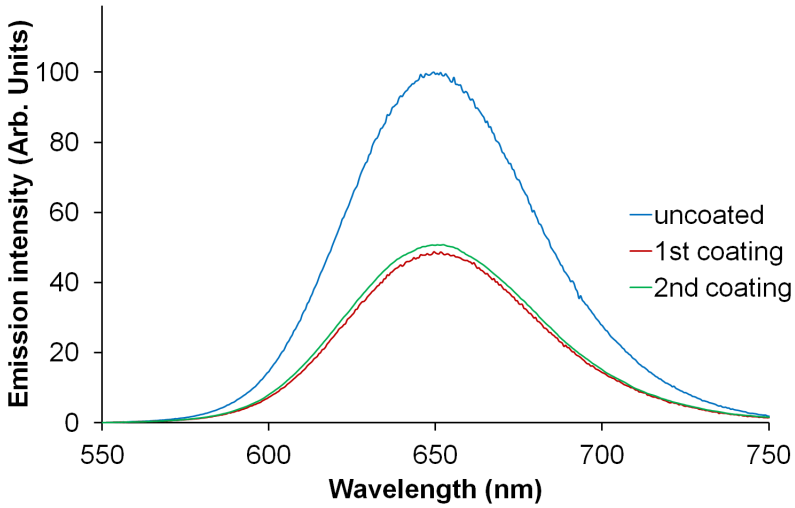

Figure 8.10: PL emission spectra of CaS:Eu^{2+} before and after coating using Al_2O_3 recorded at an excitation wavelength of 450 nm.

The effect of a second layer was also investigated. After every coating, the coated CaS:Eu^{2+} layer was heat treated again at 500°C for 30 min. The emission spectra of CaS:Eu^{2+} before and after coating are given in Fig. 8.10.

The emission spectra were recorded at an excitation wavelength of 450 nm. After the first coating, the emission intensity decreases to 50% of the initial PL emission intensity at 650 nm. After the second coating, there is no change in the emission intensity. It emphasizes that only one layer of Al_2O_3 is enough to protect CaS:Eu^{2+} at high temperatures.

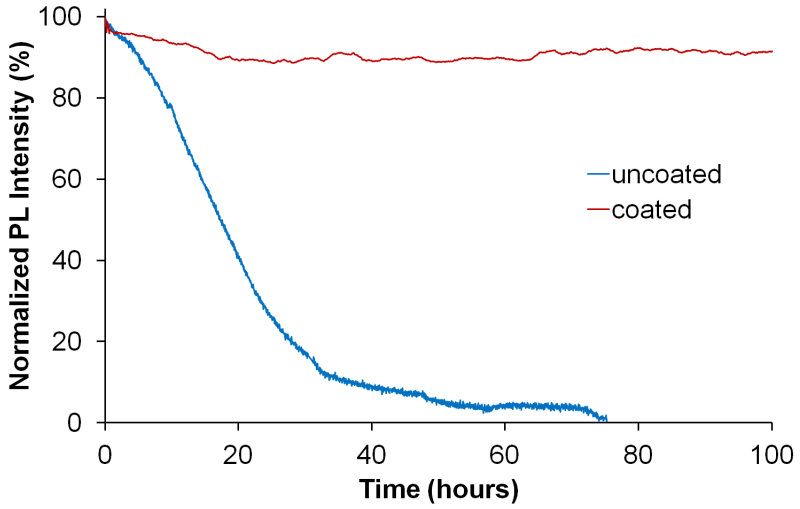

Figure 8.11: PL intensity of uncoated (blue line) sample and sample coated with an alumina film (red line) as a function of time at 80°C and 80% relative humidity.

Figure 8.11 shows the in situ measurement of the photoluminescence intensity during accelerated aging of the uncoated and coated samples at 80°C and 80% relative humidity. The blue line represents the degradation of an uncoated sample and the red line is related to the degradation of samples coated with an alumina layer. As seen in Fig. 8.11, during the first 30 h the PL emission of uncoated CaS:Eu^{2+} almost entirely disappears. After 75 h, the PL intensity of the uncoated phosphor was not detectable anymore, while the PL intensity of the coated sample was still around 95% of its initial value.

8.3.2 Al_2O_3 prepared with ALD

Al_2O_3 prepared using atomic layer deposition (ALD) was used as protection layer to compare with Al_2O_3 prepared using the sol-gel method. The preparation procedure is given in section 3.7.

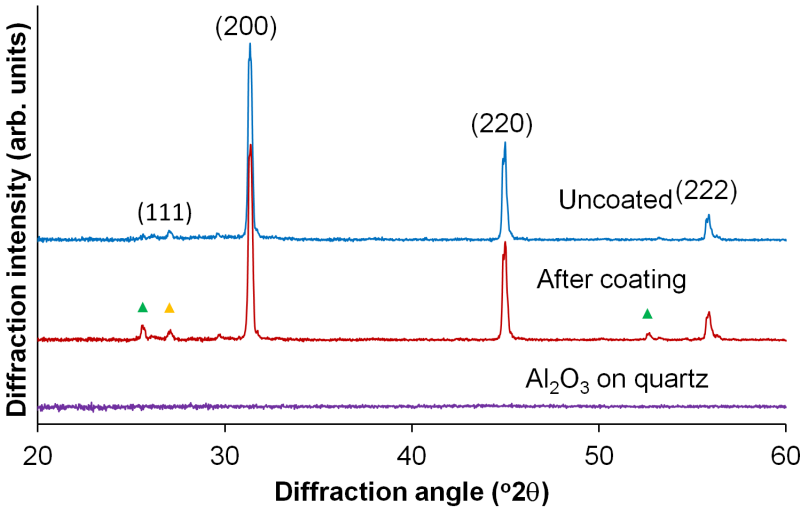

Figure 8.12: XRD spectra of a 100 nm thick aluminum oxide film deposited by ALD on a quartz substrate, of the uncoated CaS:Eu particles, and the 20 nm thick aluminum oxide ALD coated CaS:Eu. The lattice planes of CaS (data from ICDD file no. 65-7852) are indicated. The orange triangle represents the position of the most intense peak of $CaCO_3$ (data from ICDD file no. 72-0506). Green triangles indicate the peak positions of $CaSO_4 \cdot 0.64H_2O$ (data from ICDD file no. 36-0617).

Figure 8.12 presents the XRD results of the uncoated CaS:Eu particles and after coating with a 20 nm thick ALD aluminum oxide film. The intensity and the position of the CaS peaks remained the same after coating although traces of partially hydrated $CaSO_4$ were observed. The sulfate formation probably originated from the reaction of the CaS phosphor with water used as a reactive gas in the ALD coating process. This indicates that the CaS:Eu particles are essentially unaffected by the coating. There are no traces of aluminum oxide on the XRD pattern after coating because the deposition temperature is too low to obtain crystallized aluminum oxide [47, 110]. The absence of XRD peaks was confirmed on a 100 nm thick Al_2O_3 thin film deposited directly on a quartz substrate (Fig. 8.12).

The PL excitation spectra of the coated (20 nm Al_2O_3) and uncoated CaS:Eu samples are presented in Fig. 8.13. Measurements were carried out at room temperature and probed at an emission wavelength of 650 nm. As shown in Fig. 8.13, the aluminum oxide layer has a negligible influence on the excitation spectra due to the large band gap of Al_2O_3. Figure 8.13 shows also the PL emission spectrum of the uncoated (blue line) and aluminum oxide

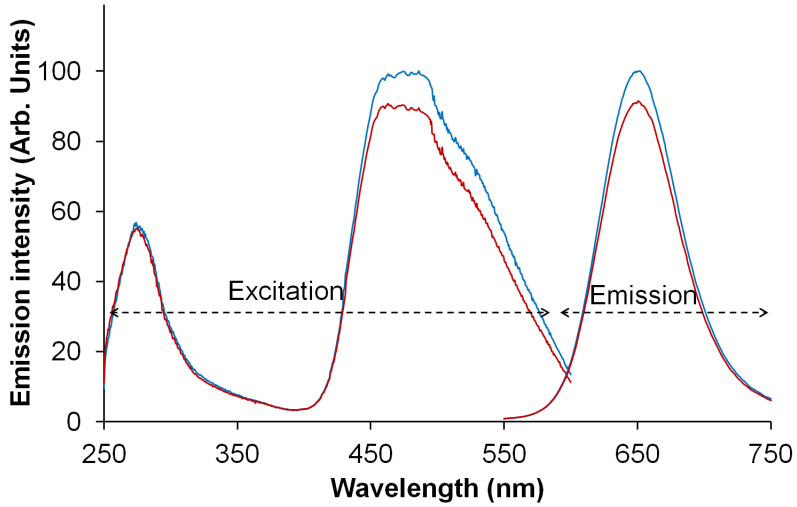

Figure 8.13: PL excitation and emission spectra of (red lines) ALD coated and (blue lines) uncoated CaS:Eu recorded at an emission wavelength of 650 nm and at an excitation wavelengths of 450 nm, respectively.

coated (20 nm) (red line) phosphor layers. Measurements were carried out at room temperature at an excitation wavelength of 450 nm. As clearly shown in Fig. 8.13, there is no shift in the emission spectra after the coating, and there is no significant difference between the PL intensity of the coated and uncoated samples. This emphasizes that there is no formation of other luminescent centers nor defect luminescence. The PL emission and excitation spectra of the uncoated and coated samples suggest that coating with a 20 nm thick aluminum oxide layer via ALD does not affect the PL properties of the sample.

In the decomposition of CaS:Eu to $CaSO_4$:Eu, an emission peak at 385 nm is expected [75–78]. The PL emission spectrum of the uncoated (blue line) and 20 nm thick aluminum oxide layer coated (red lines) phosphor layers at an excitation wavelength of 275 nm and room temperature is presented in Fig. 8.14. Although after the coating there is a trace of $CaSO_4$ in the XRD spectra (Fig. 8.12), the fraction of the decomposition of CaS:Eu to $CaSO_4$ may be too low to affect the emission spectrum (Fig. 8.14).

Figure 8.15 shows the SEM images of the CaS phosphor layer before (a) and after (b) coating with a 20 nm thick aluminum oxide film. As seen in the figure, the coated phosphor surface is smooth and clean. The elemental composition of the surface region of the uncoated and coated samples was ex-

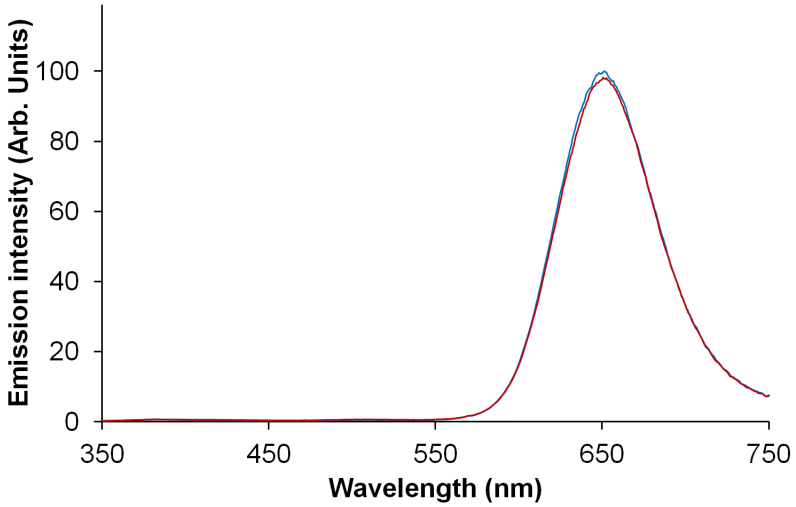

Figure 8.14: PL emission spectra of (red lines) ALD coated and (blue lines) uncoated CaS:Eu recorded at an excitation wavelengths of 275 nm.

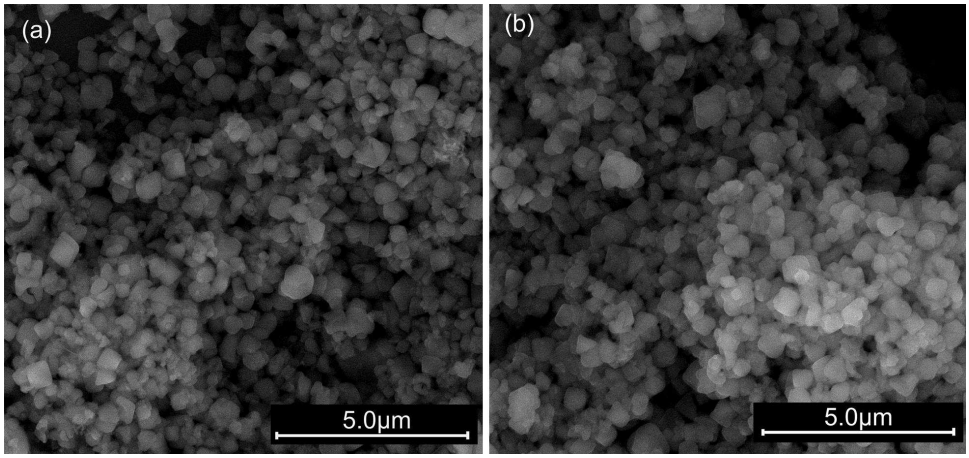

Figure 8.15: SEM images of (a) uncoated and (b) aluminum oxide ALD coated (20 nm) CaS:Eu particles.

amined with EDX. The EDX results show that the ratio between the atomic concentration of S and Ca is the same before and after coating, indicating that no major loss of sulfur (due to the release of H_2S) occurs during the coating process. The concentration of Ca and S does not drop to zero upon full coverage of the particles with aluminum oxide because of the large information depth of EDX compared to the oxide film thickness.

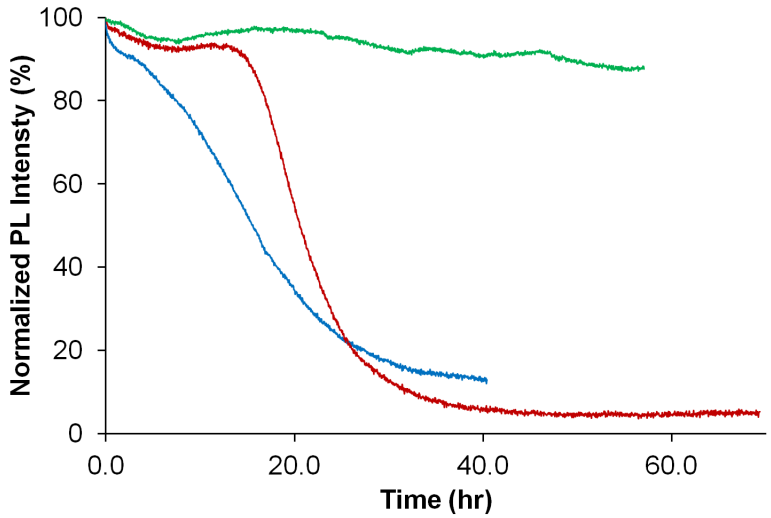

Figure 8.16: PL intensities of the (blue line) uncoated and coated samples with (red line) 10 and (green line) 20 nm thick aluminum oxide film samples as a function of time at 80°C and 80% RH.

XRD, PL emission and excitation spectra, and SEM and EDX analysis indicate that coating with aluminum oxide by the ALD technique does not create luminescent centers nor does it change the composition of the host material (CaS). We then focused on the protective properties of the aluminum oxide layer on the CaS:Eu phosphor layers against moisture. Figure 8.16 shows the in situ measurement of the PL intensity during accelerated aging of the uncoated and coated samples at 80°C and 80% RH. The blue line represents the degradation of an uncoated sample, and red and green lines are related to the degradation of samples coated with 10 and 20 nm thick aluminum oxides, respectively. As shown in Fig. 8.16, the PL intensity of the uncoated CaS:Eu has dropped to around 35% after 20 h, and the normalized PL intensities of the samples coated with 10 and 20 nm thick layers are around 55 and 95% relative to the starting PL intensity. While the normalized PL intensities of the uncoated and 10 nm thick film-coated samples reduce to 10 and 5%, respectively, the normalized PL intensity of a sample coated with 20 nm Al_2O_3 is still around 90% after 40 h. Clearly, a thickness of 10 nm is insufficient for long-term protection of the CaS phosphor layer. Even after 57 h, the PL normalized intensity of a sample coated with a 20 nm thick film is around 85%. Therefore, we have obtained a conformal aluminum oxide coating on the particles, which is a distinct advantage of ALD techniques over physical vapor deposition techniques. The latter only offer line-of-sight deposition and do not enable protection of the particles homogeneously on

all sides [181, 182].

8.4 Conclusions and perspectives

In the first year of this research, degradation of CaS:Eu particles in Al_2O_3 solution synthesized by a strong acid and a little bit of water was studied. The PL emission of particles in Al_2O_3 solution is not detectable after 80 seconds. This experiment underlines how important the used chemicals are for the preparation of a protection layer. It also shows that the protection procedure can end up with completely decomposed particles depending on the solution like in the case of Al_2O_3 prepared with the first method. Therefore we looked for another method to prepare Al_2O_3 for protection layer and we synthesized Al_2O_3 sols using a non-aqueous sol-gel method (method 2).

In the first part of this chapter, optical and structural properties of the aluminium oxide thin films prepared with method 2 were dealt with. These thin films were prepared using alumina solutions synthesized using three alcohols (EtOH, ^{i}PrOH and n-BuOH). Although all solutions were stable for at least 1 month, the most stable solution was obtained using n-BuOH. Aluminium oxide thin films prepared using these three solutions were amorphous, crack free and have similar properties. After heat treatment of films at 500°C, amorphous aluminium oxide films were obtained. Different film thicknesses from 50 to 160 nm with the same refractive index can be obtained by changing the preparation parameters such as spin speed and solvent.

The phosphor layers were coated with alumina prepared via a non-aqueous sol-gel technique (method 2) to improve their stability. Aluminium oxide sol prepared with n-BuOH was used for this purpose. The experimental results show that an alumina film strongly enhances the resistance of the phosphor layer against moisture and high temperature in spite of the partial degradation of the sample surface during the coating process. We also coated moisture sensitive CaS:Eu particles using ALD aluminium oxide. Unlike the sol-gel technique it does not require a post-deposition heat treatment of the particles. Therefore degradation of the particles during the coating process was almost negligible. Taking this into account, in combination with the excellent resistance against moisture of both the ALD and sol-gel coated particles, ALD is the better technique to prepare a protection layer for sulfides as it gives a higher luminescence efficiency. A disadvantage is it being more expensive as coating technique compared to sol-gel techniques. Hence, sol-gel based inorganic coatings seem an interesting route for the protection of

luminescent sulfides, on condition that the degradation during the necessary heat treatment can be reduced.

Chapter 9

$CaAl_2O_4$:Eu^{2+},Nd^{3+} powders

9.1 Motivation

$CaAl_2O_4$ is the most widely used member of the alkaline earth aluminates MAl_2O_4 (M= Ca, Sr and Ba) [126, 183]. It is commonly used as cement in very different areas from construction to dental applications [125–127]. In addition to this, $CaAl_2O_4$ doped with Eu^{2+} and R^{3+} (R: rare earth) shows bright violet afterglow luminescence [19]. To prepare it different kinds of techniques have been used such as solid state reaction, co-precipitation, microwave, Pechini, combustion and sol-gel synthesis [129, 130, 133, 140, 143–147]. Comparing these methods, sol-gel synthesis possesses some benefits, namely, relatively low preparation temperature, easy control of the stoichiometry, no need for expensive equipments and high homogeneity.

$CaAl_2O_4$:Eu,Nd luminescent powders were prepared using sol-gel synthesis. These powders were prepared in three stages via a non-aqueous sol-gel method and the order of the sections in this chapter will be arranged according to the consecutive preparation stages. First we focus on the optimum synthesis temperature determination, and then the influence of the europium concentration is studied. After the comparison of two methods to reduce Eu^{3+} to Eu^{2+}, finally, the persistent luminescence characteristics of $CaAl_2O_4$:Eu,Nd prepared by non-aqueous sol-gel technique will be presented.

9.2 $CaAl_2O_4$:Eu

9.2.1 Optimum annealing temperature

In previous investigations it was suggested that the strongest luminescence in $CaAl_2O_4$ is obtained for the monoclinic phase [135]. Janáková et al. reported the start of the transition from the hexagonal phase to the monoclinic phase at 1050°C (for a dwell time of one hour). Higher temperatures or longer heating times were required to have a full conversion like at 1150°C for 8 hours [137]. We have prepared $CaAl_2O_4$ using a non-aqueous sol-gel method. The preparation procedure was explained in section 3.5 and involves $Ca(NO_3)_2.4H_2O$ and aluminium sec-butoxide ($Al[O(CH_3)CHC_2H_5]_3$) as precursor, n-butyl alcohol (n-BuOH) as solvent and acetylacetone (AcAcH) as chelating agent.

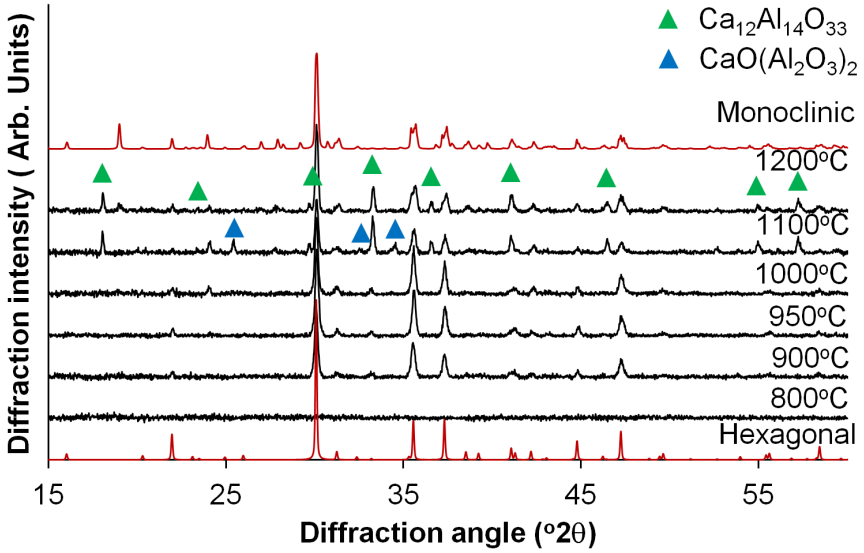

Figure 9.1: XRD spectra of undoped $CaAl_2O_4$ sols heat treated at various temperatures. The red lines indicate reference spectrum for monoclinic (data from ICDD file no. 70-0134) and hexagonal $CaAl_2O_4$ which is based on [137]. The green triangles represent the peak positions of$Ca_{12}Al_{14}O_{33}$ (data from ICDD file no. 09-0413) and blue triangles indicate the peak positions of $CaO(Al_2O_3)_2$ (data from ICDD file no. 89-3851).

The X-ray diffraction (XRD) spectra of undoped $CaAl_2O_4$ annealed at various temperatures are shown in Fig. 9.1. As seen in the figure, XRD spectra of hexagonal and monoclinic $CaAl_2O_4$ are very similar. We used the splitting

of the diffraction peak at 35.5° (2θ) to identify the main phase (presence of splitting indicates monoclinic phase). This figure reveals that the formation of the hexagonal phase begins at 900°C. At 1100°C, the phase transition to the monoclinic $CaAl_2O_4$ phase sets in. For 1100°C or higher, some minority phases are observed as well.

As mentioned in the literature review of $CaAl_2O_4$ (§5.6), europium can be trivalent (Eu^{3+}), divalent (Eu^{2+}), or both of them together in $CaAl_2O_4$ [135, 137, 144]. In order to identify the oxidation state of europium in $CaAl_2O_4$, two different excitation wavelengths are used namely, 260 and 330 nm, as in this way Eu^{3+} and Eu^{2+} are preferentially excited, respectively.

The excitation spectra of $CaAl_2O_4$:Eu (1%) annealed at 900 (blue line), 1000 (red line) and 1100°C (green line) are shown in Fig. 9.2a. The excitation spectra are recorded at an emission wavelength of 616 nm. The broad excitation bands located at the higher energy side of the spectra originate from the Eu^{3+}-O^{2-} charge-transfer transition while the narrow peaks are associated with the transitions within the $4f^6$ electronic configuration [21, 137]. Figure 9.2b indicates the emission spectra of $CaAl_2O_4$:Eu (1%) annealed at 900 (blue line), 1000 (red line) and 1100°C (green line), and they were recorded at an excitation wavelength of 260 nm. The spectra are divided into five regions. In the first region, the peak with a maximum at around 578 nm is related to the $^5D_0$ to $^7F_0$ transition and the other peaks are associated with $^5D_0$ to $^7F_1$ transitions. The transitions from $^5D_0$ to $^7F_2$, $^7F_3$, and $^7F_4$ states in Eu^{3+} are associated with the peaks located in the region (II),(III) and (IV), respectively [27]. The presence of two kinds of transitions ΔJ=1 (magnetic-dipole) and ΔJ=2 (electric-dipole) suggests at least two different crystallographic sites occupied by Eu^{3+} [137]. Two very small peaks at around 535 and 555 nm may be related to the transition from $^5D_1$ to $^7F_1$ and $^7F_2$ states in Eu^{3+}, respectively. There is a very weak peak at 440 nm in the emission spectra, this peak is related to the $5d4f^6$-$4f^7$ transition of Eu^{2+} (region (V)). The intensity of the spectra does not change with the annealing temperature except for the first peak in the region (II). An increase in this peak intensity is observed after annealing at 1100°C. Therefore, this change may related the formation of a new phase in $CaAl_2O_4$:Eu powder (Fig. 9.1). When we compare these excitation and emission spectrum with the excitation and emission spectrum in Janáková's report [137], we can clearly see that the spectra in figure 9.2 are identical to the ones for monoclinic $CaAl_2O_4$:Eu^{3+} in Janáková's report (Fig. 5.6).

The excitation and emission spectra of $CaAl_2O_4$:Eu (1%) annealed at 900

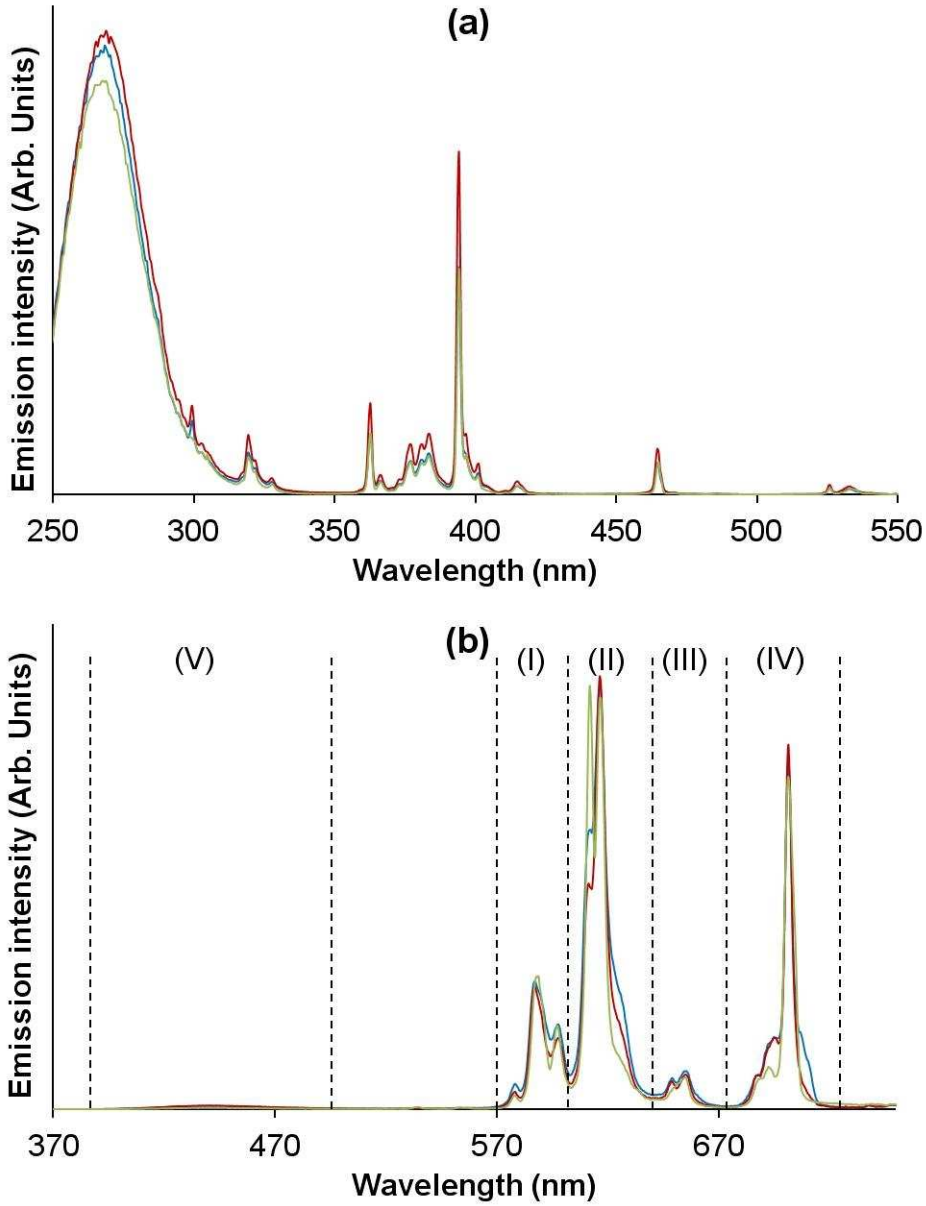

Figure 9.2: PL excitation (a) and emission (b) spectra of $CaAl_2O_4$:Eu (1%) annealed at 900 (blue line), 1000 (red line) and 1100°C (green line). The excitation and emission spectra are recorded at an emission wavelength of 616 nm and an excitation wavelength of 260 nm, respectively. The regions from (I) to (V) are explained in the text.

(blue line), 1000 (red line) and 1100°C (green line) are presented in Fig. 9.3. The excitation spectra are recorded at an emission wavelength of 440

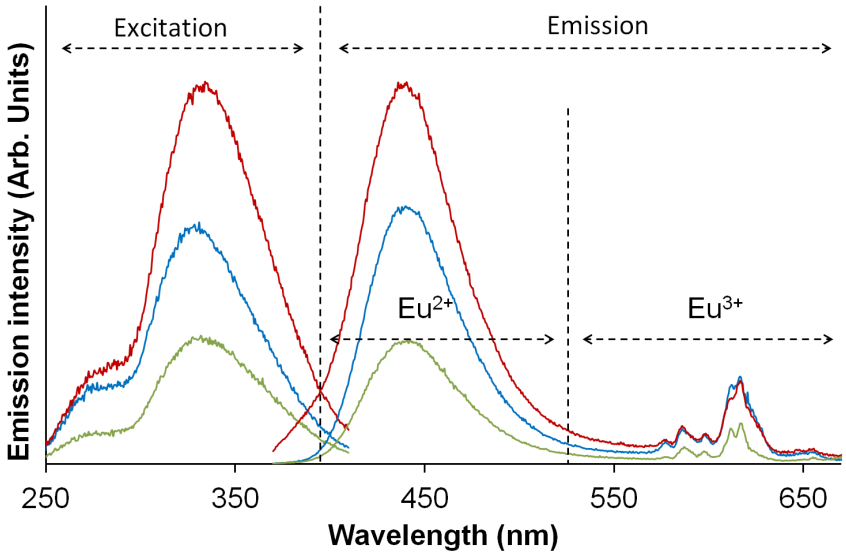

Figure 9.3: PL excitation and emission spectra of $CaAl_2O_4$:Eu (1%) annealed at 900 (blue line), 1000 (red line) and 1100°C (green line). The excitation and emission spectra are recorded at an emission wavelength of 440 nm and an excitation wavelength of 330 nm, respectively.

nm and an excitation wavelength of 330 nm, respectively. There are two excitation peaks at 255 nm and 330 nm in the spectra. They are due to transitions from the $4f^7$ ground state to the crystal field split excited levels of the $4f^65d$ state of Eu^{2+} ions [144]. As seen in the figure, we can divide the emission spectra into two regions. The high energy side is related to divalent europium emission (transition from $4f^65d^1$ excited state to $4f^7$ ground state) while the lower energy side is related to trivalent europium emission which is explained above (Fig. 9.2b). The emission properties of Eu^{2+} are easily affected by the environment, in contrast to those of Eu^{3+}. Therefore, if there is a little change in the structure of $CaAl_2O_4$ with annealing temperature, this change is likely to be reflected in the emission spectrum of Eu^{2+}. As observed in Fig. 9.3, the Eu^{2+} emission spectrum is similar for all annealing temperatures with maximum at 440 nm (characteristic peak position for monoclinic $CaAl_2O_4$:Eu^{2+} [130, 135, 136]), apart from an additional shoulder around 390 nm for the higher temperature, again pointing at the formation of impurity phases. The photoluminescence measurements reveal that the optimum annealing temperature is 1000°C although crystalline $CaAl_2O_4$ can be obtained at 900°C.

9.2.2 Influence of the Eu concentration

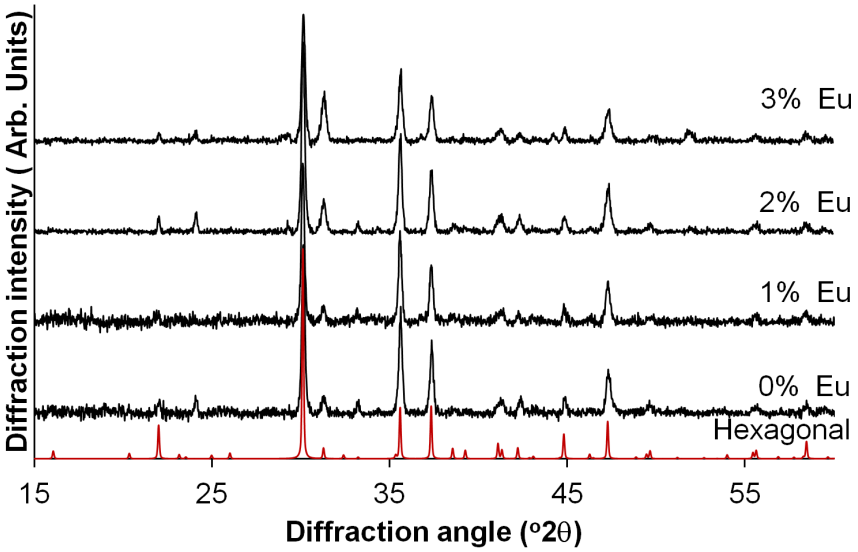

Figure 9.4: XRD spectra of undoped $CaAl_2O_4$ and Eu-doped $CaAl_2O_4$ annealed at 1000°C. The reference spectrum for the hexagonal phase is established upon [137].

After the determination of the optimum temperature to synthesize $CaAl_2O_4$:Eu, we investigated the optimum doping concentration for Eu at this temperature. Before the examination of concentration effects on the luminescence properties, we studied the influence of doping concentration on crystallization (Fig. 9.4). As seen in the spectra, no peaks related to impurity phases are observed. Consequently, these relatively low doping concentrations do not affect the crystallization.

Figure 9.5 shows the emission spectra of $CaAl_2O_4$:Eu annealed at 1000°C as a function of europium concentration, the spectra are recorded at an excitation wavelength of 330 nm. Increasing the europium concentration from 1% to 2% results in 3.5 times more intense emission. If we further increase the doping concentration to 3%, the Eu^{2+} emission intensity hardly changes, while that of Eu^{3+} still increases. This fact shows that an increase in the europium concentration beyond 2% results in an incorporation of doped europium as Eu^{3+}. Therefore the optimum europium concentration is around 2%, as we want to optimize the Eu^{2+} emission intensity.

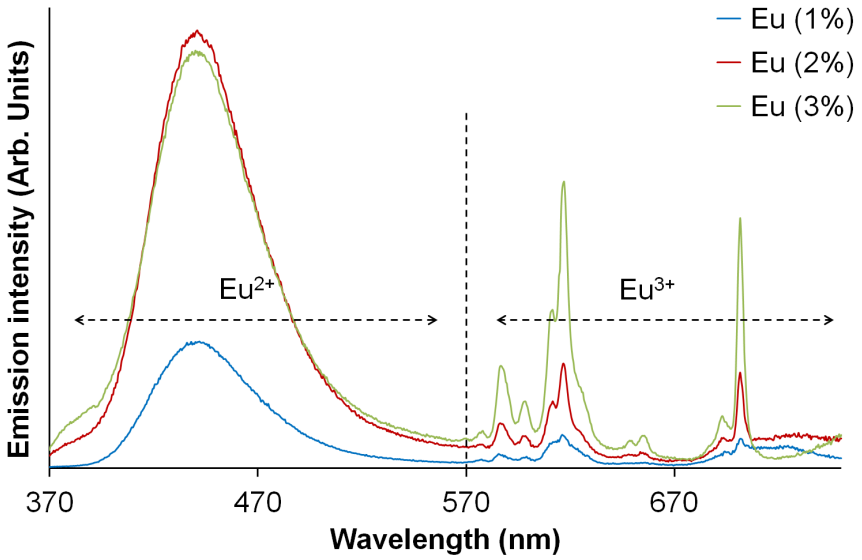

Figure 9.5: PL emission spectra of $CaAl_2O_4$:Eu annealed at 1000°C as a function of europium concentration. The emission spectra are recorded at an excitation wavelength of 330 nm.

9.2.3 Reduction of Eu^{3+} to Eu^{2+}

For persistent luminescence applications, the europium dopant has to be in its divalent state. Clearly, a large fraction of the europium ions is in a trivalent state after the thermal treatment required to form $CaAl_2O_4$. Different techniques are described in literature to reduce Eu^{3+} to Eu^{2+} in $CaAl_2O_4$ with post-annealing under H_2/N_2 atmosphere being the most commonly used [130, 136, 145].

We used two techniques to reduce Eu^{3+} to Eu^{2+} in $CaAl_2O_4$. The first one consists of post-annealing under H_2/N_2 (10%/90%) atmosphere and the second one is electron beam annealing in vacuum. Different post-annealing temperatures were tested to obtain only Eu^{2+} doped $CaAl_2O_4$ under H_2/N_2.

Figure 9.6 presents the relative emission intensity of Eu^{3+} (red line) and Eu^{2+} (blue line) $CaAl_2O_4$:Eu (1%) annealed at 1000°C as a function of post-annealing temperature under H_2/N_2. Before post annealing, only 1% of the total emission intensity belongs to Eu^{2+} as can be seen in Fig. 9.2b. By increasing the post-annealing temperature and time this ratio is increased to 65%. This ratio shows we could not achieve reduction of all Eu^{3+} to Eu^{2+} under this condition. Moreover, the powder color, which is white before post-

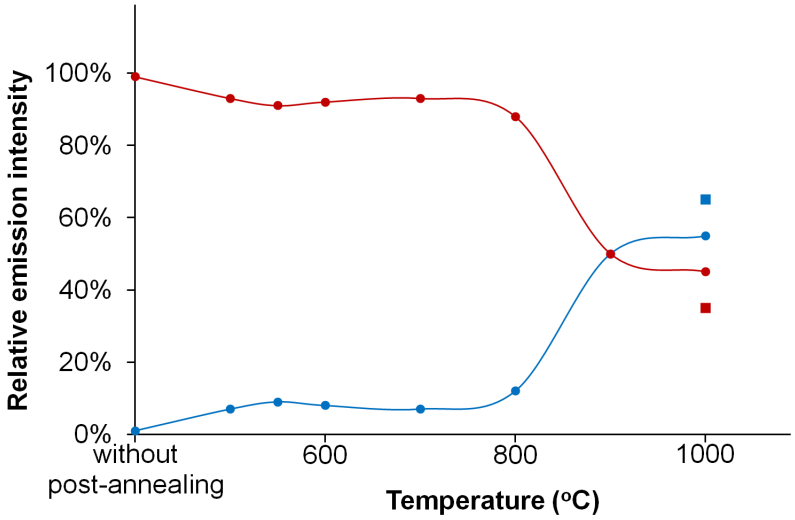

Figure 9.6: Relative PL emission intensity of Eu^{3+} (red line) and Eu^{2+} (blue line) in $CaAl_2O_4$ as a function of post-annealing temperature under H_2/N_2 for 20 min. The squares represent the post-annealing at 1000°C under H_2/N_2 for 60 min. The spectra were recorded at an excitation wavelength of 260 nm.

annealing, turns to gray by post-annealing under H_2/N_2 and gets darker by increasing the temperature. A powder with a gray body color is not desirable for a luminescent material due to the strong absorption of the luminescent emission. The gray body color is presumably related to removing oxygen from the material by annealing under H_2/N_2 atmosphere, although this was not analytically determined.

The normalized PL emission spectra of $CaAl_2O_4$:Eu (1%) annealed at 1000°C before (blue line) and after (red line) post-annealing for a few seconds using electron beam under vacuum is shown in Fig. 9.7. The emission spectra were recorded at an excitation wavelength of 260 nm which is one of the best excitation wavelengths to observe Eu^{3+} emission. As seen in this figure, after electron beam annealing, the Eu^{3+} emission peaks are not visible while only an emission band related to Eu^{2+} is present in the emission spectrum. This indicates that all Eu^{3+} is reduced to Eu^{2+}. In order to investigate the presence of trace amounts of Eu^{3+}, we excited $CaAl_2O_4$:Eu (1%) electron beam post-annealed powder using an excitation wavelength of 465 nm, which corresponds to the $^7F_0$-$^5D_2$ absorption of Eu^{3+} [184], and as Figs. 9.2a and 9.3 show, it is not possible to excite Eu^{2+} via this excitation wavelength. This emission spectrum consists of only noise and it suggest that no Eu^{3+} remains

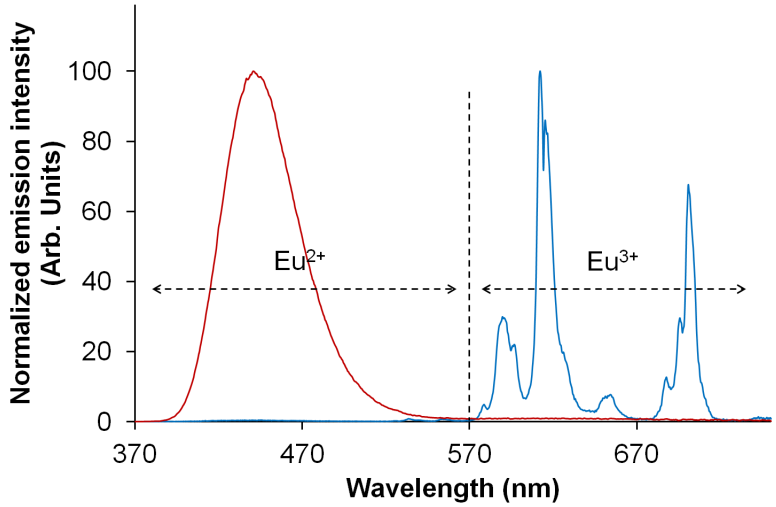

Figure 9.7: Normalized PL emission spectra of $CaAl_2O_4$:Eu (1%) annealed at 1000°C before (blue line) and after (red line) post-annealing using electron beam. The emission spectra are recorded at an excitation wavelength of 260 nm.

in $CaAl_2O_4$:Eu after electron beam annealing. In contrast with the post annealing under H_2/N_2 atmosphere, the electron beam post-annealing does not cause a change of the body color of the powders from white to gray.

The XRD spectra of $CaAl_2O_4$ doped with Eu^{2+} with different concentrations show the formation of a new phase ($Ca_{12}Al_{14}O_{33}$) for more than 1% europium concentration after after post-annealing under H_2/N_2 atmosphere (Fig. 9.8). The XRD spectra of the same samples indicate that no extra phase is formed by doping with europium before post-annealing (Fig. 9.4). However, the main difference is related to the phase of $CaAl_2O_4$. It is hexagonal before post-annealing (Fig. 9.4), but turns to monoclinic by post-annealing (Fig. 9.8).

We also checked the influence of the Eu^{2+} concentration on the PL characteristics (Fig. 9.9). The optimum europium concentration is around 2% before post-annealing, this is changing after post-annealing (Fig. 9.9). The emission spectra of $CaAl_2O_4$:Eu post-annealed as a function of europium concentration are indicated in Fig. 9.9. The most intense PL emission belongs to 1% Eu^{2+} doped $CaAl_2O_4$. Therefore the optimum Eu concentration, as evaluated by Eu^{2+} emission intensity only, can be different before and after post-annealing.

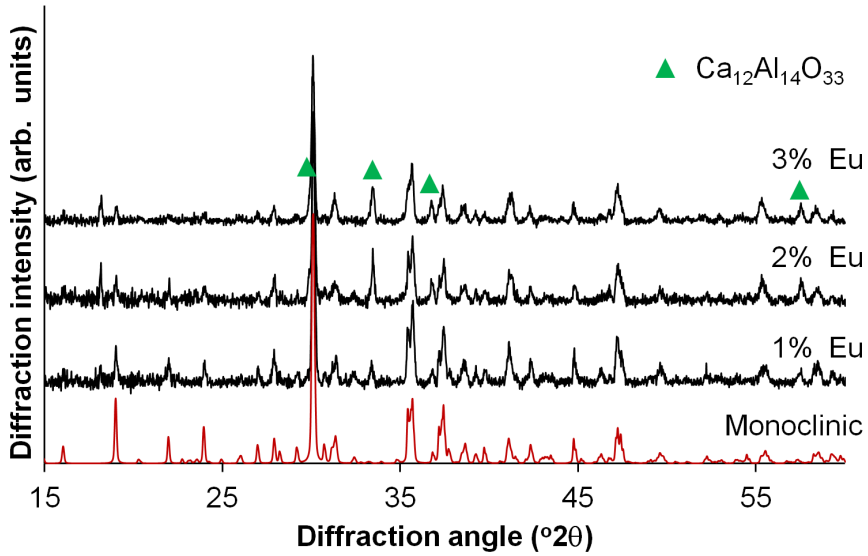

Figure 9.8: XRD spectra of $CaAl_2O_4$ doped with 1%, 2%, and 3% Eu^{2+} after post-annealing under H_2/N_2 atmosphere. The red spectrum indicate the peak positions and diffraction intensities of monoclinic $CaAl_2O_4$ (data from ICDD file no. 70-0134) and the green triangles represent the peak positions of $Ca_{12}Al_{14}O_{33}$ (data from ICDD file no. 09-0413).

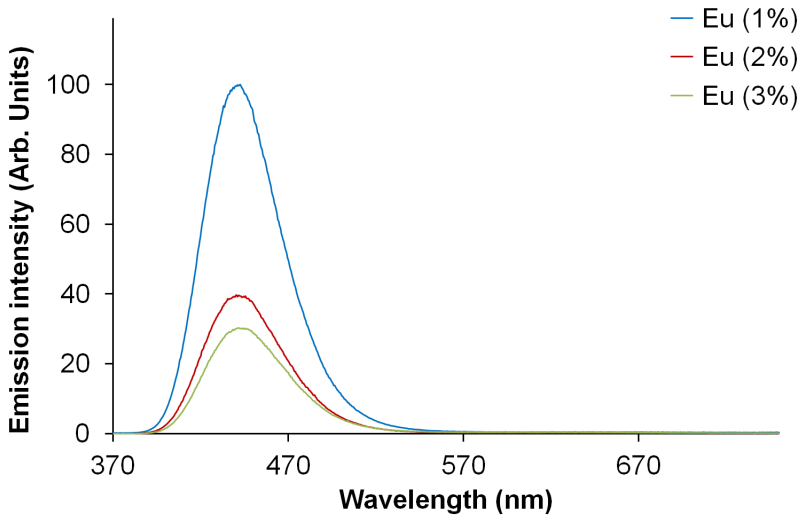

Figure 9.9: PL emission spectra of $CaAl_2O_4$:Eu^{2+} post-annealed as a function of europium concentration. The emission spectra are recorded at an excitation wavelength of 330 nm.

9.3 $CaAl_2O_4:Eu^{2+},Nd^{3+}$

The reported best co-dopant for $CaAl_2O_4:Eu^{2+}$ is Nd^{3+} (§5.6) under the consideration of the intensity and the duration of the afterglow. The influence of Nd^{3+} as co-dopant on crystal structure, PL characteristics and decay profile of $CaAl_2O_4:Eu^{2+}$ is studied in this section.

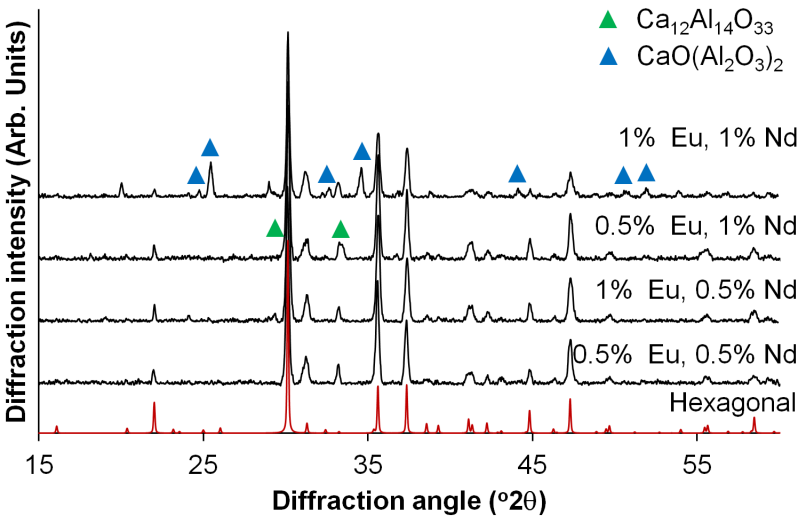

Figure 9.10: XRD spectra of $CaAl_2O_4:Eu^{2+},Nd^{3+}$ with different Eu^{2+} and Nd^{3+} concentrations annealed at 1000°C (before post-annealing). The red spectrum indicates the peak positions and diffraction intensities of hexagonal $CaAl_2O_4$ (data from [137]). The green triangles represent the peak positions of $Ca_{12}Al_{14}O_{33}$ (data from ICDD file no. 09-0413) and blue triangles indicate the peak positions of $CaO(Al_2O_3)_2$ (data from ICDD file no. 89-3851).

As seen in Fig. 9.10, when the concentrations of both Eu^{2+} and Nd^{3+} are 1%, even before post-annealing a $CaO(Al_2O_3)_2$ phase is detected besides the main phase (hexagonal). In addition to that, we also observed the formation of $Ca_{12}Al_{14}O_{33}$ when the Nd^{3+} concentration is higher than 0.5%. $CaAl_2O_4:Eu^{2+}$ (0.5%), Nd^{3+} (0.5%) and $CaAl_2O_4:Eu^{2+}$ (1%), Nd^{3+} (0.5%) have pure hexagonal phase.

Figure 9.11 shows the PL emission spectra recorded at an excitation wavelength of 330 nm of $CaAl_2O_4$ doped with 1% Eu^{2+} and $CaAl_2O_4$ doped with

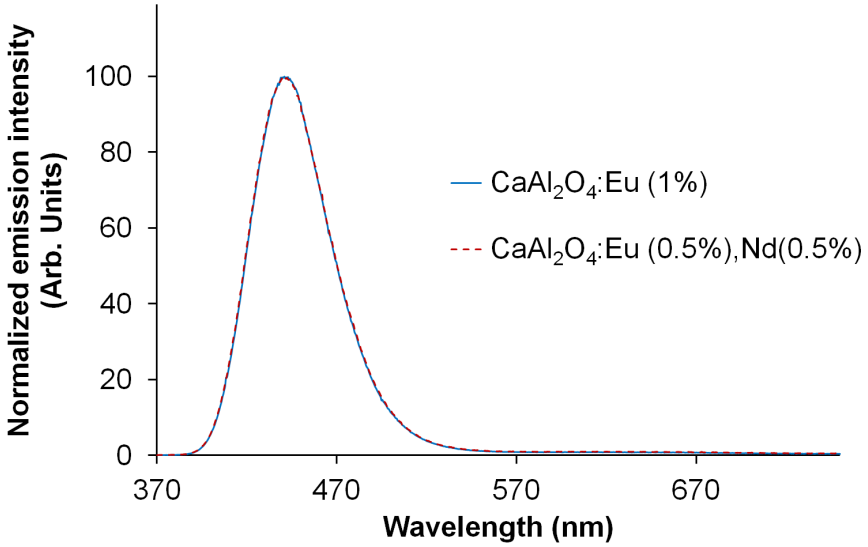

Figure 9.11: PL emission spectra recorded at an excitation wavelength of 330 nm of (solid blue line) $CaAl_2O_4:Eu^{2+}$ (1%) and (dashed red line) $CaAl_2O_4:Eu^{2+}$ (0.5%), Nd^{3+} (0.5%) after post-annealing.

0.5% Eu^{2+} and 0.5% Nd^{3+}. After the post-annealing, only Eu^{2+} emission can be observed: there is no Eu^{3+} emission and co-doping with Nd^{3+} ion does not affect the emission wavelength or the shape of the emission spectrum.

Comparison between decay profiles for commercial $CaAl_2O_4:Eu^{2+}$, Nd^{3+} purchased from Glotech (GTP3500A) [185] and $CaAl_2O_4:Eu^{2+}$ (0.5%), Nd^{3+} (0.5%) is presented in Fig. 9.12. As seen in the figure, for $CaAl_2O_4:Eu^{2+}$ (0.5%), Nd^{3+} (0.5%) a two-fold overall increase in afterglow intensity is achieved using the non-aqueous sol-gel technique, in combination with e-beam annealing.

9.4 Conclusions and perspectives

Aitasalo and colleagues reported that the strongest luminescence in $CaAl_2O_4$ is obtained for the monoclinic phase [135]. In the first stage of this study we examined the minimum synthesizing temperature for crystalline $CaAl_2O_4$. We have successfully synthesized crystalline $CaAl_2O_4$ at 900°C using a non-aqueous sol-gel method. Doping with rare earths has not affected this temperature. Although crystallization begins at 900°C, photoluminescence (PL) measurements indicated that the optimum temperature was 1000°C. For our

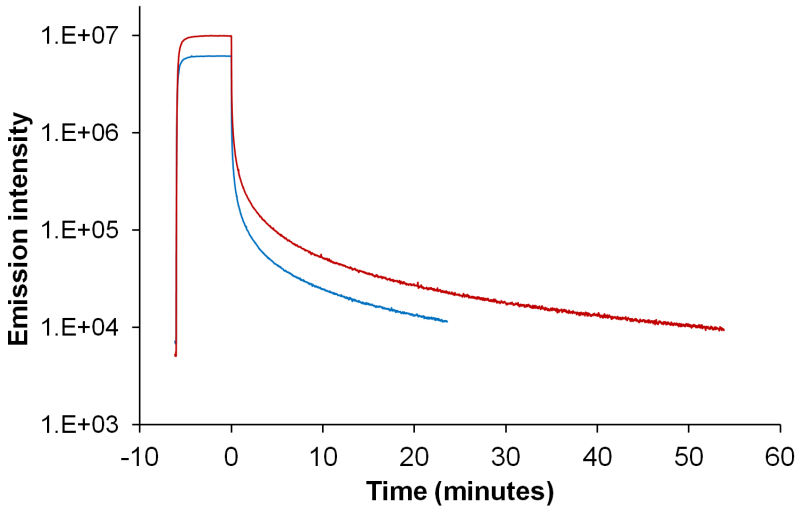

Figure 9.12: Decay profiles for (blue line) commercial $CaAl_2O_4:Eu^{2+}$, Nd^{3+} and (red line) $CaAl_2O_4:Eu^{2+}$ (0.5%), Nd^{3+} (0.5%). Powders were excited at 365 nm for 6 minutes.

synthesis method, it appeared that the largest crystalline fraction consists of the hexagonal phase, based on the absence of splitting of the diffraction peak at 35.5° (2θ). More information on the phase formation has been derived from the photoluminescence measurements. The strongest emission peak within the $^5D_0$-$^7F_2$ transition of Eu^{3+} lies at 616.5 nm, with a second less-intense one at 611 nm (Fig. 9.2b). This points at the Eu^{3+} emission mainly originating from the monoclinic phase, based on the spectra described in [137]. Also the excitation spectrum for the Eu^{3+} emission (Fig. 9.2a), with a strong CT-based excitation band, is typical for the monoclinic phase [137]. In the low-temperature range, the Eu^{2+} emission band peaks invariably at 440 nm, which is characteristic for the monoclinic phase [135]. Hence we can conclude that even for heat treatments at relatively low temperature, i.e. 900 to 1000°C, the monoclinic phase for $CaAl_2O_4$ is already obtained to a considerable extent. The absence of the monoclinic phase in the x-ray diffraction patterns could be due to nano-sized grains, leading to peak broadening, or due to a limited long-range order of the monoclinic phase.

The Eu doped $CaAl_2O_4$ contains Eu^{2+} and Eu^{3+} ions. Using post annealing, it is possible to reduce Eu^{3+} to Eu^{2+}. For this purpose, we used two methods: the first one is post-annealing under H_2/N_2 (10%/90%) atmosphere and the second one is electron beam annealing. We could manage to reduce part of the Eu^{3+} to Eu^{2+} via post-annealing under H_2/N_2 (10%/90%) as judged on

the integrated PL emission intensity for both valence states. However, this treatment resulted in gray powders. Using electron beam annealing we have reduced all Eu^{3+} to Eu^{2+} as no emission from Eu^{3+} could be detected. Additionally, the body color of the powders does not change by electron beam annealing.

Lastly, we have prepared $CaAl_2O_4$:Eu^{2+}, Nd^{3+}. Using Nd^{3+} as co-doping ion does not affect the emission wavelength or the shape of the emission spectrum. When the total doping concentration, combining Eu and Nd, is higher than 1.5%, extra phase formation is observed. The decay profile of sol-gel based $CaAl_2O_4$:Eu^{2+} (0.5%), Nd^{3+} (0.5%) was compared with commercial $CaAl_2O_4$:Eu^{2+}, Nd^{3+}. The overall afterglow intensity of the former was twice as high as the commercially available powder.

Chapter 10

Closing remarks

In this chapter, the original contributions of this research on the protection of sulfide luminescent particles against atmospheric conditions and relatively low temperature synthesis of persistent phosphors are summarized.

First, the degradation of CaS:Eu^{2+} particles in addition to luminescence properties, which were fabricated using a solvothermal synthesis method, was investigated to better understand the mechanism of degradation. These small particles were intentionally selected as a model system, since they are more sensitive against the atmospheric conditions than most other sulfides. Under high humidity, in only 18 hours, the PL emission intensity reduces to half of the initial value. Decomposition of the particles also depends on the temperature, decomposition rate is increasing with temperature. Only 26% of the PL emission intensity is lost after a heat treatment at 400°C, while after annealing at 450 and 500°C, the PL intensity decreases by 50% and 79%, respectively. However, performing more than two treatments does not influence the PL emission intensity anymore due to formation of $CaSO_4$ which covers the CaS surface and acts as a protection layer.

After the decomposition study of the CaS:Eu^{2+} particles, we explored sol-gel methods to prepare protection layers. The effect of the sol during coating was investigated using an Al_2O_3 sol synthesized by a strong acid and a little water, and TiO_2 sols. It was shown that the CaS:Eu^{2+} particles decomposed in seconds in the presence of acid and water. This required the development of non-aqueous sol-gel synthesis methods without the use of strong acids to prepare sols to cover the particles' surface.

Using a non-aqueous sol-gel method, crack free TiO_2 thin films with different thicknesses and porosities and TiO_2 powders with different phases were pre-

pared. After this study, TiO_2 was used as protection layer. We observed that the particles lose 50% of intensity by coating. In addition to that, CaS:Eu^{2+} particles coated with a TiO_2 layer decomposed as fast as uncoated particles at 80°C and 80% RH. It means that the TiO_2 layer did not protect the particles sufficiently in these conditions. This could be associated with different properties of the TiO_2 layer. Pore structure, crystallity and/or hydrophilicity of the layer may be related to insufficient protection. Although the main purpose of our study of TiO_2 thin films and powders was to assess the performance of TiO_2 as protection layer, we observed that TiO_2 prepared during this research was not suitable for this application.

Next to TiO_2, Al_2O_3 prepared without strong acids was used as protection layer. The optical and structural properties of the thin films were studied, before the performance of Al_2O_3 as protection layer was evaluated. We prepared thin films with different thicknesses with a maximum porosity of 29% using a non-aqueous sol-gel method developed in-house. After the coating with Al_2O_3, the emission intensity halved. However, the experimental results underline that the resistance of the phosphor layer against moisture and high temperature can be improved by coating with an alumina layer. In addition to the non-aqueous sol-gel technique, atomic layer deposition (ALD) was used to coat particles with Al_2O_3. Both techniques offered excellent resistance against moisture. A post-deposition heat treatment of the particles is not necessary for ALD coating unlike the sol-gel technique so it scarcely affects degradation of the particles. Therefore, ALD looks the better technique to prepare a protection layer for sulfides since it results in higher luminescence efficiency. Nevertheless, when ALD is compared with sol-gel techniques, ALD is more expensive as coating technique. Thus, sol-gel based inorganic coatings are an interesting route for the protection of luminescent sulfides. As a future work, we can try to decrease the heat treatment temperature.

Finally, we used a non-aqueous sol-gel method to synthesize luminescent materials. We prepared $CaAl_2O_4$:Eu^{2+}, Nd^{3+} which is a well know violet persistent luminescent material. In order to find the optimum conditions for this material, we prepared it in three stages. In the first one, we identified the optimum preparation temperature for $CaAl_2O_4$:Eu. This was 1000°C which is lower than the previously reported minimum temperature. $CaAl_2O_4$:Eu contains Eu^{3+} and Eu^{2+} ions, however only Eu^{2+} ions are responsible for the persistent luminescence. We used two methods to reduce the Eu^{3+} to Eu^{2+}, namely, post-annealing under H_2/N_2 (10%/90%) atmosphere and electron beam annealing. We managed to reduce all Eu^{3+} to Eu^{2+} using the latter

type of annealing. In the last stage Nd^{3+} was incorporated in $CaAl_2O_4:Eu^{2+}$ to prolong and intensify the afterglow. Neither the emission wavelength nor the shape of the emission spectrum changed by using Nd^{3+} as co-doping. Lastly, the decay profile of $CaAl_2O_4:Eu^{2+}$ (0.5%), Nd^{3+} (0.5%) was compared to commercially available $CaAl_2O_4:Eu^{2+}$, Nd^{3+}. Our sol-gel based $CaAl_2O_4:Eu^{2+}$ (0.5%), Nd^{3+} (0.5%) showed an afterglow intensity which was twice as high.

Sol-gel based processes have a broad application area and this research underlines that it can be used to coat moisture sensitive materials like sulfides. The same protection quality can be obtained by using sol-gel method as with ALD. Furthermore, it offers cheap and simple protection. However, there are two main issues limiting the application of sol-gel for protection coatings of sulfides. The first one is annealing temperature after coating and the second one is porosity. If annealing temperature can be reduced, this significantly limits the degradation of particles during annealing. It is also very important to control the porosity, to not allow moisture to reach the particles through the pores.

Chapter 11

List of publications

11.1 Publications directly related to this research

- **N. Avci**, K. Korthout, M. A. Newton, P. F. Smet, D. Poelman
  Valence states of europium in $CaAl_2O_4$:Eu phosphors
  Opt. Mater. Express, Accepted, 2012

- **N. Avci**, P. F. Smet, J. Lauwaert, H. Vrielinck, D. Poelman
  Optical and structural properties of aluminium oxide thin films by non-aqueous sol-gel techniques
  J. Sol-Gel Sci. Technol., 59:327-333, 2011

- **N. Avci**, I. Cimieri, P. F. Smet, D. Poelman
  Stability improvement of moisture sensitive CaS:Eu^{2+} micro-particles by coating with sol-gel alumina
  Opt. Mater., 33:1032-1035, 2011

- **N. Avci**, J. Musschoot, P. F. Smet, K. Korthout, A. Avci, C. Detavernier, D. Poelman
  Microencapsulation of moisture-sensitive CaS:Eu^{2+} particles with aluminum oxide
  J. Electrochem. Soc., 156:J333-J337, 2009

- **N. Avci**, P. F. Smet, H. Poelman, N. Van de Velde, K. De Buysser, I. Van Driessche, D. Poelman
  Characterization of TiO_2 powders and thin films prepared by non-aqueous sol-gel techniques
  J. Sol-Gel Sci. Technol., 52: 424-431, 2009

11.2 Other publications

- M. Arin, P. Lommens, **N. Avci**, S. C. Hopkins, K. De Buysser, I. M. Arabatzis, I. Fasaki, D. Poelman, I. Van Driessche
  Ink-jet printing of TiO_2 films from water based sol-gel precursors
  J. European Ceram. Soc., 31:1067-1074, 2011

- D. Poelman, **N. Avci**, P. F. Smet
  Measured luminance and visual appearance of multi-color persistent phosphors
  Opt. Express, 17:358-364, 2009

- P. F. Smet, **N. Avci**, D. Poelman
  Red persistent luminescence in Ca_2SiS_4:Eu,Nd
  J. Electrochem. Soc. ,156:H243-H248, 2009

- P. F. Smet, **N. Avci**, B. Loos, J. E. Van Haecke, D. Poelman
  Structure and photoluminescence of (Ca, Eu)$_2SiS_4$ powders
  J. Phys.-Condes. Matter, 19:246223, 2007

11.3 International conference contributions

- **N. Avci**, P. F. Smet, D. Poelman
  Improvement on $CaAl_2O_4$:Eu^{2+},Nd^{3+}: lower temperature synthesis, longer afterglow duration
  Phosphoros International Workshop on Persistent Phosphors, 19-20 Sept. 2011, Ghent, Belgium.

- **N. Avci**, P. F. Smet, D. Poelman
  Non-aqueous sol-gel synthesis of $CaAl_2O_4$:Eu
  Advanced Complex Inorganic Nano-materials (ACIN 2011), 11-14 Sept. 2011, Namur, Belgium.

- D. Poelman, A. Parmentier, K. Korthout, K. Van den Eeckhout, **N. Avci**, I. Cimieri, J. Botterman, P. F. Smet
  New classes of phosphors for emerging lighting applications
  15^{th} International Workshop on Inorganic and Organic Electroluminescence, 2010 International Conference on the Science and Technology of Emissive Displays and Lighting, and XVIII Advanced Display Technologies International Symposium (EL 2010) , 27 Sept.-01 Oct. 2010, St. Petersburg, Russia.

- I. Cimieri, H. Poelman, **N. Avci**, D. Poelman
  Sol-gel preparation of pure and doped TiO_2 films for photocatalytic oxidation of ethanol on air
  Air Pollution Abatement Catalysis, 2^{nd} International Symposium, 8-11 Sept. 2010, Cracow, Poland.

- P. F. Smet, **N. Avci**, D. Poelman
  Stability improvement of luminescence CaS:Eu particles by encapsulation
  E-MRS 2010 Spring Meeting, 7-11 June 2010, Strasbourg, France.

- P. F. Smet, K. Korthout, A. Parmentier, **N. Avci**, D. Poelman
  Rare earth doped sulfides as colour conversion phosphors: an overview and new candidates
  3^{rd} International Workshop on Photoluminescence in Rare Earths: Photonic Materials and Devices (PRE'10), 28-30 Apr. 2010, Florence, Italy.

- **N. Avci**, P. F. Smet, K. De Buysser, I. Van Driessche, S. Hoste, D. Poelman
  Synthesis and photoluminescence characteristics of Al_2O_3 thin films doped with (Ca,Sr)S:Eu^{2+}
  14^{th} International Workshop on Inorganic and Organic Electroluminescence, and 2008 International Conference on the Science and Technology of Emissive Displays and Lighting, 9-12 Sept. 2008, Rome, Italy.

- P. F. Smet, **N. Avci**, D. Poelman
  Morphology and luminescence of solvothermally deposited (Ca,Sr)S:Eu^{2+} thin films
  14^{th} International Workshop on Inorganic and Organic Electroluminescence , and 2008 International Conference on the Science and Technology of Emissive Displays and Lighting, 9-12 Sept. 2008, Rome, Italy.

- D. Poelman, K. Rijpstra, **N. Avci**, A. Samaneh, P. F. Smet
  Spectral design consideration for multi-colour persistent phosphors
  14^{th} International Workshop on Inorganic and Organic Electroluminescence , and 2008 International Conference on the Science and Technology of Emissive Displays and Lighting, 9-12 Sept. 2008, Rome, Italy.

- K. De Buysser, I. Van Driessche, **N. Avci**, P. F. Smet, D. Poelman, T. Vander Hoogerstraete, M. Cuadradogil, J. Schaubroeck, S. Hoste
  Soft chemistry: Low temperature synthesis and bio-templating
  6^{th} International Mesostructured Materials Symposium (IMMS), 8-11 Sept. 2008, Namur, Belgium.

- **N. Avci**, P. F. Smet, D. Poelman
  Synthesis and photoluminescence characteristics of Al_2O_3 thin films doped with (Ca,Sr)S:Eu^{2+}
  15^{th} International Conference on Luminescence and Optical Spectroscopy of Condensed Matter (ICL'08), 7-11 July 2008, Lyon, France.

- P. F. Smet, **N. Avci**, D. Poelman
  Red persistent luminescence in rare-earth codoped Ca_2SiS_4:Eu^{2+}
  15^{th} International Conference on Luminescence and Optical Spectroscopy of Condensed Matter (ICL'08), 7-11 July 2008, Lyon, France.

- K. De Buysser, I. Van Driessche, **N. Avci**, P. F. Smet, D. Poelman, T. Vander Hoogerstraete, M. Cuadradogil, J. Schaubroeck, S. Hoste,
  Soft chemistry: bio-templating of Al_2O_3
  2^{nd} International Conference on Ceramics, 29 June-04 July 2008, Verona, Italy.

- D. Poelman, J. E. Van Haecke, **N. Avci**, P. F. Smet
  Advances in sulfide phosphors for wavelength conversion in LEDs
  The 4^{th} International Symposium on Display and Lighting Phosphor Materials (ISDLPM'07), 08 Dec. 2007, Tokyo, Japan.

- **N. Doner**, B. Loos, P. F. Smet, J. E. Van Haecke, E. Michelena, D. Poelman
  Radiative properties of Ca_2SiS_4:Eu powder
  13^{th} International Workshop on Inorganic and Organic Electroluminescence, and 2006 International Conference on the Science and Technology of Emissive Displays and Lighting, 18-22 Sept. 2006, Jeju Island, Korea.

- P. F. Smet, **N. Doner**, B. Loos, J. E. Van Haecke, D. Poelman
  Correlating structural and photoluminescent properties of $(Ca,Eu)_2SiS_4$ phosphors
  E-MRS 2007 Spring Meeting, 28 May-01 June 2007, Strasbourg, France.

11.4 Other contributions

- **N. Doner**, B. Loos, P. F. Smet, J. E. Van Haecke, E. Michelena, D. Poelman
  Synthesis and characterization of luminescent Ca_2SiS_4:Eu powder
  Joint Annual Scientific Meeting of the Dutch and the Belgian Physical Society (Fysica 2006), 28 Apr. 2006, Leiden, The Netherlands.

Chapter 12

Nederlandstalige samenvatting

Luminescente materialen zijn alomtegenwoordig in de moderne maatschappij: we vinden ze in fluorescentielampen, veiligheidssignalisatie en beeldschermen, in witte LED's met een hoog rendement, en ze worden recent ook toegepast in de medische beeldvorming. De meeste dergelijke materialen (ook fosfors genoemd) zijn anorganische halfgeleiders, gedoteerd met onzuiverheidsionen - vaak zeldzame aarden (lanthaniden) - van waaruit de lichtemissie gebeurt. Deze halfgeleiders moeten een grote verboden zone bezitten (anders zijn ze niet transparant voor het opgewekte licht) en geschikt zijn voor de substitutionele inbouw van de zeldzame aarden.

Wanneer de optische transities binnen de onzuiverheidsionen sterk beïnvloed worden door het omringende rooster, dan is het de combinatie van de energieniveaus van het lanthanide-ion én zijn interacties met het rooster die de uiteindelijke golflengte en dus ook de kleur van de emissie bepaalt. Een van de meest gebruikte zeldzame aarden voor luminescente toepassingen is europium. In driewaardige toestand (Eu^{3+}) vertoont het scherpe emissiepieken ten gevolge van f-f transities in het rode gebied van het spectrum, terwijl Eu^{2+} een breedbandemissie heeft, perfect geschikt voor verlichtingstoepassingen met een goede kleurweergave. Door de keuze van een geschikt gastrooster kan de emissie van Eu^{2+} verschoven worden over vrijwel het volledige zichtbare gebied; specifiek in het rode gebied is de keuze aan mogelijke gastroosters schaars, en een van de beste kandidaten is hier CaS. Hoewel CaS:Eu een uitstekende rode fosfor is, heeft het materiaal als belangrijk nadeel dat het (zoals veel sulfides) erg vochtgevoelig is. Dit effect zorgt ervoor dat CaS:Eu moeilijk kan toegepast worden in "real world" toepassingen, tenzij de fosfordeeltjes beschermd worden tegen de atmosfeer.

Het onderzoek van dit doctoraatsproefschrift had tot doel de mogelijkheden

van sol-gel synthese van anorganische materialen te onderzoeken voor luminescente toepassingen. Deze techniek is naar toepassingen toe bijzonder aantrekkelijk, omdat zowel poeders als dunne filmen kunnen worden geproduceerd met een uitstekende homogeniteit; de samenstellende componenten worden immers in oplossing gebracht, zodat er homogeniteit op moleculaire schaal ontstaat. Bovendien kan bij sol-gelsyntheses vaak gewerkt worden bij lage temperatuur, en is er geen vacuüm nodig bij de depositie van dunne lagen.

In het eerste en grootste deel van dit proefschrift wordt onderzocht op welke manier luminescente CaS:Eu deeltjes tegen luchtvochtigheid kunnen worden beschermd via depositie van sol-gel lagen. Het eerste materiaal dat hiervoor werd gebruikt is TiO_2. Titaandioxide is een materiaal dat vrij eenvoudig met een dergelijke synthese in dunne-filmvorm kan worden gebracht. In het huidig werk moest echter specifiek gewerkt worden met een minder gebruikelijke watervrije sol-gel synthese; de aanwezigheid van water in de oplossing zou de luminescente deeltjes immers zeer snel doen degraderen. Verschillende types TiO_2 dunne filmen werden afgezet, en gekarakteriseerd op hun structurele en optische eigenschappen. Voor het testen van de degradatie van de luminescente deeltjes werd een opstelling ontwikkeld waarmee in-situ de luminescentie kon worden gemeten tijdens een versnelde veroudering bij hoge temperatuur en hoge vochtigheidgraad. Hoewel TiO_2-lagen met uitstekende fysische eigenschappen bekomen werden, boden deze niet of nauwelijks bescherming tegen degradatie, vermoedelijk omwille van een combinatie van de porositeit van de lagen en hun kristalliniteit en superhydrofiliciteit.

Daarnaast werden Al_2O_3-lagen met een watervrije sol-gel synthese aangemaakt. Dergelijke lagen werden na karakterisatie getest op hun beschermende eigenschappen, dit keer met een uitstekend resultaat: de levensduur van de CaS:Eu deeltjes in vochtige en warme condities kon met verschillende grootteordes worden verbeterd. Ter vergelijking werden de deeltjes ook individueel gecoat met behulp van ALD (atomaire laagdepositie), een techniek die toelaat zeer dichte en defectvrije lagen te groeien. De resultaten van beide technieken (sol-gel en ALD) lagen zeer dicht bij elkaar, wat de potentiële waarde van sol-gelsynthese als snelle en goedkope depositietechniek illustreert.

In het tweede deel van het werk werd nagegaan of met behulp van solgeltechnieken zeldzame-aardgedoteerde luminescente materialen konden worden geproduceerd. Hierbij werd gekozen voor $CaAl_2O_4$:Eu, een interessant fosformateriaal, dat echter hoge procestemperaturen vereist voor de aan-

maak. Dank zij de ervaring met de eerder gesynthetiseerde materialen kon er op zeer korte termijn een techniek ontwikkeld worden voor de productie van $CaAl_2O_4$:Eu poederfosfors. De vereiste temperatuur bleek bovendien enkele honderden graden lager te liggen dan de gepubliceerde waarden (waarbij gebruik gemaakt werd van traditionele methodes zoals vastestofreacties). Na synthese vertoonden de $CaAl_2O_4$:Eu poeders echter vrijwel enkel de karakteristieke lijnemissie van Eu^{3+}. Daarom werden verschillende nabehandelingsprocedures uitgetest voor de reductie van Eu^{3+} tot Eu^{2+}. Zowel een nabehandeling in N_2/H_2 als een elektronenbundelbestraling in vacuüm bleken hiervoor succesvol.

Tijdens bijkomend onderzoek werd getracht de $CaAl_2O_4$:Eu poeders persistent luminescent te maken door codotering met Nd^{3+}. Dit $CaAl_2O_4$:Eu,Nd is een van de meest performante persistent luminescente materialen, met een nalichtingstijd na excitatie van enkele tientallen uren. Met de geoptimaliseerde synthesemethode, gecombineerd met elektronenbundelbestraling, werden fosfors bekomen met een lichtopbrengst die het dubbele is van de huidig beschikbare commerciële producten.

Bibliography

[1] C. J. Brinker and G. W. Scherer. *Sol-Gel Science The Physics and Chemistry of Sol-Gel Processing*. Academic Press, Boston, 1990.

[2] J. D. Wright and N. A. J. M. Sommerdijk. *Sol-Gel Materials Chemistry and Applications*. CRC Press, Boco Raton, 2001.

[3] N. Avci, P. F. Smet, H. Poelman, N. Van de Velde, K. De Buysser, I. Van Driessche, and D Poelman. Characterization of TiO_2 powders and thin films prepared by non-aqueous sol-gel techniques. *J. Sol-Gel Sci. Technol.*, 52(3):424–431, 2009.

[4] A. Boumaza, L. Favaro, J. Lédion, G. Sattonnay, J. B. Brubach, P. Berthet, A. M. Huntz, P. Roy, and R. Tétot. Transition alumina phases induced by heat treatment of boehmite: An x-ray diffraction and infrared spectroscopy study. *J. Solid State Chem.*, 182(5):1171–1176, 2009.

[5] B. Dong, T. Yang, and M. K. Lei. Optical high temperature sensor based on green up-conversion emissions in Er^{3+} doped Al_2O_3. *Sens. Actuators B: Chem.*, 123(2):667–670, 2007.

[6] N. Avci, J. Musschoot, P. F. Smet, K. Korthout, A. Avci, C. Detavernier, and D Poelman. Microencapsulation of moisture-sensitive CaS:Eu^{2+} particles with aluminum oxide. *J. Electrochem. Soc.*, 156(11):J333–J337, 2009.

[7] N. Avci, I. Cimieri, P. F. Smet, and D Poelman. Stability improvement of moisture sensitive CaS:Eu^{2+} micro-particles by coating with sol-gel alumina. *Opt. Mater.*, 33(7):1032–1035, 2011.

[8] P. F. Smet, I. Moreels, Z. Hens, and D. Poelman. Luminescence in sulfides: A rich history and a bright future. *Materials*, 3(4):2834–2883, 2010.

[9] D. Poelman, R. Vercaemst, R. L. VanMeirhaeghe, W. H. Laflere, and F. Cardon. Influence of the growth conditions on the properties of CaS:Eu electroluminescent thin films. *J. Lumin.*, 75(2):175–181, 1997.

[10] M. Weidner, A. Osvet, G. Schierning, M. Batentschuk, and A. Winnacker. Influence of dopant compounds on the storage mechanism of CaS:Eu^{2+}, Sm^{3+}. *J. Appl. Phys.*, 100(12):073701, 2006.

[11] H. H. Shin, J. H. Kim, B. Y. Han, and J. S. Yoo. Failure analysis of a phosphor-converted white light-emitting diode due to the CaS:Eu phosphor. *Jpn. J. Appl. Phys.*, 47(5):3524–3526, 2008.

[12] J. W. Brightwell, B. Ray, P. Sephton, and I. V. F. Viney. Composition effects on excitation and fluorescence emission-spectra in $Ca_xSr_{1-x}S$. *J. Cryst. Growth.*, 86(1-4):634–638, 1988.

[13] J. Madarász, T. Leskelä, J. Rautanen, and L. Niinistö. Oxidation of alkaline-earth-metal sulfide powders and thin films. *J. Mater. Chem.*, 6(5):781–787, 1996.

[14] C. F. Guo, B. L. Chu, M. M. Wu, and Q. Su. Oxide coating for alkaline earth sulfide based phosphor. *J. Lumin.*, 105(2-4):121–126, 2003.

[15] C. F. Guo, B. L. Chu, and Q. Su. Improving the stability of alkaline earth sulfide-based phosphors. *Appl. Surf. Sci.*, 225(1-4):198–203, 2004.

[16] S. H. Yoo and C. K. Kim. Nanocomposite encapsulation of CaS:Eu light-emitting diode phosphors for the enhancement of the stability against moisture. *J. Electrochem. Soc.*, 156(7):J170–J173, 2009.

[17] I. W. Park, J. H. Kim, J. S. Yoo, H. H. Shin, C. K. Kim, and C. K. Choi. Longevity improvement of CaS:Eu phosphor using polymer binder coating for white LED application. *J. Electrochem. Soc.*, 155(5):J132–J135, 2008.

[18] M. Suchea, S. Christoulakis, M. Androulidaki, and E. Koudoumas. CaS:Eu,Sm and CaS:Ce,Sm films grown by embedding active powder into an inert matrix. *Mater. Sci. Eng. B-Adv.*, 150(2):130–134, 2008.

[19] K. Van den Eeckhout, P. F. Smet, and D. Poelman. Persistent luminescence in Eu^{2+}-doped compounds: A review. *Materials*, 3(4):2536–2566, 2010.

[20] W. M. Yen, S. Shionoya, and H. Yamamoto. *Phosphor Handbook Second Edition*. CRC Press, Boca Raton, 2007.

[21] G. Blasse and B. C. Grabmaier. *Luminescent materials*. Springer-Verlag, Berlin, 1994.

[22] A. H. Kitai. *Solid state luminescence*. Chapman & Hall, Londan, 1993.

[23] B. Henderson and G. F. Imbusch. *Optical Spectroscopy of Inorganic Solids*. Oxford university press, New York, 1989.

[24] P. F. Smet, N. Avci, B. Loos, J. E. Van Haecke, and D. Poelman. Structure and photoluminescence of (Ca, Eu)$_2$SiS$_4$ powders. *J. Phys. Condens. Mater.*, 19(246223), 2007.

[25] P. Dorenbos. Energy of the first $4f^7 \rightarrow 4f^6 5d$ transition of Eu^{2+} in inorganic compounds. *J. Lumin.*, 104(4):239–260, 2003.

[26] J. Emsley. *Nature's building blocks: an A-Z guide to the elements*. Oxford university press, New York, 2003.

[27] C. Ronda. *Luminescence from theory to applications*. WILEY-VCH, Weinheim, 2008.

[28] Y. L. Cheng, Y. Zhao, Y. F. Zhang, and X. Q. Cao. Preparation of $SrAl_2O_4$:Eu^{2+}, Dy^{3+} fibers by electrospinning combined with sol-gel process. *J. Colloid Interf. Sci.*, 344(2):321–326, 2010.

[29] Y. Q. Li, J. E. J. van Steen, J. W. H. van Krevel, G. Botty, A. C. A. Delsing, F. J. DiSalvo, G. de With, and H. T. Hintzen. Luminescence properties of red-emitting $M_2Si_5N_8$:Eu^{2+} (M = Ca, Sr, Ba) LED conversion phosphors. *J. Alloy. Compd.*, 417(1-2):273–279, 2006.

[30] N. Avci, P. Smet, and D. Poelman. Non-aqueous sol-gel synthesis of $CaAl_2O_4$:Eu. In *International Symposium on Advanced Complex Inorganic Nanomaterials*, Ghent, Belgium, 2011.

[31] P. Dorenbos. Relation between Eu^{2+} and Ce^{3+} f $\leftrightarrow$ d-transition energies in inorganic compounds. *J. Phys.- Condens Mat.*, 15(27):4797–4807, 2003.

[32] P. F. Smet, J. E. Van Haecke, F. Loncke, H. Vrielinck, F. Callens, and D. Poelman. Anomalous photoluminescence in BaS : Eu. *Phys. Rev. B*, 74(3):035207, 2006.

[33] J. E. Van Haecke, P. F. Smet, K. De Keyser, and D. Poelman. The influence of source powder composition on the electroluminescence of $Ca_{1-x}S_x$: Eu thin films. *J. Electrochem. Soc.*, 154(9):J278–J281, 2007.

[34] Sol-gel technology and products. Website, 2011. `http://www.chemat.com/`.

[35] M. Niederberger. Nonaqueous sol-gel routes to metal oxide nanoparticles. *Accounts Chem. Res.*, 40(9):793–800, 2007.

[36] J. Livage, M. Henry, and C. Sanchez. Sol-gel chemistry of transition matal oxides. *Prog. Solid St. Chem.*, 18(4):259–341, 1988.

[37] B.E. Yoldas. Modification of polymer-gel structures. *J. Non-Cryst. Solids*, 63(1-2):145–154, 1984.

[38] N. Ya. Turova, E. P. Turevskaya, V. G. Kessler, and M. I. Yanovskaya. *The chemistry of metal alkoxides*. Kluwer Academic Publishers, New York, 2002.

[39] C. P. Alain. *Introduction to Sol-Gel Processing*. Kluwer Academic Publishers, Boston, 1998.

[40] B.E. Yoldas. Hydrolysis of aluminum alkoxides and bayerite conversion. *J. Appl. Chem. Biotechn.*, 23(11):803–809, 1973.

[41] B.E. Yoldas. Effect of variations in polymerized oxides on sintering and crystalline lkansformations. *J. Am. Ceram. Soc.*, 65(8):387–393, 1982.

[42] C. Sanchez, J. Livage, M. Henry, and F. Babonneaus. Chemical modification of alkoxide precursors. *J. Non-Cryst. Solids*, 100(8):1–3, 1988.

[43] A. Vioux. Nonhydrolytic sol-gel routes to oxides. *Chem. Mater.*, 9(11):2292–2299, 1997.

[44] F. Ungureanu, R. Medianu, R. V. Ghita, C. C. Negrila, P. Ghita, A. S. Manea, and M. F. Lazarescu. Properties of TiO_2 thin films prepared by different techniques. *J. Optoelectron Adv. Mater.*, 9(5):1457–1461, 2007.

[45] C. Legrand-Buscema, C. Malibert, and S. Bach. Elaboration and characterization of thin films of TiO_2 prepared by sol-gel process. *Thin Solid Films*, 418(2):79–84, 2002.

[46] P. Kajitvichyanukul and P. Amornchat. Effects of diethylene glycol on TiO_2 thin film properties prepared by sol-gel process. *Sci. Technol. Adv. Mater.*, 6(3-4):344–347, 2005.

[47] T. Yang, H. Wang, and M.K. Lei. Phase transition of Er^{3+} doped Al_2O_3 powders prepared by the non-aqueous sol-gel method. *Mater. Phys. Chem.*, 95(2-3):211–217, 2006.

[48] S. W. Choi, N. H. Kim, Y. H. Yun, and S. C. Choi. Photoluminescence properties of $SrAl_2O_4$ and $CaAl_2O_4$ long-phosphorescent phosphors synthesized by an oxalate coprecipitation method. *J. Ceram. Process. Res.*, 7(1):62–65, 2006.

[49] Schematic representation of an ALD process. Website, 2011. `http://cnx.org/content/m25737/latest`.

[50] J. Musschoot, Q. Xie, S. Van den Berghe, R.L. Van Meirhaeghe, and C. Detavernier. Atomic layer deposition of titanium nitride from TDMAT precursor. *Microelectron. Eng.*, 86(1):72–77, 2009.

[51] S.H.K. Park, J. Oh, C.S. Hwang, J.I. Lee, S.Y. Yang, and H.Y. Chu. Ultrathin film encapsulation of an OLED by ALD. *Electrochem. Solid-State Lett.*, 8(2):H21–H23, 2005.

[52] J. Goldstein, D. Newbury, D. Joy, C. Lyman, P. Echlin, E. Lifshin, L. Sawyer, and J. Michael. *Scaning Electron Microscopy and X-Ray Microanalysis*. Kluwer Academic/Plenum Publishers, New York, 2003.

[53] Edinburgh Instruments. *Operating instructions, FS920 Steady State Fluorescence Spectrometer Software*. 2003.

[54] A. C. Galca, E. S. Kooij, H. Wormeester, C. Salm, V. Leca, J. H. Rector, and B. Poelsema. Structural and optical characterization of porous anodic aluminum oxide. *J. Appl. Phys.*, 94(7):4296–4305, 2003.

[55] Simultaneous DTA/TGA. Website, 2011. `http://www.ortonceramic.com/instruments/04iST.shtml`.

[56] Overview of thermal analysis. Website, 2011. `http://www.groupes.polymtl.ca/lanomat/modules/facilities/index.php?content_id=15`.

[57] K. Nakamoto. *Infrared and raman spectra of inorganic and coordination compounds*. John Wiley & Sons, New York, 1986.

[58] Introduction to fourier transform infrared spectrometry. Website, 2011. `http://mmrc.caltech.edu/FTIR/FTIRintro.pdf`.

[59] LED monitors. Website, 2011. `http://ledmonitors.info/`.

[60] P. F. Smet, A. B. Parmentier, Z. Hens, and D. Poelman. Selecting conversion phosphors for white light-emitting diodes. *J. Electrochem. Soc.*, 158(6):R37–R54, 2011.

[61] E. F. Schubert. *Light-emitting diodes second edition*. Cambridge University Press, Cambridge, 2006.

[62] White light sources based on wavelength converters. Website, 2011. `http://www.ecse.rpi.edu/~schubert/Light-Emitting-Diodes-dot-org/chap21/chap21.htm`.

[63] J. E. Van Haecke, P. F. Smet, and D. Poelman. Single crystal CaS : Eu and SrS : Eu luminescent particles obtained by solvothermal synthesis. *Spectrochim. Acta Part B*, 59(10-11):1759–1764, 2004.

[64] D. R. Vij. *Handbook of electroluminescent materials*. Institute of physics publishing, Bristol, 2004.

[65] R. Pandey and S. Sivaraman. Spectroscopic properties of defects in alkaline-earth sulfides. *J. Phys. Chem. Solids.*, 52(1):211–225, 1991.

[66] W. M. Yen and M. J. Weber. *Inorganic phosphors composition, preparation and optical properties*. CRC Press, Boca Raton, 2004.

[67] P. J. Liu and Y. L. Liu. Preparation of CaS : Eu^{2+} phosphor by microwave heating method and its luminescence. *Chinese Chem. Lett.*, 11(9):843–846, 2000.

[68] Y. Hu, W. D. Zhuang, H. Q. Ye, S. S. Zhang, Y. Fang, and X. W. Huang. Preparation and luminescent properties of $(Ca_{1-x},Sr_x)S : Eu^{2+}$ red-emitting phosphor for white LED. *J. Lumin.*, 111(3):139–145, 2005.

[69] P. F. Smet and D. Poelman. Templated growth of textured and luminescent CaS:Eu thin films by a low-temperature solvothermal process. *J. Phys. D: Appl. Phys.*, 42(9):095306, 2009.

[70] N. Yamashita, O. Harada, and K. Nakamura. Photoluminescence spectra of Eu^{2+} centers in Ca(S,Se)Eu and Sr(S,Se)Eu. *Jpn. J. Appl. Phys.*, 34(10):5539–5545, 1995.

[71] D. D. Jia and X. J. Wang. Alkali earth sulfide phosphors doped with Eu^{2+} and Ce^{3+} for LEDs. *Opt. Mater.*, 30(3):375–379, 2007.

[72] T. Suzuki, H. Yamamoto, K. Megumi, O. Kanehisa, Y. Morita, N. Watanabe, and Y. Uehara. Hydrolysis reactions of CaAs phosphors. *J. Electrochem. Soc.*, 134(10):2620–2624, 1987.

[73] M. García-Calzada, G. Marbán, and A. B. Fuertes. Decomposition of CaS particles at ambient conditions. *Chem. Eng. Sci.*, 55(9):1661–1674, 2000.

[74] S. J. Wu, M. A. Uddin, S. Nagamine, and E. Sasaoka. Role of water vapor in oxidative decomposition of calcium sulfide. *Fuel*, 83(6):671–677, 2004.

[75] R. R. Patil, P. L. Muthal, S. M. Dhopte, V. K. Kondawar, and S. V. Moharil. Synthesis and properties of submicron range $CaSO_4$: Eu particles. *J. Lumin.*, 126(2):571–574, 2007.

[76] S. V. Upadeo, T. K. Gundurao, and S. V. Moharil. Mechanism of thermoluminescence in CaF_2:Eu and $CaSO_4$:Eu phosphors. *J. Phys.:Condens. Matter.*, 6(44):9459–9468, 1994.

[77] S. M. Dhopte, P. L. Muthal, V. K. Kondawar, and S. V. Moharil. On the role of europium in $CaSO_4$:Eu phosphor. *J. Lumin.*, 50(3):187–195, 1991.

[78] S. V. Godbole, J. S. Nagpal, and A. G. Page. Uv-induced photoluminescence and thermally stimulated luminescence of $CaSO_4$:Eu and CaF_2:Tb^{3+} phosphors. *Radiat. Meas.*, 32(4):343–348, 2000.

[79] J. W. Brightwell, B. Ray, and C. N. Buckley. Preparation, crystal-growth and luminescence in calcium sulfide. *J. Cryst. Growth.*, 59(1-2):210–216, 1982.

[80] N. Nishio, A. Kamimoto, and Y. Kawashima. *Coating for phosphor particles*. Patent. US 5856009, January 1999. `http://www.patentlens.net/patentlens/patent/US_5856009/`.

[81] C. W. Fan, T. Dang, J. Coveleskie, F. Schwab, D. Benjamin, and D. Sheppeck. *Moisture-resistant electroluminescent phosphor with high initial brightness and method of making* . Patent. WO 2007/087480 A2, 08 2007. `http://www.patentlens.net/patentlens/patent/WO_2007_087480_A2/`.

[82] S. H. Yoo and C. K. Kim. Changes in the moisture stability of CaS:Eu^{2+} phosphors with surface coating methods. *Macromol. Res.*, 17(11):907–911, 2009.

[83] J. Lin, Y. Huang, Y. Bando, C. C. Tang, and D. Golberg. Bn tubular layer-sheathed CaS:Eu^{2+} nanowires as stable red-light-emitting nanophosphors. *Chem. Commun.*, (43):6631–6633, 2009.

[84] H. T. Cui and G. Y. Hong. Coating of $Y_2O_3 : Eu^{3+}$ with polystyrene and its characterizations. *J. Mater. Sci. Lett.*, 21(1):81–83, 2002.

[85] G. S. Li, J. Boerio-Goates, B. F. Woodfield, and L. P. Li. Evidence of linear lattice expansion and covalency enhancement in rutile TiO_2 nanocrystals. *Appl. Phys. Lett.*, 85(11):2059–2061, 2004.

[86] H. Y. Lee and G. M. Kale. Hydrothermal synthesis and characterization of nano-TiO_2. *Int. J. Appl. Ceram. Technol.*, 5(6):657–665, 2008.

[87] G. L. Tian, H. B. He, and J. D. Shao. Effect of microstructure of TiO_2 thin films on optical band gap energy. *Chinese. Phys. Lett.*, 22(7):1787–1789, 2005.

[88] S. H. Oh, D. J. Kim, S. H. Hahn, and E. J. Kim. Comparison of optical and photocatalytic properties of TiO_2 thin films prepared by electron-beam evaporation and sol-gel dip-coating. *Mater. Lett.*, 57(26-27):4151–4155, 2003.

[89] H. Poelman, H. Tomaszewski, D. Poelman, D. Depla, and R. De Gryse. Effect of the oxygen deficiency of ceramic TiO_{2-x} targets on the deposition of TiO_2 thin films by dc magnetron sputtering. *Surf. Interface. Anal.*, 36(8):1167–1170, 2004.

[90] H. Q. Jiang, Q. Wei, Q. X. Cao, and X. Yao. Spectroscopic ellipsometry characterization of TiO_2 thin films prepared by the sol-gel method. *Ceram. Int.*, 34(4):1039–1042, 2008.

[91] R. C. Xie and J. K. Shang. Morphological control in solvothermal synthesis of titanium oxide. *J. Mater. Sci.*, 42(16):6583–6589, 2007.

[92] W. C. Du, H. T. Wang, W. Zhong, L. Shen, and Q. G. Du. High refractive index films prepared from titanium chloride and methyl methacrylate via a non-aqueous sol-gel route. *J. Sol-Gel Sci. Techn.*, 34(3):227–231, 2005.

[93] L. M. Nikolić, L. Radonjić, and V. V. Srdić. Effect of substrate type on nanostructured titania sol-gel coatings for sensors applications. *Ceram. Int.*, 31(2):261–266, 2005.

[94] L. L. Hu, T. Yoko, H. Kozuka, and S. Sakka. Effects of solvent on properties of sol gel-derived TiO_2 coating films. *Thin Solid Films*, 219(1-2):18–23, 1992.

[95] R. Fretwell and P. Douglas. An active, robust and transparent nanocrystalline anatase TiO_2 thin film - preparation, characterisation and the kinetics of photodegradation of model pollutants. *J. Photoch. Photobio. A: Chem.*, 143(2-3):229–240, 2001.

[96] Y. F. Zhu, L. Zhang, C. Gao, and L. L. Cao. The synthesis of nanosized TiO_2 powder using a sol-gel method with $TiCl_4$ as a precursor. *J. Mater. Sci.*, 35(16):4049–4054, 2000.

[97] G. S. Li, L. P. Li, J. Boerio-Goates, and B. F. Woodfield. High purity anatase TiO_2 nanocrystals: Near room-temperature synthesis, grain growth kinetics, and surface hydration chemistry. *J. Am. Chem. Soc.*, 127(24):8659–8666, 2005.

[98] M. Niederberger and G. Garnweitner. Organic reaction pathways in the nonaqueous synthesis of metal oxide nanoparticles. *Chem. Eur. J.*, 12(28):7282–7302, 2006.

[99] M. P. Moret, R. Zallen, D. P. Vijay, and S. B. Desu. Brookite-rich titania films made by pulsed laser deposition. *Thin Solid Films*, 366(1-2):8–10, 2000.

[100] S. Tanemura, L. Miao, W. Wunderlich, M. Tanemura, Y. Mori, S. Toh, and K. Kaneko. Fabrication and characterization of anatase/rutile-TiO_2 thin films by magnetron sputtering: a review. *Sci. Technol. Adv. Mat.*, 6(11):11–17, 2005.

[101] K. Eufinger. *PhD thesis*. Ghent University, Ghent, 2007.

[102] Thin film and bulk index of refraction and photonics calculations. Website, 2011. `http://www.luxpop.com/`.

[103] R. J. Gonzalez, R. Zallen, and H. Berger. Infrared reflectivity and lattice fundamentals in anatase TiO_2. *Phys. Rev. B*, 55(11):7014–7017, 1997.

[104] Z. C. Wang, U. Helmersson, and P. O. Kall. Optical properties of anatase TiO_2 thin films prepared by aqueous sol-gel process at low temperature. *Thin Solid Films*, 405(1-2):50–54, 2002.

[105] P. Eiamchai, P. Chindaudom, A. Pokaipisit, and P. Limsuwan. A spectroscopic ellipsometry study of TiO_2 thin films prepared by ion-assisted electron-beam evaporation. *Curr. Appl. Phys.*, 9(3):707–712, 2009.

[106] M. Horprathum, P. Chindaudom, and P. Limsuwan. A spectroscopic ellipsometry study of TiO_2 thin films prepared by dc reactive magnetron sputtering: Annealing temperature effect. *Chinese Phys. Lett.*, 24(6):1505–1508, 2007.

[107] D. Poelman and P. F. Smet. Methods for the determination of the optical constants of thin films from single transmission measurements: a critical review. *J. Phys. D: Appl. Phys.*, 36(15):1850–1857, 2003.

[108] I. Levin and D. Brandon. Metastable alumina polymorphs: Crystal structures and transition sequences. *J. Am. Ceram. Soc.*, 81(8):1995–2012, 1998.

[109] K. J. D. MacKenzie, J. Temuujin, M. E. Smith, P. Angerer, and Y. Kameshima. Effect of mechanochemical activation on the thermal reactions of boehmite (gamma-AlOOH) and gamma-Al_2O_3. *Thermochim. Acta*, 359(1):87–94, 2000.

[110] W. M. Zeng, L. Gao, L. H. Gui, and J. K. Guo. Sintering kinetics of alpha-Al_2O_3 powder. *Ceram. Int.*, 25(8):723–726, 1999.

[111] E. Langereis, M. Creatore, S. B. S. Heil, M. C. M. Van de Sanden, and W. M. M. Kessels. Plasma-assisted atomic layer deposition of Al_2O_3 moisture permeation barriers on polymers. *Appl. Phys. Lett.*, 89(8):081915, 2006.

[112] Y. R. Do, D. H. Park, and Y. S. Kim. Al_2O_3 nanoencapsulation of $BaMgAl_{10}O_{17}:Eu^{2+}$ phosphors for improved aging properties in plasma display panels. *J. Electrochem. Soc.*, 151(10):H210–H212, 2004.

[113] J. H. Eun, J. H. Lee, S. G. Kim, M. Y. Um, S. Y. Park, and H. J. Kim. The protection of MgO film against hydration by using Al_2O_3 capping layer deposited by magnetron sputtering method. *Thin Solid Films*, 435(1-2):199–204, 2003.

[114] K. Tadanaga, N. Katata, and T. Minami. Super-water-repellent Al_2O_3 coating films with high transparency. *J. Am. Ceram. Soc.*, 80(4):1040–1042, 1997.

[115] M. D. Groner, F. H. Fabreguette, J. W. Elam, and S. M. George. Low-temperature Al_2O_3 atomic layer deposition. *Chem. Mater.*, 16(4):639–645, 2004.

[116] P. Vitanov, T. Babeva, Z. Alexieva, A. Harizanova, and Z. Nenova. Optical properties of $(Al_2O_3)_x(TiO_2)_{1-x}$ films deposited by the sol-gel method. *Vacuum*, 76(2-3):219–222, 2004.

[117] R. L. Chiu and P. H. Chang. Thickness dependence of refractive index for anodic aluminium oxide films. *J. Mater. Sci. Lett.*, 16(2):174–178, 1997.

[118] N. Ozer, J. P. Cronin, Y. J. Yao, and A. P. Tomsia. Optical properties of sol-gel deposited Al_2O_3 films. *Sol. Energy Mater. Sol. Cells*, 59(4):355–366, 1999.

[119] E. D. Palik. *Handbook of Optical Constants of Solids*, volume 3. Academic Press, San Diego, 1998.

[120] B. Dong, C. R. Li, and M. K. Lei. Green and red up-conversion emissions of Er^{3+}-Yb^{3+}-codoped Al_2O_3 powders prepared by the nonaqueous sol-gel method. *J. Lumin.*, 126(2):441–446, 2007.

[121] B. Dong, C. R. Li, and X. J. Wang. Two color up-conversion emissions of Er^{3+}-doped Al_2O_3 nanopowders prepared by non-aqueous sol-gel method. *J. Sol-Gel Sci. Techn.*, 44(2):161–166, 2007.

[122] Z. H. Zhu, M. J. Sha, and M. K. Lei. Controllable formation of Er^{3+}-Yb^{3+} codoped Al_2O_3 films by the non-aqueous sol-gel method. *Thin Solid Films*, 516(15):5075–5078, 2008.

[123] S. Acosta, R. J. P. Corriu, D. Leclercq, P. Lefevre, P. H. Mutin, and A. Vioux. Preparation of alumina gels by a non-hydrolytic sol-gel processing method. *J. Non-Cryst. Solids*, 170(3):234–242, 1994.

[124] S. X. Zhou, M. Antonietti, and M. Niederberger. Low-temperature synthesis of gamma-alumina nanocrystals from aluminum acetylacetonate in nonaqueous media. *Small*, 3(5):763–767, 2007.

[125] J. M. R. Mercury, A. H. De Aza, and P. Pena. Synthesis of $CaAl_2O_4$ from powders: Particle size effect. *J. Eur. Ceram. Soc.*, 25(14):3269–3279, 2005.

[126] A. Gaki, T. Perraki, and G. Kakali. Wet chemical synthesis of monocalcium aluminate. *J. Eur. Ceram. Soc.*, 2(2-3):1785–1789, 2007.

[127] B. M. Mohamed and J. H. Sharp. Kinetics and mechanism of formation of monocalcium aluminate, $CaAl_2O_4$. *J. Mater. Chem.*, 7(8):1595–1599, 1997.

[128] J. J. Vijaya, L. J. Kennedy, G. Sekaran, and K. S. Nagaraja. Utilization of Sr(ii)-added calcium aluminate for the detection of volatile organic compounds. *Ind. Eng. Chem. Res.*, 46(19):6251–6258, 2007.

[129] J. Hölsä, T. Laamanen, M. Lastusaari, M. Malkamäki, E. Welter, and D. A. Zajac. Valence and environment of rare earth ions in $CaAl_2O_4$:Eu^{2+},R^{3+} persistent luminescence materials. *Spectrochim. Acta B*, 65(4):301–305, 2010.

[130] T. Aitasalo, J. Hölsä, H. Jungner, M. Lastusaari, and J. Niittykoski. Sol-gel processed Eu^{2+}-doped alkaline earth aluminates. *J. Alloy Compd.*, 341(1-2):76–78, 2002.

[131] Y. J. Park and Y. J. Kim. Effects of crystal structures on luminescent properties of Eu doped Ca-Al-O systems. *Ceram. Int.*, 34(4):1109–1112, 2008.

[132] G. H. Chen. Mechanical activation of calcium aluminate formation from $CaCO_3$-Al_2O_3 mixtures. *J. Alloy Compd.*, 416(1-2):279–283, 2006.

[133] A. Douy and M. Gervais. Crystallization of amorphous precursors in the calcia-alumina system: A differential scanning calorimetry study. *J. Am. Ceram. Soc.*, 83(1):70–76, 2000.

[134] D. Haranath, P. Sharma, and H. Chander. Optimization of boric acid content in developing efficient blue emitting long persistent phosphor. *J. Phys. D: Appl. Phys.*, 38(3):371375, 2005.

[135] T. Aitasalo, J. Hölsä, H. Jungner, M. Lastusaari, and J. Niittykoski. Comparison of sol-gel and solid-state prepared Eu^{2+} doped calcium aluminates. *Materials Science*, 20(1), 2002.

[136] T. Aitasalo, J. Hölsä, H. Jungner, M. Lastusaari, J. Niittykoski, M. Parkkinen, and R. Valtonen. Eu^{2+} doped calcium aluminates prepared by alternative low temperature routes. *Opt. Mater.*, 26(2):113–116, 2004.

[137] S. Janáková, L. Salavcová, G. Renaudin, Y. Filinchuk, D. Boyer, and P. Boutinaud. Preparation and structural investigations of sol-gel derived Eu^{3+}-doped $CaAl_2O_4$. *J. Phys. Chem. Solids*, 68(5-6):1147–1151, 2007.

[138] W. Hörkner and H. K. Müller-Buschbaum. Crystal-structure of $CaAl_2O_4$. *J. Inorg. Nucl. Chem.*, 38(5):983–984, 1976.

[139] T. Nakamura, T. Matsuzawa, C. C. Rowlands, V. Beltrán-López, G. M. Smith, and P. C. Riedi. Epr investigations on europium(II)-doped barium aluminate. *J. Chem. Soc., Faraday Trans.*, 94:3009–3012, 1998.

[140] D. Ravichandran, S. T. Johnson, S. Erdei, R. Roy, and W. B. White. Crystal chemistry and luminescence of the Eu^{2+}-activated alkaline earth aluminate phosphors. *Displays*, 19(4):197–203, 1999.

[141] V. Singh, V. Natarajan, and D. K. Kim. Characterisation and luminescence investigations of Mn doped $CaAl_2O_4$ phosphor prepared by combustion. *Int. J. Mod. Phys. B*, 22(13):2093–2099, 2008.

[142] X. J. Wang, D. D. Jia, and W. M. Yen. Mn^{2+} activated green, yellow, and red long persistent phosphors. *J. Lumin.*, 102:34–37, 2003.

[143] S. W. Choi and S. H. Hong. Size and morphology control by planetary ball milling in $CaAl_2O_4$:Eu^{2+} phosphors prepared by Pechini method and their luminescence properties. *Mater. Sci. Eng. B*, 171(1-3):69–72, 2010.

[144] V. Singh, J. J. Zhu, M. K. Bhide, and V. Natarajan. Synthesis, characterisation and luminescence investigations of Eu activated $CaAl_2O_4$ phosphor. *Opt. Mater.*, 30(3):446–450, 2007.

[145] C. K. Chang, J. Xu, L. Jiang, D. L. Mao, and W. J. Ying. Luminescence of long-lasting $CaAl_2O_4$:Eu^{2+},Nd^{3+} phosphor by co-precipitation method. *Mater. Chem. Phys.*, 98(2-3):509–513, 2006.

[146] W. Y. Jia, H. B. Yuan, L. Z. Lu, H. M. Liu, and W. M. Yen. Crystal growth and characterization of Eu^{2+},Dy^{3+}:$SrAl_2O_4$ and Eu^{2+},Nd^{3+}:$CaAl_2O_4$ by the LHPG method. *J. Cryst. Growth.*, 200(1-2):179–184, 1999.

[147] T. Katsumata, T. Nabae, K. Sasajima, and T. Matsuzawa. Growth and characteristics of long persistent $SrAl_2O_4$- and $CaAl_2O_4$-based phosphor crystals by a floating zone technique. *J. Cryst. Growth.*, 183(3):361–365, 1998.

[148] M. Murayama, N. Takeuchi, Y. Aoki, and T. Matsuzawa. *Phosphorescent phosphor*. Patent. US 5424006, June 1995. `http://www.patentlens.net/patentlens/patent/US_5424006/`.

[149] P. F. Smet, K. Korthout, J. E. Van Haecke, and D. Poelman. Using rare earth doped thiosilicate phosphors in while light emitting LEDs: Towards low colour temperature and high colour rendering. *Mater. Sci. Eng. B*, 146(1-3):264–268, 2008.

[150] Y. Tamura and A. Shibukawa. Optical studies of CaS:Eu,Sm infrared stimulable phosphors. *Jpn. J. Appl. Phys.*, 32(7):3187–3196, 1993.

[151] W. Lehmann and F. M. Ryan. Cathodoluminescence of CaS:Ce^{3+} and CaS:Eu^{2+} phosphors. *J. Electrochem. Soc.*, 118(3):477–482, 1971.

[152] M. W. Brooks and S Lynn. Recovery of calcium carbonate and hydrogen sulfide from waste calcium sulfide. *Ind. Eng. Chem. Res.*, 36(10):4236–4242, 1997.

[153] R-900 titanium dioxide. Website, 2011. `http://www2.dupont.com/Titanium_Technologies/en_US/products/900`.

[154] D. Mardare, M. Tasca, M. Delibas, and G. I. Rusu. On the structural properties and optical transmittance of TiO_2 r.f. sputtered thin films. *Appl. Surf. Sci.*, 156(1-4):200–206, 2000.

[155] P. S. Shinde, P. S. Patil, P. N. Bhosale, and C. H. Bhosalew. Structural, optical, and photoelectrochemical properties of sprayed TiO_2 thin films: Effect of precursor concentration. *J. Am. Ceram. Soc.*, 91(4):1266–1272, 2008.

[156] M. J. Van Bommel and T. N. M. Bernards. Spin coating of titanium ethoxide solutions. *J. Sol-Gel Sci. Techn.*, 8(1-3):459–463, 1997.

[157] G. Risse, S. Matys, and H. Böettcher. Investigation into the photo-induced change in wettability of hydrophobized TiO_2 films. *Appl. Surf. Sci.*, 254(18):5994–6001, 2008.

[158] L. Van Puyvelde. *Master thesis*. Ghent University, Ghent, 2010.

[159] T. Tsumura, N. Kojitani, H. Umemura, M. Toyoda, and M. Inagaki. Composites between photoactive anatase-type TiO_2 and adsorptive carbon. *Appl. Surf. Sci.*, 196(1-4):429–436, 2002.

[160] F. A. Jenkins and H. E. White. *Fundamentals of Optics Fourth Edition*. McGraw-Hill, Auckland, 1976.

[161] W. Decker and B. Henry. Basic principles of thin film barrier coatings. In *45th Annual Technical Conference Proceedings*, Lake Buena Vista, Florida, USA, 2002.

[162] D. Jiang, D. M. Hulbert, U. Anselmi-Tamburini, T. Ng, D. Land, and A. K. Mukherjee. Optically transparent polycrystalline Al_2O_3 produced by spark plasma sintering. *J. Am. Ceram. Soc.*, 91(1):151–154, 2008.

[163] G. Hirata, N. Perea, M. Tejeda, J. A. Gonzalez-Ortega, and J. McKittrick. Luminescence study in Eu-doped aluminum oxide phosphors. *Opt. Mater.*, 27(7):1311–1315, 2005.

[164] K. Vanbesien, P. De Visschere, P. F. Smet, and D. Poelman. Electrical properties of Al_2O_3 films for TFEL-devices made with sol-gel technology. *Thin Solid Films*, 514(1-2):323–328, 2006.

[165] J. W. Lee, C. W. Won, B. S. Chun, and H. Y. Sohn. Dip coating of alumina films by the sol-gel method. *J. Mater. Res.*, 8(12):3151–3157, 1993.

[166] D. W. Thompson, P. G. Snyder, L. Castro, L. Yan, P. Kaipa, and J. A. Woollam. Optical characterization of porous alumina from vacuum ultraviolet to midinfrared. *J. Appl. Phys.*, 97(11):0021–8979, 2005.

[167] M. E. Mata-Zamora and J. M. Saniger. Thermal evolution of porous anodic aluminas: a comparative study. *Rev. Mex. Fis.*, 51(5):502–509, 2005.

[168] J. T. Kloprogge, L. V. Duong, B. J. Wood, and R. L. Frost. Xps study of the major minerals in bauxite: Gibbsite, bayerite and (pseudo-)boehmite. *J. Colloid. Interf. Sci.*, 296(2):572–576, 2006.

[169] J. Q. Wang, S. R. Yang, M. Chen, and Q. J. Xue. Preparation and characterization of arachidic acid self-assembled monolayers on glass substrate coated with sol-gel Al_2O_3 thin film. *Surf. Coat. Technol.*, 176(2):229–235, 2004.

[170] C. Morterra and G. Magnacca. A case study: Surface chemistry and surface structure of catalytic aluminas, as studied by vibrational spectroscopy of adsorbed species. *Catal. Today*, 27(3-4):497–532, 1996.

[171] M. Nguefack, A. F. Popa, S. Rossignol, and C. Kappenstein. Preparation of alumina through a sol-gel process. Synthesis, characterization, thermal evolution and model of intermediate boehmite. *Phys. Chem. Chem. Phys.*, 5(19):497–532, 2003.

[172] G. Liu, M. J. Jia, Z. Zhou, L. Wang, W. X. Zhang, and D. Z. Jiang. Synthesis and pore formation study of amorphous mesoporous aluminophosphates in the presence of citric acid. *J. Colloid Interface Sci.*, 302(1):278–286, 2006.

[173] S. Fessi and A. Ghorbel. Preparation of alumina supported palladium catalysts by sol-gel method. *J. Sol-Gel Sci. Technol.*, 19(1-3):417–420, 2000.

[174] K. Tadanaga, T. Iwami, N. Tohge, and T. Minami. Precursor structure and hydrolysis-gelation process of $Al(O\text{-}sec\text{-}Bu)_3$ modified with ethylacetoacetate. *J. Sol-Gel Sci. Technol.*, 3:5–10, 1994.

[175] R. Rinaldi and U. Schuchardt. On the paradox of transition metal-free alumina-catalyzed epoxidation with aqueous hydrogen peroxide. *J. Catal.*, 236(2):335–345, 2005.

[176] G. K. Priya, P. Padmaja, K. G. K. Warrier, A. D. Damodaran, and G. Aruldhas. Dehydroxylation and high temperature phase formation in sol-gel boehmite characterized by Fourier transform infrared spectroscopy. *J. Mater. Sci. Lett.*, 16(19):1584–1587, 1997.

[177] C. H. Shek, J. K. L. Lai, T. S. Gu, and G. M. Lin. Transformation evolution and infrared absorption spectra of amorphous and crystalline nano-Al_2O_3 powders. *Nanostruct. Mater.*, 8(5):605–610, 1997.

[178] Silicon. Website, 2011. `http://www.reading.ac.uk/infrared/library/infraredmaterials/ir-infraredmaterials-si.aspx`.

[179] P. Wagner and J. Hage. Thermal double donors in silicon. *Appl. Phys. A: Mater. Sci. Process*, 49(2):123–138, 1989.

[180] T. Lichtenstein. *Handbook of Thin Film Materials*. Academic Press, New York, 1972.

[181] Physical Vapour Deposition (PVD) - an introduction. Website, 2011. `http://www.azom.com/article.aspx?ArticleID=1558`.

[182] J. Singh and D. E. Wolfe. Nano and macro-structured component fabrication by electron beam-physical vapor deposition EB-PVD. *J. Mater. Sci.*, 40(1):1–26, 2005.

[183] S. Iftekhar, J. Grins, G. Svensson, J. Lööf, T. Jarmar, G. A. Botton, C. M. Andrei, and H. Engqvist. Phase formation of $CaAl_2O_4$ from

$CaCo_3$-Al_2O_3 powder mixtures. *J. Eur. Ceram. Soc.*, 28(4):747–756, 2008.

[184] K. A. Gschneidner, J. C. G. Bünzli, and V.K. Pecharsky. *Handbook on the physics and chemistry of rare earths: optical spectroscopy*. Elsevier, Amsterdam, 2007.

[185] Glotech international. Website, 2011. `http://www.glotechint.com/`.